Tools for Measuring the Material Parameters of Neurites

Madeleine Anthonisen

Department of Physics
McGill University
Montreal, Canada

April 2020

A thesis submitted to McGill University in partial fulfillment of the requirements of the degree of Doctor of Philosophy.

2020/04/08

Acknowledgments

> I felt a cleaving in my mind
> As if my brain had split;
> I tried to match it, seam by seam,
> But could not make them fit.
>
> Emily Dickinson

I would like to thank the many people who made this journey possible. First and foremost I am incredibly grateful to my supervisor, Peter Grütter. His guidance, experience, insights and research philosophies were essential to every part of this process. Peter, thanks for everything, the support and the freedom to pursue the projects in the directions of interest to me. You made this entire project possible.

Thanks to the people who made the experimental and technical aspects of this project possible. Thanks to Prof. Yoichi Miyahara for his wisdom and his patience. Thanks to John Smeros, Robert Gagnon and Richard Talbot: you are wizards and the physics department, let alone my project, could not run without you.

I am grateful to Monserratt Lopez, Margaret Magdesian and Evan McDonough for being incredible mentors and acquainting me with the world of biophysics. I can always count on you for invaluable advice.

I am grateful to my lab-mates Ying, Tyler, Matt, José, Megan, Rikke, Aaron, Andreas for help and emotional support.

I want to thank everyone in the front office, especially Diane and Louise for all their help through my 10 long years in the physics department.

Finally I want to thank my parents, Nathaniel, Grailing, Justin, Alisa, Lea, Brian, Charlotte, Erin, Presely, Rosie for taking such good care of me all these years.

Abstract

This thesis details the development of a collection of methods to measure the material parameters of mechanically-created neurites. Neurites are long thin processes extending from the body of a nerve cell. To characterize the material response of a neurite to a deformation, information about both its tension and its geometry are required and the body of this thesis is divided accordingly. In the first part, we describe a platform to precisely control and manoeuver neurite-tethered polystyrene beads. We use a mechanical probe composed of a hollow micropipette with its tip fixed to a functionalized bead to incite the formation of a neurite in a sample of rat hippocampal neurons. In the second part, we measure neurite tension by optically tracking the deflection of the beaded tip as the neurite is extended. By calibrating the spring constant of the pipette we can convert this deflection to a force. We use this technique to investigate the dependence of the force-extension relationship on mechanical pull speeds. We develop statistically robust methods to categorize the results and describe the behaviour of neurites under tension. The third part of this work presents a method to measure dimensions of objects below the optical diffraction limit using diffraction analysis of out-of-focus images. We validate this method by applying it to calibration objects with correlative scanning electron microscope (SEM) measurements. We apply this procedure to obtain the diameters of neurites and investigate the dependence of geometry on mechanical pull speed. In the final part of the thesis, we develop a model of neurite growth in response to elastic deformation. We decompose applied stretch into an elastic component and a growth component and adopt an observationally-motivated growth law. We compute best-fit model parameters by fitting force-extension curves. We find a time constant for the growth law of 0.009 s^{-1}, similar to the diffusion rate of actin in a cell. These results characterize the kinematics of neurite growth and establish new limits on the growth rate of neurites.

Abrégé

Cette thèse détaille le développement d'une collection de méthodes pour mesurer les paramètres matériels des neurites créés mécaniquement. Les neurites sont de longs processus minces s'étendent du corps d'une cellule nerveuse. Pour caractériser la réponse matérielle d'un neurite à une déformation, des informations sur sa tension et sa géométrie sont nécessaires et le corps de cette thèse est divisée en conséquence. Dans la première partie, nous décrivons une configuration pour contrôler et manœuvrer avec précision des sphères de polystyrène attachées aux neurites. Nous utilisons une micropipette avec son extrémité fixée à une sphère fonctionnalisée pour inciter la formation d'une neurite dans un échantillon de neurones hippocampiques de rat. Dans la deuxième partie, nous mesurons la tension des neurites en suivant optiquement la déviation de la sphr̀e au point au fur et à mesure de l'extension de la neurite. En calibrant la constante de rigidité de la pipette, nous pouvons convertir cette déviation en une force. Nous utilisons cette technique pour étudier la dépendance de la relation force-extension sur les vitesses d'extensions mécaniques. Nous développons des méthodes statistiques pour catégoriser les résultats et décrire le comportement des neurites sous tension. La troisième partie de ce travail présente une méthode pour mesurer les dimensions d'objets en dessous de la limite de diffraction optique en utilisant l'analyse de diffraction d'images floues. Nous validons cette méthode en l'appliquant à des objets de tailles connues avec des mesures de microscopie électronique à balayage (MEB) corrélatifs. Nous appliquons cette procédure pour obtenir les diamètres des neurites et étudions la dépendance de la géométrie à la vitesse d'extension mécanique. Dans la dernière partie de la thèse, nous développons un modèle de croissance des neurites en réponse à la déformation élastique. Nous décomposons l'étirement appliqué en un composant élastique et un composant de croissance et adoptons une loi de croissance motivée par l'observation. Nous calculons les paramètres du modèle le mieux ajusté en ajustant les courbes force-extension. Nous trouvons une constante de temps pour la loi de croissance de 0,009 s^{-1}, similaire au taux de diffusion de l'actine dans une cellule. Ces résultats caractérisent

la cinématique de la croissance des neurites et établissent de nouvelles limites sur le taux de croissance des neurites.

Contents

Preface

Preface

This thesis consists of an introduction and 4 papers that either have been or will be published. Chapters 6-8 are original contributions to the field of biophysics. In this preface I will identify my contribution to each work.

Statement of Originality and Contributions

Chapter 5: M. H. Magdesian, M. Anthonisen, G. M. Lopez-Ayon, X. Y. Chua, M. Rigby, P. Grütter, *Rewiring Neuronal Circuits: A New Method for Fast Neurite Extension and Functional Neuronal Connection*, JoVE (Journal of Visualized Experiments) 124 (2017): e55697.

This publication is an experimental methods paper and is a more detailed description of procedures introduced in Magdesian *et al.* (2016). Margaret Magdesian and G. Monserratt Lopez-Ayon initiated this project and originally developed the method. MM is first author on this article, I am second author. Together with MM, I wrote the manuscript and added details to make the method accessible and replicable to the scientific community. I performed all the demonstration-experiments in the article, some in tandem with the other authors.

Chapter 6: M. Anthonisen, M. Rigby, M. H. Sangji, X. Y. Chua and P. Grütter, *Response of Mechanically-Created Neurites to Extension*, Journal of the Mechanical Behavior of Biomedical Materials. **98**, 121 (2019).

I am first author on this peer-reviewed article. This is the first large scale study of the force-extension curves of neurites. It introduces a method to acquire force-extension curves and a new categorization scheme to analyze data. P. Grütter and M. H. Sangji initiated the project in MHS's Master's thesis. MHS wrote code to track particles. Matthew Rigby acquired fluorescent images of neurites.

Chapter 7: M. Anthonisen, Y. Zhang, M. H. Sangji and P. Grütter, *Quantifying Neurite Morphology Below the Diffraction Limit of an Optical Microscope Using Out-of-Focus Images*, Applied Optics 20;59(9):2914-2923 (2020).

This publication describes an original method to measure the diameters of isolated objects below the optical diffraction limit. I developed the method and performed analysis and measurements, with supervision and input from P. Grütter. Correlative SEM measurements were performed by Y. Zhang and X. Capaldi.

Chapter 8: M. Anthonisen and P. Grütter, *Growth and Elasticity of Mechanically-Created Neurites*, Preprint, 2019. arXiv:1912.05735 [physics.bio-ph].

I initiated this project to explore the roles of stress and growth in neurite deformations with a growth law identified in a previous paper by P. Grütter. I performed the analytical calculations in tandem with P. Grütter and wrote the text of the manuscript.

Part I

Introduction

Chapter 1

Neuromechanics

1.1 Background and Motivation

Over the past 50 years, neuromechanics has become increasingly relevant as a framework to understand various aspects of brain development and function [1,2]. Mechanical forces and deformations are inherent to many physiological processes such as cellular growth, guidance and motility [3]. They also play an integral role in pathological processes such as brain injury, certain neurodegenerative diseases and brain surgery [4]. Quantifying the material response of the brain to mechanical stimuli, as well as the mechanical forces exerted by the brain itself, could thus have important implications for healthcare and medicine [2,5]. In particular, detection of mechanical forces at the single-cell level could elucidate questions of cell growth and regeneration [3,6–8,10–12]. This, in turn, could have a significant impact on surgical therapies since neuronal regrowth in the central nervous system (CNS) over large distances is severely limited. Consequently, injuries to the brain or spinal cord that sever cellular connectors can cause permanent impairment or even death.

Elongation of neurites, long processes extending from the body of the neuron that are responsible for signal propagation, has been widely studied (see e.g. Refs. [8,9] for reviews). Most techniques to measure neurite extension and growth apply a mechanical stress and measure the resulting deformation [9]. These experiments have lead to the identification of tension as a driver of neurite growth and development; “a pulled axon grows as though the nerve cell contained telescopic machinery prefabricated for elongation” [3]. Recent work, [13–15], has shown that this “telescopic” growth also occurs in axon-like structures initiated from parent axons or dendrites. However, the mechanisms responsible for this surprising mass-accretion and the role of tension in limiting this process remain outstanding mysteries [3, 6–8].

To understand how tension influences the mechanisms underlying single neurite growth and elongation, high throughput biological force measurement tools are needed. However, large-scale experimental repetition is limited in most conventional methods probing force scales relevant to neurons. For example, so-called “towed growth” experiments that apply force to a neurite by attaching either a microneedle or the cantilever of an Atomic Force Microscope (AFM) to its end have relatively low experimental yields because of the time required for an adhesive contact to form.

This thesis details the development of a collection of methods to obtain the material parameters of mechanically-created neurites. To characterize the material response of a neurite, information about both its tension and its geometry are required.

In Part II, the experimental set-up and sample preparation procedures are described. This chapter also introduces neurite initiation and elongation via a bead, microneedle and suction in samples of rat hippocampal neurons. Ref. [18] showed that when a polystyrene bead coated with the positively charged polymer poly-D-lysine (PDL) contacts an axon or dendrite, a synapse is formed at the bead-cell interface. If the bead is pulled relative to the sample, e.g. with a microneedle attached with suction, the formation of an auxiliary structure, the neurite, is induced.

In the following Parts, I describe two methods to obtain two ingredients for a stress measurement: axial force (Part III) and geometry (Part IV). Part III builds on the results in Part II, detailing the development of a force-probe by adding an optical tracking method to track the bending of the microneedle and obtain the force exerted on it by the extending neurite. A large-scale investigation of the force-extension relationships of neurites induced over a range of pull speeds is presented as is a categorization scheme to determine similarities between curves.

Part IV is motivated by the necessity for a suitable technique to obtain the diameters of neurites below the optical diffraction limit. It details a method to compare diffraction patterns of a neurite and a calibration object to those in a series of out-of-focus images of objects of known dimension. This is used to obtain the cross-sectional areas of induced neurites and parameterize them by pull speed.

Finally, in Part V the results of Parts III&IV are combined to quantify the relationship between mass addition and tension. A Mooney-Rivlin model is compared to other candidates and determined to be the best model to fit the data. The material parameters are given.

1.2 Mechanical Components of a Neuron

The brain is a complex system with different levels of organization across many scales, Fig. 1.1. The average human brain contains roughly ∼100 billion neurons that exist in an extra-cellular matrix and are in contact with glial cells [5]. This thesis focuses on individual neurons in isolation on a glass coverslip; the idea is that in a simplistic setting we can identify network behaviours or limits specific to neurons. We note, however, the necessity of studying neurons in 3D environments analogous to their *in vivo* state in order to gain a complete understanding of their functions and properties. The results described here are a preliminary step to this understanding.

In this section, we briefly review the constituents of a neuron relevant to discussions of its material parameters. Neurons are cells specialized for information processing. They have many of the same features as other cells including a cell body (soma), a nucleus containing DNA and a plasma membrane. Unlike other cells, neurons have long, thin extensions called neurites that connect the soma to other cells and enable the exchange of information via the propagation of chemical and/or electrical signals. Neurites are classified as either axons, which send signals or dendrites, which are shorter and receive signals. The junction between a signal

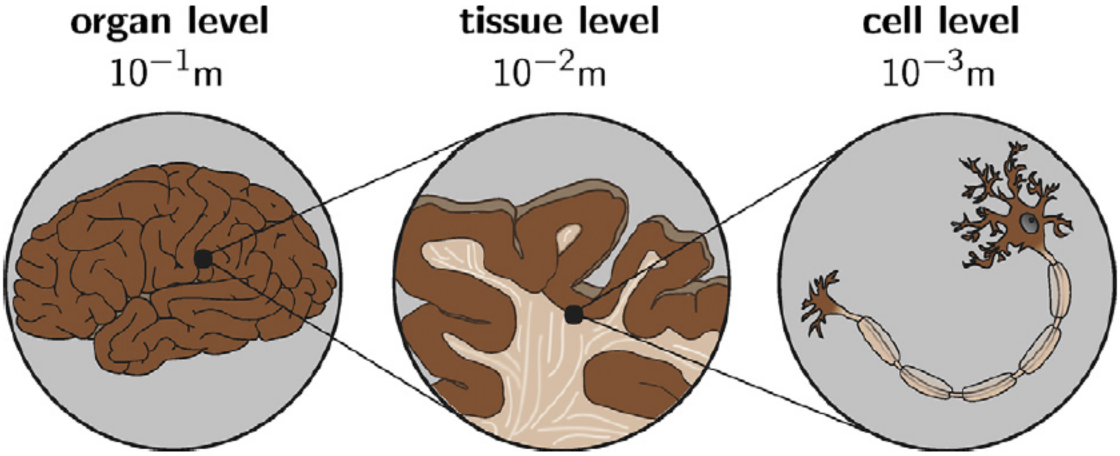

Figure 1.1 Levels of organization of the human brain at different scales. This figure was published in Advances in Applied Mechanics, Volume 48, Alain Goriely, Silvia Budday, Ellen Kuhl, Neuromechanics: From Neurons to Brain, pp81, Copyright Elsevier (2015).

transmitting neuron and a signal receiving neuron is called a synapse. Some neurites are encased in a dielectric layer, the myelin sheath, but not the hippocampal neurons studied in this thesis.

The cell body and neurites are permeated by a network of polymers, the cytoskeleton, that maintains cell structure and motility and is involved in cellular transport. The exact mechanisms by which the cytoskeleton mediates force generation and mechanotransduction present many open questions but the interplay between the various cytoskeleton elements and the assembly/disassembly of its structures are connected to processes of axonal elongation and motility. A perspective commonly adopted in the literature is to view axonal guidance cues (intrinsic and extrinsic) as elements that alter the physical state of the cytoskeleton through biochemical pathways. In a simplified model, the cytoskeleton is described as a meshwork of three polymers (see Fig. 1.2):

- F-actin, a polar structure polymerized at one end by G-actin subunits and cross-linked by the molecular motor myosin II.

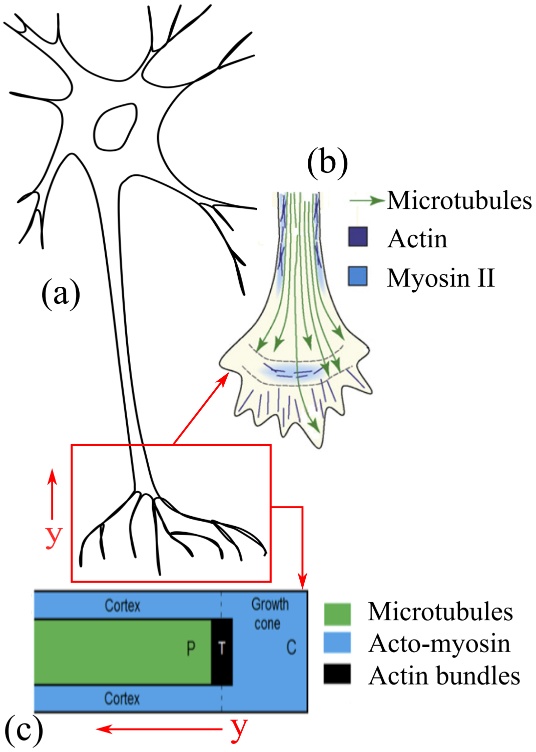

Figure 1.2 **(a)** Schematic of an axon. Growth cone and initial part of axon shaft labeled in red box. **(b)** Region inside the red box shown with schematic representation of cytoskeleton. **(c)** Simplified schematic of **(b)** with the growth cone and axon shaft modelled as a microtubule mesh core surrounded by an actin-rich cortex. This figure was adapted from figures published in Physical Review E, Volume 93, Pierre Recho, Antoine Jerusalem, Alain Goriely, Growth collapse and stalling in a mechanical model for neurite motility, p.032410, Copyright American Physical Society (2016).

- Microtubules: polar and polymerized by tubulin subunits; cross-linked by molecular motors dyenin or kinesin.
- Neurofilaments: passive and apolar. These are not shown in Fig. 1.2; the contribution of neurofilaments to the network elasticity are usually not modelled as separate from the contribution of microtubules [12].

The axoplasm, which is the segment of the axon that connects the soma to the proximal end (the growth cone) can be thought of as a microtubule core, linked by proteins in a quasilattice structure, surrounded by a cortical mesh consisting of F-actin (Fig. 1.2). The action of myosin motors in the cortex generates contractile stress.

There are many physical models linking the cytoskeleton to neurite motility in the literature. Ref. [12] broadly categorizes these according to wether the growth cone is propelled forward by actin polymerization pushing its leading edge combined with myosin-generated contraction at the trailing edge or wether microtubules from the axoplasm push the growth cone forward by polymerizing against trailing edge or wether motion arises from some combination of these phenomena. A framework to describe the mechanical behaviour of neurites has emerged from numerous experiments that probe its dynamics and/or investigate the role of individual elements of the cytoskeleton network by applying drug treatments that either enhance or inhibit the actions of these elements. The behavioural trends of neurites observed in the body of these experiments (as summarized in Ref. [12]) are

- Neurite growth in response to axial force. Neurites extend with tension applied to the proximal end with a cantilever or microneedle. The response of neurites is elastic only at very small strains, $< 0.1\%$. For larger deformations, a non-linear model is necessary to describe the dynamics.
- Neurite retraction under microtubule depletion/elongation under increased microtubule polymerization.

- Neurite retraction with reduced adhesivity of substrate. This is connected to the dependence of myosin II inhibition on substrate adhesivity.
- Neurite motility is linked to contractility, demonstrated by drugs that affect the contractility of myosin II.

Physical models that incorporate aspects of force, motility and environment of the cell should be consistent with this framework.

The field of mechanobiology applies nano- and microtechnological approaches to quantify the mechanical properties of biological systems [19, 20]. Mechanobiology seeks to understand the links between forces and functionality; it explores the way in which cells process the information contained in mechanical changes. Reproducibility and throughput are issues in the field of mechanobiology [19] and are addressed in this thesis.

Chapter 2

Biological Force Measurement Techniques

2.1 Introduction

This section is an overview of common techniques to measure forces on or within cells. It discusses the resolutions, advantages, disadvantages and important conclusions of each experimental method. Ref. [6] presents a nice review of these techniques.

2.2 Force-Calibrated Microneedles

For decades, force-calibrated microneedles have been widely-used to apply and measure forces in neurons [1]. The deformation of a flexible glass microneedle is recorded optically and combined with its experimentally-determined stiffness to measure a force. Often, deformation of the needle is measured relative to a second, stiffer 'reference' needle mounted near the first needle [10, 21–24].

Ref. [1] first applied microneedles to neurites (PC12) and discovered that tension induces neurite growth but did not quantify forces. Force-calibrated microneedles were first introduced in Ref. [25] where PC12 axons were rapidly pulled laterally, perpendicular to the long axis of the neurite, see Fig. 2.1. They observed a linear relationship between deformed length of the neurite (labeled by l in Fig. 2.1) and force. The mean axonal stiffness of 82 neurites was $2.44 \pm 2.20 \times 10^{-4}$ N/m. We note that the elastic response was for strains $\sim< 0.2\%$ on timescales of 2-3 seconds. For larger deformations under the same experimental paradigm, Ref. [26] showed PC12 neurites had a nonlinear force-response to applied strain. They obtained diameters from optical images and fit a viscoelastic model to their data to find an elastic modulus of 12.2 kPa.

Over the years there have been numerous experiments in which tension is applied to a neurite along its axial direction [10, 21–24, 39]. These reports all observe that an axial force applied to the tip of a neurite will elongate it and this elongation is elastic below a certain threshold. Ref. [21] fixed a microneedle to the cell body, raised it off the substrate leaving only the growth cone attached and allowed the growth cone to generate tension by crawling along the substrate. Ref. [39] applied tension to rat hippocampal neurites, the same cell-type studied in this thesis, at different stages of development. They observed a linear relation between pull speed and tension—something we did not see although our experiments were conducted on different timescales. We will show this in Ch. 6. Ref. [24] conducted microneedle measurements while observing labeled docked mitochondria as a proxy for sub-cellular strain. They developed a mathematical model by comparing subcellular forces to total neurite tension. Note that these methods fix microneedles to cells by coating needles with a cell adhesive then applying some manipulation to create a contact with the cell then waiting for adhesion.

Microneedle techniques are effective at measuring forces as low as $10^{-3} - 10^{-2}$ nN. They do not require involved analysis or specialized equipment so could be paired with other approaches to study cell life, e.g. optical or electrical techniques. Microneedle techniques also present the option for the neurite to be pulled along the substrate or elevated off of it—depending on if cell-substrate friction is of interest for a particular model. On the other hand, some disadvantages are that they are traditionally time consuming and are highly sensitive to vibrations. The method we present is an adaptation of these classic techniques and here we highlight a major advantage: we use microbeads adhered to the cell and suction to attach neurites to the microneedle, thus bypassing the time it takes for a cell-microneedle contact to form. This greatly enhances experimental yield.

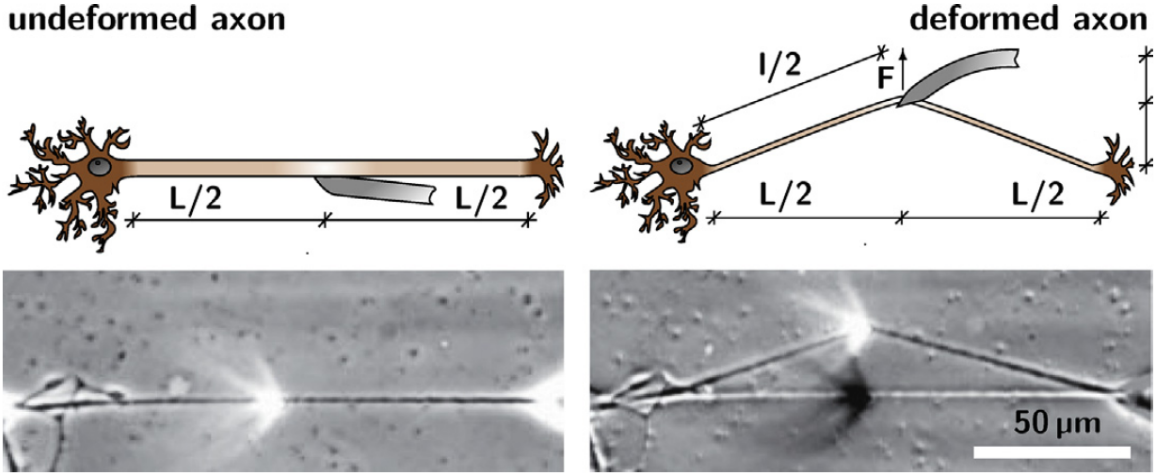

Figure 2.1 A lateral pulling experiment to measure the stiffness of an individual axon. From the first image to the second, the axon of length L has been rapidly deformed by the microneedle (bright spot) with a force F to a length l. This figure was published in Advances in Applied Mechanics, Volume 48, Alain Goriely, Silvia Budday, Ellen Kuhl, Neuromechanics: From Neurons to Brain, pp85, Copyright Elsevier (2015).

2.3 Traction Force Microscopy

Traction Force Microscopy (TFM) refers to techniques that mechanically manipulate the substrate to which the cells are adhered. This allows the application of uniaxial, biaxial or radial strains and is meant to mimic *in vivo* conditions. As with microneedles, the force applied to or by cells is calculated by combining the substrate stiffness with its deformation. Many studies have used deformable substrates to elongate axons [27–29]. Refs. [27, 29] investigated the connection between substrate stiffness, outgrowth and traction force of the growth cones and found traction force incresed with substrate stiffness. Ref. [30] found that neurite branching was linked to softer substrates.

Ref. [32] applies rapid stretching to neurons via a deformable substrate and reports a disruption of the microtubule network and partial loss of mechanical functions. On the surface, these findings are inconsistent with the results of Refs. [11, 31] that demonstrate that stretch-grown axons maintain structural and electrical viability. However, differences in experimental conditions in the reports could explain these outcomes. Refs. [11, 31] apply stretch to axons which are suspended in media and at much slower rates than Ref. [32]. More studies are needed to conclusively identify the roles of environmental conditions and the platform we present in Chapter. 5 is an ideal playground to test models and constrain such experimental parameters.

The detailed operating principles of TFM are beyond the scope of this thesis (instead see e.g. Ref. [33] for a review) but discussion of TFM naturally leads to open questions concerning the role of substrate adhesiveness and compliance in neurite elongation/contraction. We have summarize some results that demonstrate the link between substrate compliance and elongation but more experiments are needed to elucidate the mechanisms involved.

While TFM can resolve forces over several orders of magnitude, $\sim 10^{-2}$–10^{1} nN [6], it has the disadvantage of uniform substrate stiffness that fails to simulate the *in vivo* environment. The creation of a stiffness gradient, e.g. by micropatterning, is a technical challenge.

2.4 Optical Tweezers

Optical tweezers use a highly-focused infrared laser to manipulate micro- or nano-sized dielectric objects, usually transparent beads. When laser photons pass through the bead, the difference in refractive index leads to a momentum transfer photons→bead. The net force from the laser ‘traps’ the bead in its centre, so the bead can be moved with the laser focus. Small displacements of the bead from the centre spot are linear with force and can be described by Hooke’s law [6]. Many reports use this method to measure the force necessary to induce tethers (long lipid structures from the cell membrane) by towing a bead attached to a cell with the laser [34–36], see Fig. 2.2.

Optical traps have excellent force resolution but the magnitude of forces they can apply are limited to the $\sim 10^{-3}$ nN range. Larger forces need high laser powers, which damage cells. They have been used to detect forces produced by molecular motors [37] but cannot generate sufficient force to induce growth cone advance [6].

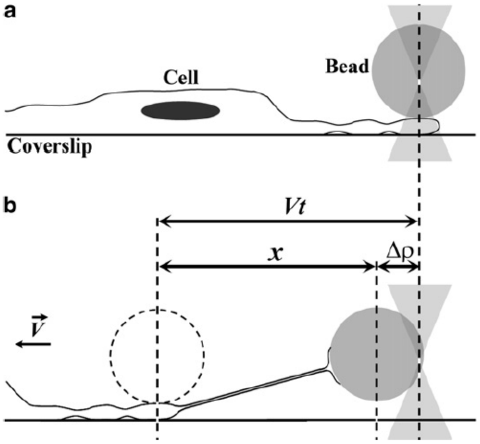

Figure 2.2 Schematic of a tether extraction experiment with optical tweezers. **(a)** Initial position. **(b)** The sample is moved relative to the laser with velocity V for time t. The change in position of the bead relative to its equilibrium position near the laser centre is $\Delta\rho$. This figure was published in Biophysical Journal, Volume 101, B Pontes *et al.*, Cell cytoskeleton and tether extrction, pp43, Copyright Cell Press (2011).

2.5 Atomic Force Microscopy

Atomic force microscopy (AFM) is a scanning probe technique capable of resolving nano-scale features [46]. It probes a sample with a sharp tip attached to a cantilever. The tip-sample interaction forces are measured by combining the deflection of a cantilever with its stiffness. The cantilever deflection is measured by the reflection of a laser off the back of the cantilever onto a position-sensitive photodiode [46]. Generally, the sample rests on a piezo-actuated stage that can control its location relative to the tip to nano-scale precision.

AFM has several different modes of operation; here we list some that are relevant to biology:

- **Contact mode**: the tip touches the sample surface and the cantilever is deflected by tip-sample repulsive force. This generates images representing contours of constant force. Previous work in our group [38] acquired images of fixed hippocampal and dorsal root ganglion (DRG) neurons treated with different quantities of vinblastine, which prevents polymerization of tubulin and induces depolymerization of formed tubules, to characterize their morphology, Fig. 2.3.

- **Lateral Force Microscopy**: a form of contact mode in which the cantilever scans the sample measuring the variation of lateral forces. It acquires information on tip-sample friction. Ref. [40] measured the pushing forces at the leading edges of growth cones of NG108-15 cells by letting the growth cones approach and push the cantilever from the side.

- **Force-Distance Spectroscopy**: simplistically, the cantilever approaches the sample, pokes it, then retracts while its deflection is recorded. This gives information about the forces as a function of distance including those arising from tip-sample interactions such as van der Waals, electrostatic forces, or hard repulsion or viscoelastic deformation [41]. This can be done at a single location or the cantilever can scan the sample, acquiring force-distance curves (cantilever deflection force versus its position) at specified grid points creating a force map. Ref. [38] also applied this method to investigate axonal response to compression and obtain the elastic modulus of axons. Ref. [48] created stiffness maps of dendritic spines (see Fig. 2.4), which are sites of excitatory synaptic contact along the dendrite. They used force-distance curves to identify relatively hard and soft regions in dendrites.

- **Non-contact mode**: The cantilever does not contact the sample, instead oscillates near resonance frequency in close proximity to the sample. Tip-sample interactions result in changes in resonant frequency or amplitude that are measured to create a topographic image of the sample surface. Although this mode has some advantages over other modes (it can be less invasive), it is challenging to perform in a liquid environment because the liquid can dampen certain resonance peaks and create others, obscuring the cantilever resonance frequency. Ref. [42] used this method to capture AFM images of live neuronal growth cones.
- **Intermittent-contact mode (Tapping mode)**: Similar to non-contact mode, here the cantilever oscillates at or near resonance frequency. Height differences in the sample change the cantilever oscillation and this is used to adjust tip-sample distance, either by feedbacking on corresponding frequency or amplitude resonance shifts [44,45]. In an ideal set-up, the tip only contacts the sample at the end of its downward motion to minimize friction between the tip and the sample. This avoids lateral forces and thus shear forces, which can easily destroy fragile biomembranes. Use of this mode is demonstrated in Ref. [43] where circular plasmid DNA was imaged in buffer solution.

AFM can also be used as a micromanipulation tool, see Fig. 2.5. This thesis is based on groundbreaking work in our group that used a cantilever with a microbead glued to its tip to induce the formation of a neurite from a parent axon or dendrite [13]. This work also demonstrated how AFM can be combined with fluorescence measurements to monitor different aspects of biological phenomena.

Due to its high imaging resolution, positional accuracy and versatility, AFM is an important tool in the biophysics community [16]. However, notable disadvantages are its invasiveness (the forces it applies can damage cells) and the fact that the calibration process can be involved [6]. Also, obtaining the compressive elastic modulus from AFM is model-dependant and requires information on both the shape of the AFM tip and the depth of indentation, which can make experiments with different AFM instruments/tips difficult to replicate [47].

Biological AFM is its own thesis topic [16, 17]. Outside of contextualizing force measurements, it is relevant to this thesis for two reasons. The first is that, as mentioned, AFM was used as an intermediate step on the road to developing our micropipette force probe. Before a micropipette, AFM was used to elongate neurites in our lab. We thus have data to compare and validate our measurements. The second reason is tangential: we use force spectroscopy to calibrate the stiffness constants of our micropipettes.

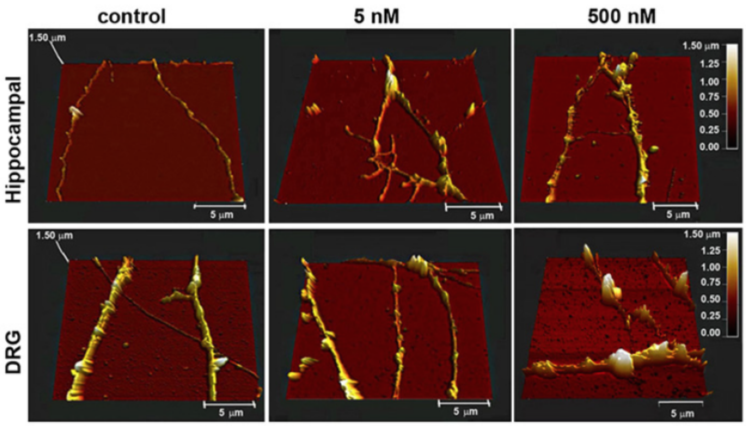

Figure 2.3 AFM images of hippocampal and DRG axons not treated or treated with 5 nM or 500 nM vinblastine. This figure was published in Biophysical Journal, Volume 103, M. H. Magdesian *et al.*, Atomic force microscopy reveals important differences in axonal resistance to injury, pp 410, Copyright Cell Press (2012).

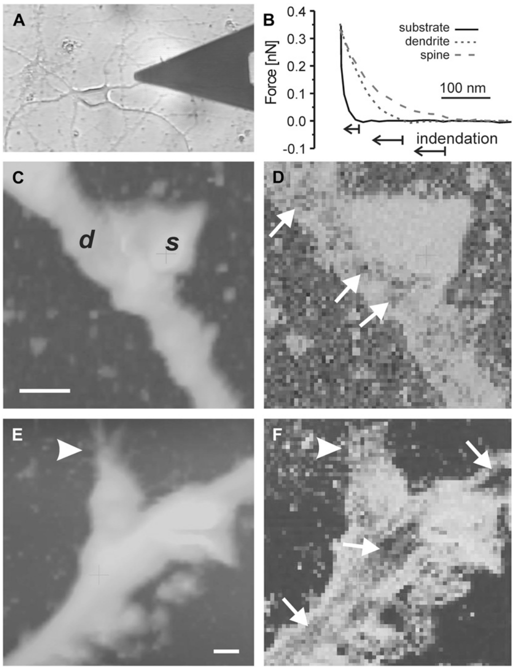

Figure 2.4 Soft dendritic spines. **(a)** Image of a cultured hippocampal neuron being scanned with an AFM probe. **(b)** Representative force-distance curves acquired during scan imaging regions of a spine, dendrite, and substrate (as indicated). **(c, e)** Topography (under constant force) maps of two dendrites with spines (labeled d and s in **(c)**). Vertical color scale is 0.5 μm in **(c)** and 0.5 μm in **(e)**. Lateral bar is 1 μm in both. **(d, f)** Corresponding stiffness maps (bright is soft, dark is stiff). Spines appeared soft relative to dendrite shafts, where stiff patches or fibers were identified (small arrows). Spine shapes were irregular, often exhibiting small surface protrusions (arrowheads). This figure was published in Biophysical Journal, Volume 92, B. A. Smith, Dendritic spine viscoelasticity and soft-glassy nature: balancing dynamic remodeling with structural stability, pp1425, Copyright Cell Press (2007).

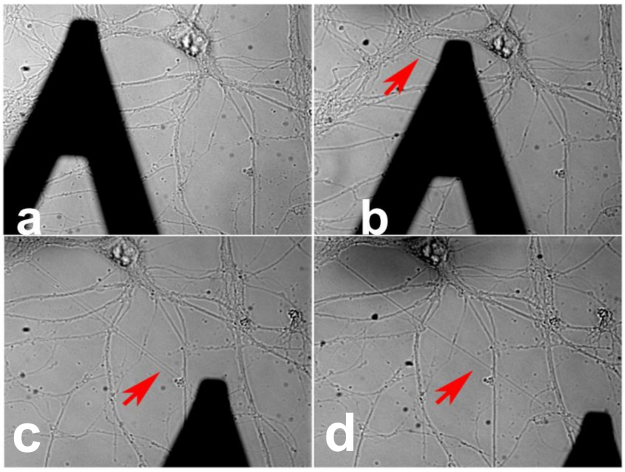

Figure 2.5 Initiation, elongation and connection of multiple neuron filaments with AFM. **(a)** A PDL-bead attached to the tip of an AFM microscope was brought in contact with bundles of neurites for 30 minutes. **(b)** Next, the AFM tip was moved 15 μm away from the sample enabling the visualization of several neurites (red arrow) attached to the PDL-bead. **(c-d)** Upon micromanipulation of the AFM tip, neurites (red arrows) can be extended over more than 90 μm in less than 5 minutes. From Ref. [16], Copyright G. M. Lopez Ayon.

Chapter 3

Morphological Characterization Techniques

3.1 Introduction

In this section I give an overview of some techniques used to study the geometric properties of neurons and the relationships between their structures. I also give a lightning review of the underlying physical concepts. The goal of this will be to provide the reader with an understanding of the capabilities and limits of current state-of-the-art technologies in order to set the stage for the results presented in Ch. 7.

3.2 Traditional Microscopy

3.2.1 Diffraction Theory Concepts

The physical limitations of the optical microscope are due to a phenomenon called diffraction. The intensity distribution of an optical wave that travels a given distance in free space *after* either being transmitted through an aperture in an opaque screen or encountering an object is known as the diffraction pattern. In the ray-optics-description of light, we expect the aperture pattern to correspond to a shadow of the aperture or a shadow in the shape of the object. However, Huygens's description of light as a wave, which can be modelled as a series of 'wavelets' or points that emanate light in all directions and travel on a wavefront gives an intuition for the ability of light to bend slightly at the edges of an object or an aperture, see for example Fig. 3.1. Coherent wavelets (that is wavelets originating from the same source at the same time—such as a single point source of light that goes through two slits) can create standing waves of constructive and destructive interference. To understand how the resolution of an optical micro-

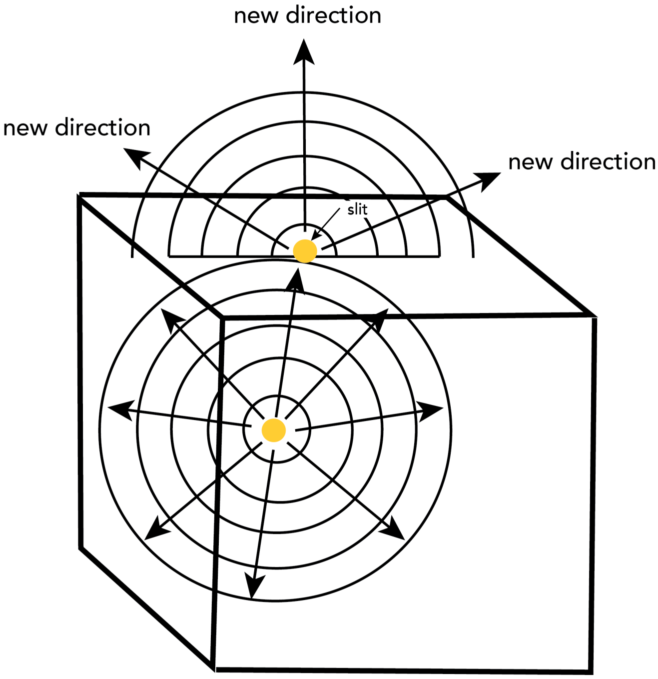

Figure 3.1 Imagine a point source in a box with a slit so small that only a single wavelet could get through it at once. The wavelet emerges from the slit, and emits light in all directions. The point source itself will be emitting light in all directions and you can trace paths from the point source that are not straight lines. Adapted from `https://www.ibiology.org/talks/resolution-in-microscopy/`, Copyright iBiology.

scope emerges from these ideas, consider the simplified schematic of microscope lenses, Fig. 3.2. The diagram shows a point source in the specimen plane emitting diverging spherical waves. A sub-portion of the spherical wave is collected by the microscope objective (red and green arrows in Fig. 3.2) and converted into plane waves that travel through the microscope tube until reaching the tube lens (labeled in Fig. 3.2). The tube lens converts the plane waves to converging spherical waves that travel to the image plane and form a spot.

The resolution of a given objective is set by its numerical aperture, $NA = n\sin(\alpha)$, where n is the index of refraction of the material between the microscope and the slide and α is the half-angle over which the objective can collect light from the source (red and green arrows in Fig. 3.2) so a higher NA collects a larger light cone—again compare green arrows in Fig. 3.2(a) and red arrows in Fig. 3.2(b). This is the critical feature for resolution. In the higher resolution configuration in Fig. 3.2(a), the points A and B in the wavefront generate a smaller blur in the image plane than the lower resolution case in Fig. 3.2(b). The radius of the blur is "an inverse measure of resolving power and image quality" [79]. Another way to understand this is to consider the description of a light wave in Fourier space. A larger NA collects the higher frequency Fourier components of the wave and thus allows the reconstruction of a higher spatial resolution image.

At the centre of the image plane, all the wavelets on the converging spherical wavefront (red box in Fig. 3.2(a)) are in phase, the light is concentrated at the centre relative to the converging spherical wave in a single main peak. The effect of all the wavelets (an infinite number on the wavefront) is the point spread function (PSF). In this sense, the PSF can be thought of as the impulse response of an imaging system.

The light distribution from a point source is the PSF. Mathematically, if the source is on axis, the PSF of an idealized system with aperture size D can be described by an Airy function,

$$I_0(x,y) = \left(\frac{\pi D^2}{4\lambda d}\right)^2 \left[\frac{2J_1(\pi D\rho/\lambda d)}{\pi D\rho/\lambda d}\right]^2,$$

$$\rho = \sqrt{x^2 + y^2}, \tag{3.1}$$

where x, y are coordinates in the image plane, λ is the wavelength of light, d is the propagation distance of light beyond the aperture and J_1 is the Bessel function of order 1. In a single plane, this pattern consists of a central disk surrounded by rings. The radius of this disk, known as the Airy disk, is $\rho_d = 0.61\lambda/NA$. The Airy disk determines how close two equal point sources can be in the field of view and still be resolved as separate objects, this is known as the Rayleigh Criterion. Though it is arbitrary, the Rayleigh Criterion is generally accepted as a limit of resolution.

3.2.2 Bright-field Imaging

In bright-field microscopy, the sample is illuminated with white light from above (or below) and observed from below (or above).

In classic fluorescence microscopy, the image, $I_{\text{em}}(\mathbf{x})$ at a postion $\mathbf{x}$, can be expressed as the convolution of the product of the illumination source, $I_{\text{ex}}(\mathbf{x})$, a constant, and the sample distribution $s(\mathbf{x})$ with the PSF:

$$I_{\text{em}}(\mathbf{x}) = (I_{\text{ex}}(\mathbf{x})s(\mathbf{x})) \circledast \text{PSF}(\mathbf{x}). \tag{3.2}$$

Recall the spatial resolution is limited by the PSF. The corresponding quantity in Fourier space is given by

$$I_{\text{em}}(\mathbf{k}) = (I_{\text{ex}}(\mathbf{k}) \circledast S(\mathbf{k}))\text{OTF}(\mathbf{k}), \tag{3.3}$$

where $\mathbf{k}$ is the spatial frequency and $I_{\text{em}}(\mathbf{k})$, $I_{\text{ex}}(\mathbf{k})$, $S(\mathbf{k})$ and $\text{OTF}(\mathbf{k})$ are the respective Fourier transforms of $I_{\text{em}}(\mathbf{x})$, $I_{\text{ex}}(\mathbf{x})$, $s(\mathbf{x})$ and $\text{PSF}(\mathbf{x})$.

If the PSF of the microscope is known, the intensity distribution of the object can be precisely obtained through deconvolution.

For bright-field microscopy, the deconvolution process is more complicated because the PSF is not unique. Ref. [80] showed that the image formation process is described by two different PSFs: one that captures the phase structure of the object $\mathrm{PSF_P}$ and one that captures the absorption structure $\mathrm{PSF_A}$. The 3D intensity distribution of the object I_{em} is given in terms of the real part P and the imaginary part A of the scattering potential [80, 81]

$$I_{\mathrm{em}} = P \circledast \mathrm{PSF_P} + A \circledast \mathrm{PSF_A} + B, \tag{3.4}$$

where B is background light that does not interact with the sample. In most biological applications of the bright-field microscope, samples are near-transparent and it suffices to treat them as pure phase objects and consider only the contributions of $\mathrm{PSF_P}$ [80, 81, 83]. The phase PSF is phenomenologically modelled in Ref. [81]. It is shown to depend on a constant phase caused by the difference in refractive index between the sample and the medium $\delta = (4\pi w/3\lambda)(n_{\mathrm{sample}} - n_{\mathrm{medium}})$, where w is the thickness of the sample. This will be relevant to the results presented in Ch. 7.

Apart from the additional challenges of applying deconvolution, bright-field microscopy suffers from poor contrast [81, 83]. However, given its simplicity and the fact that unstained samples can be observed continuously for long periods of time (several hours), it can be more convenient in certain contexts than fluorescence microscopy. Several techniques have been developed to circumvent challenges to bright-field. Ref. [84] demonstrated the visualization of microtubules with a conventional bright-field set-up. They developed a technique called computer enhanced bright-field imaging, which involves averaging over multiple frames, background subtraction, spatial filtering, smoothing and enhancing images with spatial convolution routines. Ref. [81] used this technique to experimentally prove the theoretical underpinnings of image formation summarized in this section. Ref. [83] used out-of-focus imaging to characterize fluctuations on the surfaces of cells. In Ch. 7, we also use out-of-focus images and further show how this can be used to quantify sub-resolution objects.

3.3 Super-resolution Microscopy

Since the 17th century, the microscope has been the ‘workhorse’ of biological studies. As discussed in the previous section, diffraction limits this technique to a resolution of $d \sim \lambda/(2NA)$, which is commonly taken to be $\sim$ 250 nm [53]. However, many cellular processes and structures occur at the macro-molecular scale. These require greater resolution to detect.

The term ‘super-resolution’ refers to the family of techniques used in light microscopy to circumvent the optical diffraction limit. Over the past 20 years, many powerful and versatile tools have emerged that enable the observation of cellular nano-architecture and dynamics (see Ref. [51] for a review). In 2014, the Nobel Prize in Chemistry was awarded to three scientists, Betzig, Hell and Moerner “for the development of super-resolved fluorescence microscopy” [52]. Here I identify some of these techniques as well as the neuroscience insights they have enabled.

Single Molecule Localization Microscopy

“How precisely can the position or location of a single molecule be determined?” [54]. In conventional microscopy (that is a widefield microscope with a camera detector), the image of a point-like emitter is a blur, the PSF. While details within the blur are obscure, information like its centre can be extracted and used to localize the emitter with precision much greater than the diffraction limit [53, 56].

The concept of single-molecule localization is important for single particle tracking techniques as well as super-resolution imaging approaches. It is relevant to the measurement techniques developed in both Chapters 6 and 7 of this thesis and so I will spend some time here detailing the factors affecting its limitations. I follow Section 2.2 of Ref. [54].

Noise in single-molecule localization arises from photon shot noise (Poisson noise) as well as background noise. Detectors have ‘dark noise’ due to the thermal current in the photon→photoelectron conversion process as well as ‘read noise’ due to the conversion of the photocurrent of each pixel to a voltage.

In an idealized system, the image of a point emitter can be mathematically described by a cross-section of the system's 3D PSF, scaled by the number of photons from the signal, N_{sig}, and added to a number of background photons per unit area, N_{bg}, a constant. The intensity distribution of the emitter, in image plane coordinates, u, v, is given by

$$I(u, v) = H(x, y, z, N_{sig}, N_{bg}) = H(\theta), \tag{3.5}$$

where x, y, z are the position coordinates of the emitter in the specimen space and θ sums up the parameterizations of the PSF.

In an image from a real experiment, each pixel w_k in the region of interest (ROI) will have some signal n_k that is a combination of signal and noise. Given some knowledge of H together with the noisy image vector $\mathbf{n}$, how well can the position of the object, $\mathbf{x} = (x, y, z)$, be determined?

Based on the fact that the brightest region of the PSF corresponds to the position of the molecule, a weighted average of N pixels in the ROI is a reasonable estimator,

$$(x_c, y_c) = \left(\frac{\sum_k^N n_k x_k}{\sum_k^N n_k}, \frac{\sum_k^N n_k y_k}{\sum_k^N n_k} \right). \tag{3.6}$$

This quantity is known as the centroid estimator and it is often exploited in this thesis. It is computationally tractable though it is also sensitive to bias from background outlying pixels.

A more accurate and precise approach to finding a position estimator is to solve the inverse problem in Eq. 3.5 with a detailed PSF model and a method such as least-squares or maximum likelihood estimation. In the least-squares approach, the mean square error,

$$S = \sum_k^N [n_k - \mu_k]^2, \tag{3.7}$$

where $\mu(\theta)$ is the PSF model, is minimized.

To obtain a model for H that gives I, we assume the case of an ideal, focused emitter. As mentionned, this is described by an Airy function. However, in realistic experimental conditions, there is insufficient precision to distinguish an

Airy function from a Gaussian [50, 53, 57] and it is common practice to fit the image of the PSF with a Gaussian plus a constant:

$$I(u,v) = \frac{N_{sig}}{2\pi\sigma_{\mathrm{PSF}}^2} \exp\left(-\frac{\rho^2}{2\sigma_{\mathrm{PSF}}^2}\right) + N_{bg}, \tag{3.8}$$

where $\rho = \sqrt{(u-u_c)^2 + (v-v_c)^2}$ is the distance from the emitter in the image plane and σ_{PSF} is the size of the blur determined by the diffraction limit. The precision of this can be tested by applying it to many images of the same molecule. Ref [54] finds a localization precision of $\sim$ 10 nm. Note that using a so-called maximum estimator (assuming the location of the molecule corresponds to the maximum intensity) gives a precision of $\sim$ 34 nm—worse but more than sufficient for the applications in this thesis. Ref. [53] uses Eqs. 3.7&3.8 to derive an expression for the precision to which an emitter can be localized, σ,

$$\sigma \propto \frac{\sigma_{\mathrm{PSF}}}{\sqrt{N_{sig}}}. \tag{3.9}$$

This expression ignores pixelation and assumes a negligible background but shows the importance of high photon counts.

There are many strategies to localize the PSF centre (see e.g. Refs. [50,53,54]) and these can be broadly categorized based on whether or not the rely on the fitting of a PSF model function to the image. For our purposes, it is important to consider the noise sources affecting the accuracy and precision of the measurement and to have an intuition for the importance of signal photons.

The above discussion applies to the case of a single emitter in the field of view; it does not apply to multiple, overlapping PSFs. The mechanism underlying single-molecule-localization-microscopy (SMLM) limits the number of emitting particles in the field of view at a given time. Tens of thousands of frames are collected of the sample, each showing a small number of isolated emitters. The information from the PSFs in each image is combined into a single image of the sample that can resolve details with a $\sim 20-30$ nm resolution.

Different modalities of SMLM have lead to important neuroscience discoveries. For example, Ref. [58] exploited the axonal transport process to separate fluorophores and resolve densely packed microtubules. By tracking endosomes containing quantum dots that are transported along unlabeled microtubules, individual microtubules could be resolved in axons and it was observed that endosomes switched microtubule ‘tracks’—an important insight into axonal transport. Refs. [59–61] used stochastic optical reconstruction microscopy (STORM), a modality of SMLM to revolutionize our understanding of dynamic actin organization along the axon. Ref. [59] reported stable actin rings that wrapped the circumference of the axonal shaft, spaced periodically along its long axis. Ref. [61] used STORM to detect these rings along the initial segment of the axon. In addition to the rings, Ref. [60] observed periodic regions of actin assembly and disassembly, so called ‘actin hotspots’.

Structured Illumination Microscopy

The working principle of structure illumination microscopy (SIM) is that the illumination intensity, $I_{\mathrm{ex}}(x)$ in Eq. 3.3, is varied spatially so the convolution of $I_{\mathrm{ex}}(x)$ with $S(k)$ is non-local [62–64]. As a consequence, information within the detection passband (i.e. the circle in frequency space with radius $k_{pb} = 2NA/\lambda_{em}$) can be dependant on frequency-space modes generated by the sample which are outside the passband [63, 64]. In SIM, the sample is illuminated with a series of periodic light patterns with high spatial frequencies and the resulting signal is recorded for each pattern. These illumination patterns are typically produced with a laser and a movable grating [49]. The images resulting from each different illumination pattern can be analyzed with algorithms to generate a single, higher resolution image. This technique can resolve details about a factor of 2 better than classic microsocpy [61].

SIM has been used to explore cytoskeleton dynamics. One application has been to elucidate fluctuations in the motion of actin bundles in the developing neuron at the stage before the axon differentiates from other neurites [65].

Ref. [66] used SIM to explore the actin-ring structure discussed in the previous section. Though it operates at a slightly lower resolution than SMLM methods, SIM can capture the periodic structure in several axons and enable network statistics, ultimately revealing the role of 11 different actin regulators.

Stimulated Emission Depletion Microscopy

In stimulated emission depletion microscopy (STED), the sample is scanned with a laser set-up that applies two synchronous pulses: one pulse to stimulate fluorophores into their excited state (a laser photon gives energy to an electron to jump to an excited state) and one pulse to induce stimulated depletion [67]. In stimulated depletion, an incident photon interacts with an electron in an excited state and causes it to transition to a lower energy state. This second pulse limits the fluorescent emission so the PSF can be compressed below the optical diffraction limit.

STED is also used to identify a periodic actin-ring structure throughout the axon [68, 69]. Ref. [68] engineered probes composed of silicon-rhodamine (SiR) that in equilibrium exist in both a fluorescent 'on' state and an 'off' state. The SiR-based fluorophores were attached to ligands that bind to both microtubules and F-actin. Ref. [69] also exploited an SiR-based probe to observe actin rings in axons and dendrites. STED has also been used to characterize the actin structure in regions surrounding synapses [72]. Interestingly, actin rings are absent in these areas.

Closing Thoughts

Super-resolution microscopy is a rapidly developing field that has already proven to be extremely powerful in its capabilities. While these techniques have lead to important discoveries, they have also unearthed many more questions. Three-dimensional imaging is a feature of each technique that was not directly discussed. These techniques also have disadvantages. They all require specialized equipment such as lasers and both SMLM and STED require specialized probes that can be sample-dependent. Finding a good sample-preparation recipe to perform the desired experiment can be a multi-month enterprise and can ultimately limit which experiments can be performed [68, 70]. Probes could interfere with the regular dynamics of the cell. Another major disadvantage for some super-resolution techniques relying on probes is the risk of photo-toxicity and photo-bleaching since neurons are photo-sensitive [81, 82].

We focus the discussion on techniques most commonly used by neuroscientists [51] but there are many super-resolution methods not detailed here (e.g. total internal reflection fluorescence microscopy and scanning near-field optical microscopy) as well as some resolution enhancement techniques that do not qualify as 'super' (confocal laser scanning microscopy).

3.4 Electron Microscopy

Electron microscopy is a technique for 3D imaging that uses an electron beam instead of photons to probe samples. There are two principle types of electron microscope: transmission EM (TEM) and scanning EM (SEM). In TEM, electrons pass through the sample to generate the image, analogous to classic light microscopy. It is generally applied to thin specimens. In SEM, the electron beam scans a rectangular area of the sample. The beam-sample interaction converts beam electron energy to forms such as heat, secondary electrons of lower energy, backscattered electrons of higher energy, light emission and X-ray emission. These signals are collected and combined to construct an image of the sample surface. In general, TEM has better resolution but SEM has a better depth of field so can capture 3D surface maps of larger samples. SEM captures details on the order of ~ 1 nm while TEM can capture details down to 0.01 nm.

EM was first use to identify fibrils in neurites that would come to be known as microtubules and neurofilaments [51, 73]. It revealed for the first time the extent to which the cytoskeleton structure is complex and intricate, with a network of branching structures and cross-linkers [74, 75].

EM results shaped our perspective on the cytoskeleton. However, it has limitations. Sample-preparation can be tricky and can destroy delicate structures researchers seek to observe (such as neurites suspended off the coverslip) [51, 71]. It is also unable to resolve proteins in the cytoskeleton. Furthermore, samples must be fixed so it cannot capture cell dynamics. This is eliminates the possibility of measuring cell morphology in response to deformations.

3.5 Atomic Force Microscopy II

AFM belongs as a section here too. As well as forces, it is a tool to characterize cell morphology. It has been used to image neurons (again see Fig. 2.3 [38]), as well as microtubules and other cytoskeleton structures [76]. Amazingly, high-frequency AFM was used to directly observe the motion of the molecular motor myosin V along actin [77]. However, AFM cannot measure structures that are not fixed to the coverslip so it cannot be applied to neurites suspended like telephone cables between two fixed points on a coverslip.

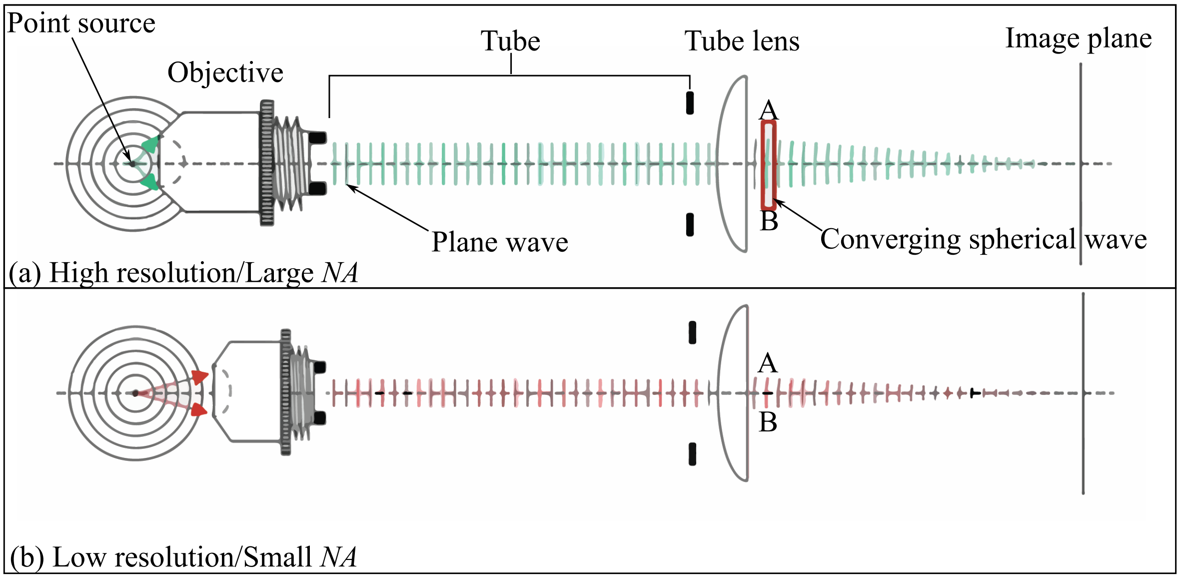

Figure 3.2 Schematic of the wave path in an optical microscope for **(a)** a high NA objective and a **(b)** low NA objective. In both set-ups, a point source on the optical axis emits diverging spherical waves. A portion of these get collected by the objective, the size of the arc collected is dependant on the objective NA, and converted into plane waves. The plane waves travel along the tube until they encounter the tube lens where they get transformed into converging spherical waves. These travel to the image plane. A converging spherical wave from the high NA configuration is marked in a red box. Points A and B in both configurations label extreme points on the wavefronts. These points are sources of wavelets in the Huygen's picture. Adapted from `https://www.ibiology.org/talks/resolution-in-microscopy/`, Copyright iBiology.

Chapter 4

Lightning Review of Continuum Mechanics

4.1 Introduction

In this chapter we introduce continuum mechanics, the mathematical framework used to describe the response of solid materials to mechanical deformations. Definitions introduced here will be important for treating quantities discussed in Ch. 8. We follow Refs. [5, 78].

4.2 Deformation Measures

Consider an undeformed material contained in a volume $\mathcal{B} \in \mathbb{R}^3$. The displacement field, $\mathbf{u(x)}$, maps every point $\mathbf{x} \in \mathcal{B}$ to another point $\mathbf{y} \in \mathbb{R}^3$. For example, a volume-preserving uniaxial extension is given by

$$\begin{aligned} y_1 &= \lambda x_1 \\ y_2 &= \lambda^{-1/2} x_2 \\ y_3 &= \lambda^{-1/2} x_3, \end{aligned} \tag{4.1}$$

where $\lambda > 0$ is a constant, the x_i's and y_i's are cartesian coordinates.

Shape changes in a material are described by the deformation gradient,

$$F_{ij} = \delta_{ij} + \frac{\partial u_i}{\partial x_j}, \tag{4.2}$$

where $u_i = y_i - x_i$. The Jacobian, $J = \det(\mathbf{F})$, captures the volume change in the material and is 1 for constant volume deformations.

It is common practice to characterize deformations with the left and right Cauchy-Green deformation tensors, $\mathbf{b}$ and $\mathbf{C}$, which are defined in terms of $\mathbf{F}$:

$$\begin{aligned} \mathbf{b} &= \mathbf{F} \cdot \mathbf{F^T} \\ \mathbf{C} &= \mathbf{F^T} \cdot \mathbf{F}. \end{aligned} \tag{4.3}$$

With these, we can construct the invariants of the left and right Cauchy-Green deformation tensors,

$$\begin{aligned} I_1 &= \mathrm{trace}(\mathbf{b}) = \mathrm{trace}(\mathbf{C}) \\ I_2 &= \frac{1}{2}\left[(\mathrm{trace}(\mathbf{b}))^{\mathbf{2}} - \mathrm{trace}(\mathbf{b^2})\right] = \frac{1}{2}\left[(\mathrm{trace}(\mathbf{C}))^{\mathbf{2}} - \mathrm{trace}(\mathbf{C^2})\right] \\ I_3 &= J^2 = \det(\mathbf{b}) = \det(\mathbf{C}). \end{aligned} \tag{4.4}$$

The eigenvalues of $\mathbf{b}$ and $\mathbf{C}$ are called the stretches, λ_i, and these are commonly used to characterize the deformation-response of neurons. For the case of 1-D uniform stretching along an axis (as is the configuration for the experiments described in this thesis), we define the axonal stretch, $\lambda = l/L$, which is the ratio between the unstretched length L and the stretched axonal length l.

Specific materials have associated constitutive relations that capture the relation between the force on the material at any $\mathbf{x}$ and t. These are modelled by the strain-energy function Ψ, which has phenomenologically determined parameters. Some examples of strain-energy functions are listed in Table 4.1.

The strain-energy function can be used to define the Piola stress P, which is the stress across a neurite

$$P = \frac{\partial \Psi}{\partial \lambda}. \tag{4.5}$$

Name	Definition
Neo-Hookean	$\Psi_{nh} = (I_1 - 3)/2$
Mooney-Rivlin	$\Psi_{mr} = c_1[I_1 - 3] + c_2[I_2 - 3]$
1-term Ogden	$\Psi_{og} = 2\nu^{-2}(\lambda_1^\nu + \lambda_2^\nu + \lambda_3^\nu - 3)$
Fung	$\Psi_{fu} = \alpha^{-1}(\exp[\alpha(I_1 - 3)] - 1)$
Gent	$\Psi_{ge} = -\beta^{-1}\log[1 - \beta(I_1 - 3)]$

Table 4.1 Some examples of strain-energy functions [85]. α, $c_1, c_2, \nu, \alpha, \beta$ are material constants.

4.3 Principle of Virtual Work

As mentioned in Sec. 2.2, the stress-stretch relation of neurites has been extensively studied using calibrated microneedles [10,21–24,39]. In this technique, the neurite is pulled and the equilibirum between the applied force and the deformation of the material is measured.

The principle of virtual work is applied in this context by minimizing the total work, which is given as the sum of the internal work W^i and the external work W^e. Here

$$W^\mathrm{i} = \int_\mathcal{B} \Psi dV \tag{4.6}$$

is the work of the neurite to deform in response to stretch. It is common to model the deformation as well as the cross section A as homogenous along the length L of the neurite so $\int_\mathcal{B} dV \to AL$. The external work W^e is the response of the microneedle as it pulls the axon with a force F to create a deformation ϕ,

$$W^\mathrm{e} = -F\phi. \tag{4.7}$$

The minimization of the total work gives the condition that the first variation with respect to ϕ must vanish:

$$\delta W = \delta W^\mathrm{i} + \delta W^\mathrm{e} \doteq 0 \ \forall \delta\phi \tag{4.8}$$

Taking the variations of Eqs. 4.6&4.7 and inserting these into Eq. 4.8 gives

$$\delta W = \left[PAL\frac{d\lambda}{d\phi} - F \right] \delta\phi \doteq 0 \ \forall \delta\phi, \tag{4.9}$$

which yields the force-deformation relation for a pulled neurite:

$$F = PAL\frac{d\lambda}{d\phi}. \tag{4.10}$$

In the experiments described in this thesis, we pull the end of a neurite in the direction parallel to its long axis (i.e. we pull axially). The deformation is given by $\phi = L + \Delta L = l$ so $d\lambda/d\phi = 1/L$ and Eq. 4.10 becomes

$$F = PA. \tag{4.11}$$

4.4 Growth with Elastic Deformation in 1 Dimension

There is an important relationship between growth, the process by which a body changes size through the addition of mass, and stress. Stress can drive growth and growth can induce stress, especially if a body is inhomogenous and/or undergoing differential growth. Continuum mechanics is a convenient framework to study biological growth because it captures the fact that a deformation can be due to a (nonlinear) elastic response and due to the addition of mass.

Ref. [5] describes the theoretical framework of morphoelasticity in 1D that models stretch as the product of a stretch contribution from elasticity λ^e and a stretch contribution from growth λ^g,

$$\lambda = \lambda^e \lambda^g. \tag{4.12}$$

We assume that stress is only caused by λ^e and not by λ^g—a commonly adopted assumption in growth theories. Eq. 4.12 tells us what part of neurite deformation is due to added mass (growth) and what part is due to the elastic stretching of material present in the neurite.

To link this to force-deformation measurements, we first reparameterize the strain-energy function in terms of the elastic stretches. For example, the Mooney-Rivlin model from Table 4.1 becomes $\Psi = c_1[I_1 - 3] + c_2[I_2 - 3] \rightarrow \Psi = c_1[I_1^e - 3] + c_2[I_2^e - 3]$. Note that I_i^e can be written in terms of the stretches, $I_i^e = f(\lambda_1^e, \lambda_2^e, \lambda_3^e)$ so we can write the strain-energy functions in terms of λ^e, $\Psi = \Psi(\lambda^e)$.

This can in turn be reparameterized in terms of λ, λ^g: $\Psi(\lambda^e) \rightarrow \Psi(\lambda, \lambda^g)$. Using

$$\begin{aligned} P &= \frac{\partial \Psi}{\partial \lambda} \\ &= \frac{\partial \Psi}{\partial \lambda^e} \frac{\partial \lambda^e}{\partial \lambda} \\ &= P^e \frac{\partial \lambda^e}{\partial \lambda} \\ &= \frac{1}{\lambda^g} P^e, \end{aligned} \tag{4.13}$$

we can write Eq. 4.11 in terms of λ, λ^g.

To get a closed set of equations, we need to assume an evolution law for the growth λ^g. It is common to adopt a constitutive law of the form

$$\frac{\partial \lambda^g}{\partial t} = G(\lambda^g, \lambda). \tag{4.14}$$

For uniform growth $G = 1$ and for exponential growth $G = k\lambda^g$ for some constant k. This law can also capture the fact that neurites have been observed to have a homeostatic stress that they try to recover if they are deformed from this state by setting $G = k\Theta(\lambda^e - \lambda^*)$, where $\Theta(x)$ is a Heaviside theta function: $\Theta(x)$ is 1 for $x > 0$ and 0 otherwise and λ^* is a critical stretch associated with the homeostatic stress.

In this Chapter we have identified quantities used to characterize deformations in the context of 1D pulling experiments. These will be used and developed further in Ch. 8.

Bibliography

[1] Dennis Bray. Axonal growth in response to experimentally applied mechanical tension. *Developmental biology*, 102(2):379–389, 1984.

[2] Rijk de Rooij and Ellen Kuhl. Constitutive modeling of brain tissue: current perspectives. *Applied Mechanics Reviews*, 68(1):010801, 2016.

[3] Steven R Heidemann and Dennis Bray. Tension-driven axon assembly: a possible mechanism. *Frontiers in cellular neuroscience*, 9:316, 2015.

[4] Karol Miller, Adam Wittek, and Grand Joldes. Biomechanical modeling of the brain for computer-assisted neurosurgery. In *Biomechanics of the Brain*, pages 111–136. Springer, 2011.

[5] Alain Goriely, Silvia Budday, and Ellen Kuhl. Neuromechanics: from neurons to brain. In *Advances in Applied Mechanics*, volume 48, pages 79–139. Elsevier, 2015.

[6] Ahmad Ibrahim Mahmoud Athamneh and Daniel Marcel Suter. Quantifying mechanical force in axonal growth and guidance. *Frontiers in cellular neuroscience*, 9:359, 2015.

[7] Maria A Holland, Kyle E Miller, and Ellen Kuhl. Emerging brain morphologies from axonal elongation. *Annals of biomedical engineering*, 43(7):1640–1653, 2015.

[8] Daniel M Suter and Kyle E Miller. The emerging role of forces in axonal elongation. *Progress in neurobiology*, 94(2):91–101, 2011.

[9] Kristian Franze, Paul A Janmey, and Jochen Guck. Mechanics in neuronal development and repair. *Annual review of biomedical engineering*, 15:227–251, 2013.

[10] Matthew O'Toole, Phillip Lamoureux, and Kyle E Miller. A physical model of axonal elongation: force, viscosity, and adhesions govern the mode of outgrowth. *Biophysical journal*, 94(7):2610–2620, 2008.

[11] Bryan J Pfister, Akira Iwata, David F Meaney, and Douglas H Smith. Extreme stretch growth of integrated axons. *Journal of Neuroscience*, 24(36):7978–7983, 2004.

[12] Pierre Recho, Antoine Jerusalem, and Alain Goriely. Growth, collapse, and stalling in a mechanical model for neurite motility. *Physical Review E*, 93(3):032410, 2016.

[13] Margaret H Magdesian, G Monserratt Lopez-Ayon, Megumi Mori, Dominic Boudreau, Alexis Goulet-Hanssens, Ricardo Sanz, Yoichi Miyahara, Christopher J Barrett, Alyson E Fournier, Yves De Koninck, et al. Rapid mechanically controlled rewiring of neuronal circuits. *Journal of Neuroscience*, 36(3):979–987, 2016.

[14] Madeleine Anthonisen, Matthew Rigby, M Hussain Sangji, Xue Ying Chua, and Peter Grütter. Response of mechanically-created neurites to extension. *Journal of the mechanical behavior of biomedical materials*, 2019.

[15] Fernando Suarez, Peter Thostrup, David Colman, and Peter Grutter. Dynamics of presynaptic protein recruitment induced by local presentation of artificial adhesive contacts. *Developmental neurobiology*, 73(1):98–106, 2013.

[16] Gabriela López Ayón. *Local Mechanical Stimulation Based Approaches for the Study of Cells*. PhD thesis, McGill University Libraries, 2015.

[17] Fernando Suárez Sánchez. *AFM investigations of cellular response to environmental and local chemo-mechanical stimulus*. McGill University (Canada), 2011.

[18] Anna Lisa Lucido, Fernando Suarez Sanchez, Peter Thostrup, Adam V Kwiatkowski, Sergio Leal-Ortiz, Gopakumar Gopalakrishnan, Dalinda Liazoghli, Wiam Belkaid, R Bruce Lennox, Peter Grutter, et al. Rapid assembly of functional presynaptic boutons triggered by adhesive contacts. *Journal of Neuroscience*, 29(40):12449–12466, 2009.

[19] V. Marx. May mechanobiology work forcefully for you. *Nature Methods* 16, no. 11 (2019): 1083-1086, 2019.

[20] M. Krieg, G. Fläschner, D. Alsteens, B. M. Gaub, W. H. Roos, G. J. L. Wuite, H. E. Gaub, C. Gerber, Y. F. Dufrêne, and D. J. Müller. Atomic force microscopy-based mechanobiology. *Nature Reviews Physics* 1, no. 1 (2019): 41-57, 2019.

[21] Philip Lamoureux, Robert E Buxbaum, and Steven R Heidemann. Direct evidence that growth cones pull. *Nature*, 340(6229):159, 1989.

[22] Timothy J Dennerll, Phillip Lamoureux, Robert E Buxbaum, and Steven R Heidemann. The cytomechanics of axonal elongation and retraction. *The Journal of cell biology*, 109(6):3073–3083, 1989.

[23] Jing Zheng, Phillip Lamoureux, Vivian Santiago, Timothy Dennerll, Robert E Buxbaum, and Steven R Heidemann. Tensile regulation of axonal elongation and initiation. *Journal of Neuroscience*, 11(4):1117–1125, 1991.

[24] Matthew O'Toole, Phillip Lamoureux, and Kyle E Miller. Measurement of subcellular force generation in neurons. *Biophysical journal*, 108(5):1027–1037, 2015.

[25] TJ Dennerll, HC Joshi, VL Steel, RE Buxbaum, and SR Heidemann. Tension and compression in the cytoskeleton of pc-12 neurites. ii: Quantitative measurements. *The Journal of cell biology*, 107(2):665–674, 1988.

[26] Roberto Bernal, Pramod A Pullarkat, and Francisco Melo. Mechanical properties of axons. *Physical review letters*, 99(1):018301, 2007.

[27] Daniel Koch, William J Rosoff, Jiji Jiang, Herbert M Geller, and Jeffrey S Urbach. Strength in the periphery: growth cone biomechanics and substrate rigidity response in peripheral and central nervous system neurons. *Biophysical journal*, 102(3):452–460, 2012.

[28] Suzanne Higgins, Jeong Soon Lee, Ligyeom Ha, and Jung Yul Lim. Inducing neurite outgrowth by mechanical cell stretch. *BioResearch open access*, 2(3):212–216, 2013.

[29] Callen Hyland, Aaron F Mertz, Paul Forscher, and Eric Dufresne. Dynamic peripheral traction forces balance stable neurite tension in regenerating aplysia bag cell neurons. *Scientific reports*, 4:4961, 2014.

[30] Lisa A Flanagan, Yo-El Ju, Beatrice Marg, Miriam Osterfield, and Paul A Janmey. Neurite branching on deformable substrates. *Neuroreport*, 13(18):2411, 2002.

[31] Bryan J Pfister, David P Bonislawski, Douglas H Smith, and Akiva S Cohen. Stretch-grown axons retain the ability to transmit active electrical signals. *FEBS letters*, 580(14):3525–3531, 2006.

[32] Min D Tang-Schomer, Ankur R Patel, Peter W Baas, and Douglas H Smith. Mechanical breaking of microtubules in axons during dynamic stretch injury underlies delayed elasticity, microtubule disassembly, and axon degeneration. *The FASEB Journal*, 24(5):1401–1410, 2010.

[33] Benedikt Sabass, Margaret L Gardel, Clare M Waterman, and Ulrich S Schwarz. High resolution traction force microscopy based on experimental and computational advances. *Biophysical journal*, 94(1):207–220, 2008.

[34] Jianwu Dai and Michael P Sheetz. Mechanical properties of neuronal growth cone membranes studied by tether formation with laser optical tweezers. *Biophysical journal*, 68(3):988–996, 1995.

[35] Jianwu Dai and Michael P Sheetz. Membrane tether formation from blebbing cells. *Biophysical journal*, 77(6):3363–3370, 1999.

[36] Bruno Pontes, Nathan B Viana, Leonarde T Salgado, Marcos Farina, V Moura Neto, and H Moyses Nussenzveig. Cell cytoskeleton and tether extraction. *Biophysical journal*, 101(1):43–52, 2011.

[37] Mary Williard Elting and James A Spudich. Future challenges in single-molecule fluorescence and laser trap approaches to studies of molecular motors. *Developmental cell*, 23(6):1084–1091, 2012.

[38] Margaret H Magdesian, Fernando S Sanchez, Monserratt Lopez, Peter Thostrup, Nela Durisic, Wiam Belkaid, Dalinda Liazoghli, Peter Grütter, and David R Colman. Atomic force microscopy reveals important differences in axonal resistance to injury. *Biophysical journal*, 103(3):405–414, 2012.

[39] Phillip Lamoureux, Gordon Ruthel, Robert E Buxbaum, and Steven R Heidemann. Mechanical tension can specify axonal fate in hippocampal neurons. *The Journal of cell biology*, 159(3):499–508, 2002.

[40] Thomas Fuhs, Lydia Reuter, Iris Vonderhaid, Thomas Claudepierre, and Josef A Käs. Inherently slow and weak forward forces of neuronal growth cones measured by a drift-stabilized atomic force microscope. *Cytoskeleton*, 70(1):44–53, 2013.

[41] William F Heinz and Jan H Hoh. Spatially resolved force spectroscopy of biological surfaces using the atomic force microscope. *Trends in biotechnology*, 17(4):143–150, 1999.

[42] Ying Xiong, Aih Cheun Lee, Daniel M Suter, and Gil U Lee. Topography and nanomechanics of live neuronal growth cones analyzed by atomic force microscopy. *Biophysical journal*, 96(12):5060–5072, 2009.

[43] S. Ido, K. Kimura, N. Oyabu, K. Kobayashi, M. Tsukada, K. Matsushige, H. Yamada. Beyond the helix pitch: direct visualization of native DNA in aqueous solution. *ACS nano*, 7(2), 1817-1822, 2013.

[44] Y. F. DufrŘne, T. Ando, R. Garcia, D. Alsteens, D. Martinez-Martin, A. Engel, C. Gerber, D. J. M§ller. Imaging modes of atomic force microscopy for application in molecular and cell biology. *Nature nanotechnology*, 12(4), p.295, 2017.

[45] P. K. Hansma, J. P. Cleveland, M. Radmacher, D. A. Walters, P. E. Hillner, M. Bezanilla, M. Fritz et al. Tapping mode atomic force microscopy in liquids. *Applied Physics Letters* 64, no. 13 (1994): 1738-1740, 1994.

[46] G. Binnig, C. F. Quate, and Ch. Gerber. Atomic force microscope. *Phys. Rev. Lett.*, 56:930–933, Mar 1986.

[47] Kweku A Addae-Mensah and John P Wikswo. Measurement techniques for cellular biomechanics in vitro. *Experimental biology and medicine*, 233(7):792–809, 2008.

[48] B. A. Smith, H. Roy, P. De Koninck, P. Gr§tter, and Y. De Koninck. Dendritic spine viscoelasticity and soft-glassy nature: balancing dynamic remodeling with structural stability. *Biophysical journal* 92, no. 4 (2007): 1419-1430.

[49] Lothar Schermelleh, Rainer Heintzmann, and Heinrich Leonhardt. A guide to super-resolution fluorescence microscopy. *The Journal of cell biology*, 190(2):165–175, 2010.

[50] Hao Shen, Lawrence J Tauzin, Rashad Baiyasi, Wenxiao Wang, Nicholas Moringo, Bo Shuang, and Christy F Landes. Single particle tracking: from theory to biophysical applications. *Chemical Reviews*, 117(11):7331–7376, 2017.

[51] Christophe Leterrier, Pankaj Dubey, and Subhojit Roy. The nano-architecture of the axonal cytoskeleton. *Nature Reviews Neuroscience*, 18(12):713, 2017.

[52] `https://www.nobelprize.org/prizes/chemistry/2014/press-release/` 2014

[53] Russell E Thompson, Daniel R Larson, and Watt W Webb. Precise nanometer localization analysis for individual fluorescent probes. *Biophysical journal*, 82(5):2775–2783, 2002.

[54] Alex von Diezmann, Yoav Shechtman, and WE Moerner. Three-dimensional localization of single molecules for super-resolution imaging and single-particle tracking. *Chemical reviews*, 117(11):7244–7275, 2017.

[55] Jeff Lichtman. Resolution of a Microscope. `https://www.ibiology.org/talks/resolution-of-a-microscope/` 2012.

[56] Norman Bobroff. Position measurement with a resolution and noise-limited instrument. *Review of Scientific Instruments*, 57(6):1152–1157, 1986.

[57] Alex Small and Shane Stahlheber. Fluorophore localization algorithms for super-resolution microscopy. *Nature methods*, 11(3):267, 2014.

[58] Harsha V Mudrakola, Kai Zhang, and Bianxiao Cui. Optically resolving individual microtubules in live axons. *Structure*, 17(11):1433–1441, 2009.

[59] Ke Xu, Guisheng Zhong, and Xiaowei Zhuang. Actin, spectrin, and associated proteins form a periodic cytoskeletal structure in axons. *Science*, 339(6118):452–456, 2013.

[60] Archan Ganguly, Yong Tang, Lina Wang, Kelsey Ladt, Jonathan Loi, Bénédicte Dargent, Christophe Leterrier, and Subhojit Roy. A dynamic formin-dependent deep f-actin network in axons. *J Cell Biol*, 210(3):401–417, 2015.

[61] Christophe Leterrier, Jean Potier, Ghislaine Caillol, Claire Debarnot, Fanny Rueda Boroni, and Bénédicte Dargent. Nanoscale architecture of the axon initial segment reveals an organized and robust scaffold. *Cell reports*, 13(12):2781–2793, 2015.

[62] Mats GL Gustafsson. Surpassing the lateral resolution limit by a factor of two using structured illumination microscopy. *Journal of microscopy*, 198(2):82–87, 2000.

[63] Rainer Heintzmann and Mats GL Gustafsson. Subdiffraction resolution in continuous samples. *Nature Photonics*, 3(7):362, 2009.

[64] Yicong Wu and Hari Shroff. Faster, sharper, and deeper: structured illumination microscopy for biological imaging. *Nature methods*, page 1, 2018.

[65] Amy M Winans, Sean R Collins, and Tobias Meyer. Waves of actin and microtubule polymerization drive microtubule-based transport and neurite growth before single axon formation. *Elife*, 5:e12387, 2016.

[66] Yue Qu, Ines Hahn, Stephen ED Webb, Simon P Pearce, and Andreas Prokop. Periodic actin structures in neuronal axons are required to maintain microtubules. *Molecular biology of the cell*, 28(2):296–308, 2017.

[67] Thomas A Klar, Stefan Jakobs, Marcus Dyba, Alexander Egner, and Stefan W Hell. Fluorescence microscopy with diffraction resolution barrier broken by stimulated emission. *Proceedings of the National Academy of Sciences*, 97(15):8206–8210, 2000.

[68] Gražvydas Lukinavičius, Luc Reymond, Elisa D'este, Anastasiya Masharina, Fabian Göttfert, Haisen Ta, Angelika Güther, Mathias Fournier, Stefano

Rizzo, Herbert Waldmann, et al. Fluorogenic probes for live-cell imaging of the cytoskeleton. *Nature methods*, 11(7):731, 2014.

[69] Elisa D'Este, Dirk Kamin, Fabian Göttfert, Ahmed El-Hady, and Stefan W Hell. Sted nanoscopy reveals the ubiquity of subcortical cytoskeleton periodicity in living neurons. *Cell reports*, 10(8):1246–1251, 2015.

[70] Anaël Chazeau, Eugene A Katrukha, Casper C Hoogenraad, and Lukas C Kapitein. Studying neuronal microtubule organization and microtubule-associated proteins using single molecule localization microscopy. In *Methods in cell biology*, volume 131, pages 127–149. Elsevier, 2016.

[71] Zhang, Y., T. Huang, D. M. Jorgens, A. Nickerson, L.-J. Lin, J. Pelz, J. W. Gray, C. S. López, and X. Nan, 2017. Quantitating morphological changes in biological samples during scanning electron microscopy sample preparation with correlative super-resolution microscopy. *PloS one* 12:e0176839.

[72] Sven C Sidenstein, Elisa D'Este, Marvin J Böhm, Johann G Danzl, Vladimir N Belov, and Stefan W Hell. Multicolour multilevel sted nanoscopy of actin/spectrin organization at synapses. *Scientific reports*, 6:26725, 2016.

[73] Raymond B Wuerker and Joel B Kirkpatrick. Neuronal microtubules, neurofilaments, and microfilaments. In *International review of cytology*, volume 33, pages 45–75. Elsevier, 1972.

[74] Nobutaka Hirokawa. Cross-linker system between neurofilaments, microtubules and membranous organelles in frog axons revealed by the quick-freeze, deep-etching method. *The Journal of cell biology*, 94(1):129–142, 1982.

[75] Bl J Schnapp and TS Reese. Cytoplasmic structure in rapid-frozen axons. *The Journal of Cell Biology*, 94(3):667–669, 1982.

[76] Loic Hamon, Patrick A Curmi, and David Pastré. High-resolution imaging of microtubules and cytoskeleton structures by atomic force microscopy. In *Methods in cell biology*, volume 95, pages 157–174. Elsevier, 2010.

[77] Toshio Ando. Molecular machines directly observed by high-speed atomic force microscopy. *FEBS letters*, 587(8):997–1007, 2013.

[78] Allan F Bower. *Applied mechanics of solids*. CRC press, 2009.

[79] Bahaa E A Saleh and Malvin Carl Teich. *Fundamentals of photonics*. John Wiley & Sons, 2019.

[80] N Streibl. Three-dimensional imaging by a microscope. *JOSA A*, 2(2), 121-127, 1985.

[81] C. N. H. Candia and B. Gutiérrez-Medina. Direct imaging of phase objects enables conventional deconvolution in bright field light microscopy. *PloS one*, 9(2), e89106, 2014.

[82] R. Hoebe, C. Van Oven, T. Gadella Jr, P. Dhonukshe, C. Van Noorden, and E. Manders. Controlled light-exposure microscopy reduces photobleaching and phototoxicity in fluorescence live-cell imaging. *Nature biotechnology* **25**, 249 (2007).

[83] U. Agero, C. H. Monken, C. Ropert,R. T. Gazzinelli, and O. N. Mesquita. Cell surface fluctuations studied with defocusing microscopy. *Physical Review E*, 67(5), 051904, 2003.

[84] B. Gutiérrez-Medina and S. M. Block. Visualizing individual microtubules by bright field microscopy. *American Journal of Physics*, 78(11), 1152-1159, 2010.

[85] A. Goriely, M. Robertson-Tessi, M. Tabor, and R. Vandiver. "Elastic growth models." In *Mathematical modelling of biosystems*, pp. 1-44. Springer, Berlin, Heidelberg, 2008.

Part II

Experimental set-up and procedures

Chapter 5

Rewiring Neuronal Circuits: A New Method for Fast Neurite Extension and Functional Neuronal Connection

M. H. Magdesian, M. Anthonisen, G. M. Lopez-Ayon, X. Y. Chua, M. Rigby, P. Grütter *Rewiring Neuronal Circuits: A New Method for Fast Neurite Extension and Functional Neuronal Connection*, JoVE (Journal of Visualized Experiments) 124 (2017): e55697.

Addendum for thesis

This chapter is written in the form of a recipe with step-by-step instructions on the experimental methods used in this thesis. In addition to this step-by-step description, a video of the detailed procedures was shot by a professional team and is also part of the multimedia JoVE article (`https://www.jove.com/video/55697/rewiring-neuronal-circuits-new-method-for-fast-neurite-extension?status=a57703k`). It is a comprehensive guide, detailing all laboratory procedures including the preparation of cells, solutions and micromanipulation tools. This chapter introduces the set-up and describes how to initiate, elongate and reconnect a neurite from a parent axon or dendrite using microbeads and micropipettes. This procedure is used again in Ch. 6 where we perform this experiment many times to get statistics.

Note that there are elements of this chapter that are beyond the scope of the rest of the thesis. In particular, this chapter focuses on plating neurons in microfluidic systems to control the location of neurons on the coverslip. These systems are not used consistently in the remainder of this thesis. However, the use of microfluidics here enables the demonstration of signal propagation between two isolated neuron populations that are connected by a mechanically-created and reconnected neurite. We do not explore the signal propagation capacities of pulled neurites in the rest of this thesis but the demonstration here constitutes compelling evidence that these pulled neurites are dendrite-like in their behaviour. This makes the results in the rest of the thesis relevant to questions of axon growth.

Abstract

Brain and spinal cord injury may lead to permanent disability and death because it is still not possible to regenerate neurons over long distances and accurately reconnect them with an appropriate target. Here a procedure is described to rapidly initiate, elongate, and precisely connect new functional neuronal circuits over long distances. The extension rates achieved reach over 1.2 mm/h, 30-60 times faster than the in vivo rates of the fastest growing axons from the peripheral nervous system (0.02 to 0.04 mm/h)

5.1 Introduction

Injuries to the adult Central Nervous System (CNS) may lead to permanent disability due to multiple mechanisms that limit axonal regrowth [5]. Following injury, many CNS axons do not form a new growth cone and fail to mount an effective regenerative response [3]. Furthermore, damage and scar tissue surrounding CNS lesions significantly inhibit axonal growth [1,3,5]. Current therapies to promote CNS regeneration after injury have focused on enhancing the intrinsic growth potential of the injured neuron and on masking the inhibitors of axonal extension associated with myelin debris and the glial scar [3,5]. Despite this, the capacity to regenerate long axons to distant targets and to form appropriate functional synapses remains severely limited [8,9,15,17].

In the present work, microbeads, pipette micromanipulation, and microfluidic devices are used to rapidly initiate, elongate, and precisely connect new functional neuronal circuits over long distances. Previous work has shown that poly-D-lysine-coated beads (PDL-beads) induce membrane adhesion followed by the clustering of synaptic vesicle complexes and the formation of functional presynaptic boutons [16]. It was also shown that when the PDL bead is mechanically pulled away after presynaptic differentiation, the synaptic protein cluster follows the bead, initiating a new neurite [24]. The following procedure exploits this fact along with the ability to culture embryonic hippocampal neurons of rats into organized regions on a coverslip using polydimethylsiloxane (PDMS) microfluidic devices to precisely rewire a neuronal circuit.

These PDMS microfluidic devices are non-toxic, optically transparent and consist of two chambers connected by a system of microchannels. Once assembled on a coverslip, each device serves as a mold to guide neuronal growth and maintain healthy neuronal cultures on precise patterns for longer than 4 weeks *in vitro*.

Here, a framework is presented in which to investigate the limits of extension and functionality of the new neurite. New, functional neurites are created and positioned to controllably (re)wire neuronal networks. The extension rates achieved are faster than 20 μm/min over millimeter-scale distances and functional connections are established. Our results show, unexpectedly, that the intrinsic capacity of these neurites for elongation is much faster than previously thought. Our proposed mechanical approach bypasses slow chemical strategies and enables controlled connection to a specific target. This technique opens new avenues for the *in vitro* study of novel therapies to restore neuronal connectivity after injury.

It also enables the manipulation and rewiring of neuronal networks to investigate fundamental aspects of neuronal signal processing and neuronal function *in vitro*.

5.2 Experimental protocols

The following is a step-by-step guide for lab procedures.

All procedures detailed below were approved by McGill University's Animal Care Committee and conformed to the guidelines of the Canadian Council of Animal Care.

5.2.1 Biological sample preparation

Standardization of neuronal cultures using microfluidic devices: device assembly

1. Select a suitable microfluidic device for the desired experiment. To connect neurons within the same population use the Neuro Devices (Fig. 5.1) and to connect neurons in different populations use the Co-Culture devices (Fig. 5.6) (ANANDA, Montreal, Canada).

2. Clean and prepare the desired number of sterile coverslips or glass bottom dishes. For best results on plastic surfaces use 35 mm dishes, on glass use 25 mm coverslips, or 35 mm glass bottom dishes.

3. Coat the dishes or coverslips with 0.5-1 mL of 100 μg/mL Poly-D-Lysine (PDL) for 2 hs or overnight at room temperature. Note: protocol can be paused here and resumed the following day if desired.

4. Wash the dishes twice with water (do not use Phosphate-buffered saline (PBS), salt crystals may block the channels), remove all the liquid and let it dry in a sterile environment such as a biosafety cabinet for 5-10 minutes or until the surface is completely dry. Note: careful to ensure the coverslips are absolutely dry, as any remaining liquid will interfere with the adherence of the microfluidic systems.

5. Place microfluidic devices with pattern facing up under UV light in a sterile environment (biosafety cabinet) for 10 mins.

6. Using tweezers place a microfluidic device with pattern facing down in contact with the clean coverslip/dish. Use the tweezers to softly press the device so that it adheres to the glass. Note: You will see the transparency of the adhered region when looking against the light. Make sure all corners are contacting the glass. Do this to all microfluidic devices. See Fig. 5.1(a).

7. To fill the single population device with medium, point the pipette towards the channels and add 50 μL of complete Neurobasal cell medium supplemented with serum-free B-27 (volume ratio 1:50) and 500 μg/mL penicillin/streptomyocin/glutamine (collectively called NBM) to the right upper well, then add another 50 μL to the well lying diagonally to it. Do this for all devices, making sure that the medium flows between wells. Next, add 50 μL of medium to the remaining 2 wells. See Fig. 5.2(a).

8. To fill the multiple population device with medium, point the pipette towards the channels and add 30 μl of complete NBM to the right wells, refer to Fig. 5.6(a). Do this for all devices, making sure that the medium flows between wells. Next, add 50 μL of medium to the remaining 4 wells.

9. Place the devices in a bigger plate with an open dish with autoclaved water (wet chamber) and place in the incubator (37°C, 5% CO_2 and 95% humidity)for 1-2 hs while you prepare the cell culture. See Fig. 5.2(b).

Plating neurons in microfluidic systems

1. Following the protocol outlined in Ref. [16] obtain dissociated hippocampal or cortical neurons from Sprague Dawely rat embryos (either gender).

2. Resuspend embryonic neurons in NBM at a concentration of 1-2 million neurons/mL. Verify cell concentrations in the microscope using a hemocytometer

and following Ref. [16]. Adjust the cell concentration according to the desired cell density. To increase the chances of obtaining single hippocampal axons per channel, plate 10000 neurons per device. To have multiple axons in the same channel, plate 60000 neurons per device. Note: These numbers vary according to the neuronal type used.

3. Remove the medium from the microfluidic devices without emptying the wells. Leave approximately 5 μL in each.

4. To plate cells in the single population device, add 50 μL of NBM to the lower right well. At this point the medium should flow by itself to fill the other lower well. Add 20 μL of the concentrate cell solution into the top right well of the microfluidic device, as indicated in Fig. 5.1(b).

5. To plate cells in the multiple population device add 20 μL of the concentrate cell solution into each of the right wells in Fig. 5.6(a).

6. Check in the microscope if cells are inside the chambers and place the devices in the incubator for 15-30 min to promote cell attachment to the substrate.

7. Check in the microscope if there are enough cells in the chambers. If more are needed, repeat steps 3-5.

8. Add 50 μL of NBM to the 2 top wells of the single population device and 20 μL of NBM into the same well as the cells were injected in the multiple population device. The media should protrude slightly to form a positive meniscus giving the wells a “muffin top” aspect. Again, see Fig. 5.2(a).

9. Maintain the cells at 37°C and 5% CO_2.

Maintaining the neuronal cultures

1. Remove NBM from the cells and apply new pre-warmed NBM the day following their introduction to the devices (that is one day after the previous step).

2. Check every two days if there is enough medium in each channel, if the “muffin top is low” just add more medium to the top wells.

3. Culture cells for at least 7 d before removal of the microfluidic devices. The cells can survive in these devices for several weeks. Remove the devices 1-2 days before experiments are performed on samples.

Removal of microfluidic devices

1. 1-2 days before removal of microfluidic devices, add 2 mL of NBM pre-warmed to 37°C to each sample dish, flooding the chambers and maintain the devices in the incubator.

2. Use sterile tweezers and one tip to remove the microfluidic devices from the coverslips leaving a patterned configuration of neurons. Use the tip to hold the coverslip in place and the tweezers to clasp the edge of the device at the bottom left corner of the well. Delicately apply torsion, raising the device up with the tweezers so that it peels off the coverslip. See Fig. 5.2(c-d).

3. Every 2-3 days replace half the NBM until the sample is used for experiments.

4. Before performing rewiring experiments on the sample, verify that neurites in the single population device channels and the neuronal populations in the multiple population device are isolated by examining the gaps between them in the microscope to ensure there are no filaments linking neuronal populations.

5.2.2 Micromanipulation set-up

Preparing PDL-coated beads

1. Add 2×50 μL drops of either 4, 10 or 20 μm polystyrene beads diluted in water (1:500) to 1 mL of PDL (100 μg/mL). Leave for at least 2 hours at room temperature. Note protocol can be paused here and resumed the following day.

2. Centrifuge the solution at 15000× rpm for 1 min.
3. Carefully remove supernatant without disturbing the beads accumulated at bottom of container.
4. Wash the beads twice with 1 mL of sterile 10 mM HEPES pH 8.4 solution.
5. Ressuspend the PDL-coated beads in 200 mL of 10 mM HEPES pH 8.4 solution.

Preparing micropipettes

1. Prepare pipettes from glass capillary tubes (∼1.5 mm outer diameter) using a horizontal electrode puller. The outer tip of the pulled micropipette should be on the order of 2-5 μm. Before pulling, ensure the glass tubes are clean.
2. Pipettes can be fixed to glass slides for storage, ensure that the tip does not contact the surface of the slide as the tip is fragile. Store in a covered container to protect from dust.

PDL-bead adhesion to neurons

1. Add 40-60 μL of PDL-coated beads to a cell culture. Center the pipette tip over the neurons, which should be faintly visible on the coverslip, and add the beads (see Fig. 5.3).
2. Return the sample to the incubator for 1 hr to promote the formation of synaptic contacts [16, 24].
3. After the incubation, remove any un-adhered beads by gently washing the culture with pre-warmed NBM.

Prepare physiological saline solution (for room temperature experiments)

1. Prepare physiological saline solution by combining the ingredients listed in Refs. [16, 17].
2. Verify osmolarity and pH levels as indicated in Refs. [16, 17].
3. Continuously infuse solution with O_2 to minimize pH fluctuations while conducting experiments.
4. Heat to room temperature.
5. Set up the perfusion system by inserting one end of a plastic tube (optional dimensions) in O_2-infused physiological solution and fixing the other end to a needle inserted in the sample holder. Place the tubing and solution higher than the sample (See Fig. 5.4).
    (a) Disconnect the tube from the needle and connect it to a syringe. Use the syringe to exert pressure and draw liquid, filling the tube. Seal with a roller clamp and reconnect the needle.

5.2.3 Re-wiring neuronal networks

Bead Micromaniputaion

1. Install sample in an experimental set-up such that cells can be accessed from above by two micropipettes mounted in micromanipulators and accessed optically below, for instance with the 40×-phase objective with a numerical aperture of 0.6 of an inverted optical microscope. In this configuration, a CCD camera for image capture can be mounted on the side port of the microscope. Connect each pipette to 1 mL syringes via plastic tubing. At this step, replace NBM with physiological saline solution (1-2 mL) (See Fig. 5.4).
2. During experiments, continuously perfuse cells with the physiological saline solution prepared in the previous step at a rate of 0.5-1 mL/min.

3. Select a PDL-bead NOT attached to a neuron in the field of view. Align the bead with the second micropipette tip by focusing onto the bead then up to the micropipette. Bring the tip down as close as possible to the bead by monitoring it through the microscope.

4. Apply negative pressure with the 1 mL syringe connected to the pipette to pick up the bead. Maintain negative pressure throughout the experiment.

Pulling neurites

1. Select a PDL-bead attached to a neuron in the field of view and attach it to the second micropipette using suction as described in the previous step.

2. Pull the PDL-bead-neuron complex by slowly (∼0.5 μm/min) moving either the micromanipulator or the sample stage by 1 μm and pause for 5 min to allow neurite initiation.

3. Repeat item 2 twice. Note: the first 3 μm have to be pulled very slowly to guarantee experimental success.

4. Pull the PDL-bead-neuron complex by slowly moving either the micromanipulator or the sample stage by 2 μm and pause for 5 min to allow neurite elongation.

5. After successful initiation and neurite extension for the first 5 μm the neurite can now be pulled at 20 μm/min over millimeter-scale distances. Note: Pulling can be performed continuously or in steps and at varying rates. See Fig. 5.5(b-c) .

Connecting neurons

1. Select a region rich in neurites and lower the PDL-bead-neurite complex so that it physically contacts it. Use other beads to gauge tip height above coverslip surface. See Fig. 5.5(d).

2. Leave the PDL-bead-neurite complex in contact with the target neurite while manipulating the second micropipette. Lower the second pipette with the second PDL-bead on top of the newly formed neurite about 20 μm form the first bead. Use the second PDL-bead to push the new neurite filament towards the target cell.
3. Hold both beads in place for at least 1 h. Verify the absence of focal swelling, a thickening of the neurites contacting the bead, with the microscope [18].
4. During this time, use perfusion to slowly change the medium of the sample from physiological saline to pre-warmed, CO_2-equilibrated NBM
5. Release the bead from the second pipette by releasing suction. If the new neurite remains attached, release the first bead as well. See Fig. 5.5(e).
6. Gently remove saline solution and replace with NBM ($\sim$2 mL).
7. Carefully place the sample back in the incubator to strengthen the neuronal connection for future experiments. This connection is stable for $>$ 24 h [17].

Verifying the Functionality of the New Connection via Whole-cell Paired Patch Clamp Recordings

1. Follow Refs. [7, 17, 22] to assemble an electrophysiology set-up.
2. Follow Ref. [17] to prepare the pre- and postsynaptic electrodes.
3. Gather patch clamp data, again following Refs. [7, 22].
4. Compare the results to naturally occurring signals [17] to determine the connection type.

5.3 Summary

Embryonic rat hippocampal neurons are cultured in microfluidic devices to enable precise positioning of cells, PDL-beads and micromanipulators. The first step is

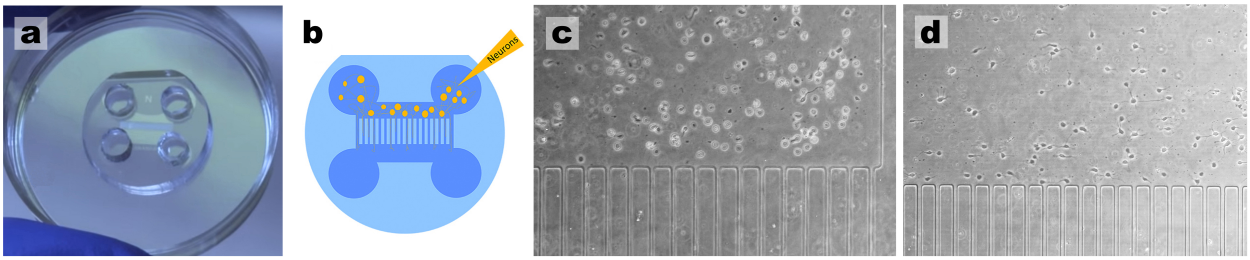

Figure 5.1 Standardization of neuronal cultures using microfluidic devices. **(a)** Device assembly: when the microfluidic devices are properly assembled on a dry surface all chambers are visible. **(b)** Cell plating: plate the cells on the top right well and cells should move towards the left well. **(c)** Cell density: just after plating, check in the microscope if the concentration of cells is adequate. **(d)** After one day in culture, hippocampal neurons are well adhered close to the microchannels and start forming neurites.

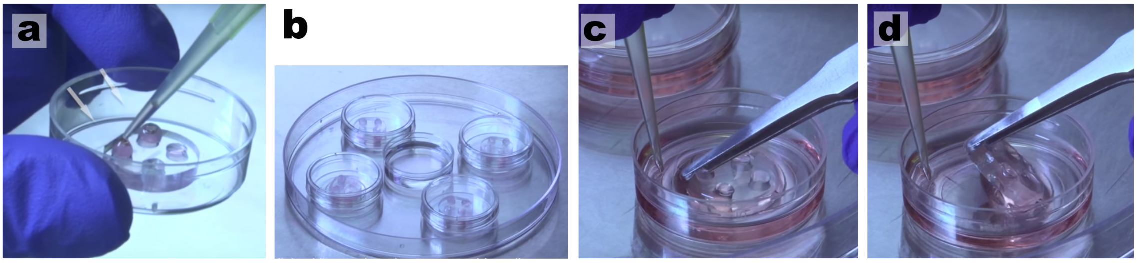

Figure 5.2 Maintenance of healthy neuronal cultures for several weeks. **(a)** Add medium every 2-3 days and keep a positive meniscus in the upper wells of the microfluidic chambers so cells will have a constant supply of nutrients. **(b)** Keep cells inside a larger plate with a dish containing water to reduce medium evaporation. **(c)** Use sterile tip and tweezers to **(d)** easily peel off the microdevices.

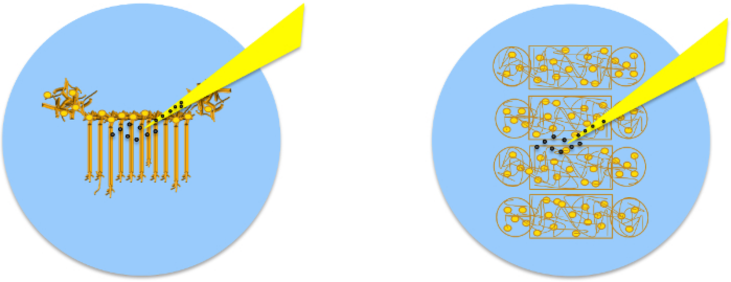

Figure 5.3 Location of Pipette Depositing Beads into Cultures.Once the microfluidic device has been removed, neurons are visible on the coverslip. When depositing beads, position the pipette tip so that it is in the center of the cells.

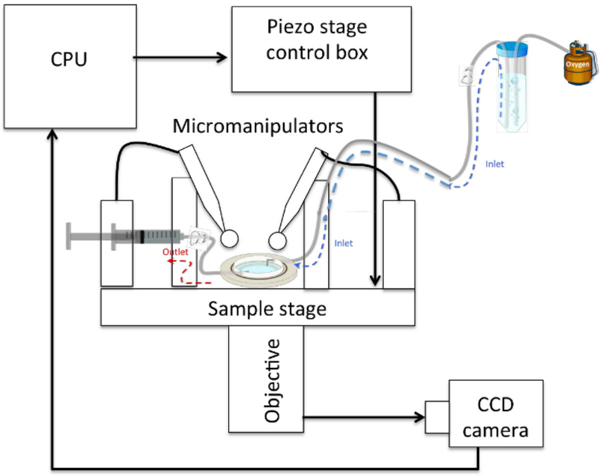

Figure 5.4 Schematic of a Typical Neurite-pulling Set-up. The sample rests on a (piezo-actuated) stage and can be accessed from above by 2 micropipettes held in micromanipulators and connected to 1 mL syringes via plastic tubing. The sample is accessed optically from below by an objective connected to a CCD camera that sends images to a CPU. An inlet tube feeds oxygenated physiological saline solution to the sample, which rests below it, and an outlet tube connected to a syringe allows the withdrawal of solution in the event of overflow.

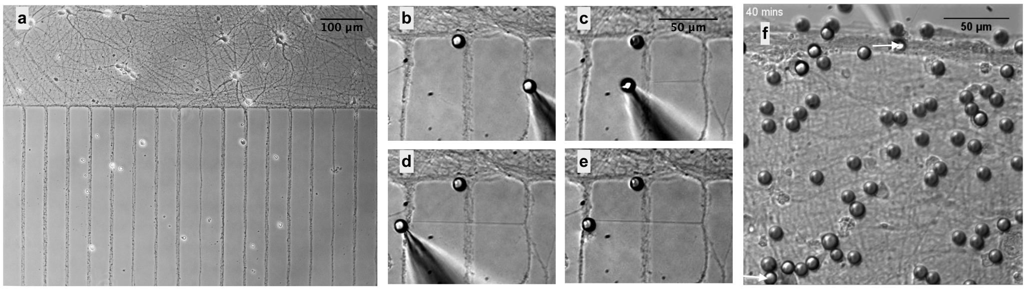

Figure 5.5 PDL-bead Adhesion to Neurons and Pipette Micromanipulation (Magdesian *et al.*, 2016). **(a)** Neurons remain organized in patterns after removal of microfluidic chambers allowing easy identification of soma and neurites. **(b)** Micromanipulation of PDL-beads adhered to neurites enables neurite initiation, extension **(c)** and connection **(d)**, followed by release of the PDL-bead from the pipette **(e)**. **(f)** After contacting two isolated neuronal populations (bottom arrow), a second PDL-bead and pipette micromanipulator (top arrow) is used to establish a second adhesion point, a few hundreds of microns apart form the first contact point, and guarantee functional connections.

to properly assemble the microfluidic device on a glass coverslip or dish. It is essential that the microfluidic device be well attached to the substrate to avoid cells exiting the chambers and moving under the parts of the device that should be sealed (Fig. 5.1(a)). To maintain healthy cultures for several weeks, it is important to prevent medium evaporation by checking the cell medium every 2-3 days and preserving a positive meniscus of medium (Fig. 5.2(a)). Medium evaporation is also avoided by keeping both the cells and an open dish of water inside a larger plate (Fig. 5.2(b)). The microfluidic devices can be removed at any time. For optimal results, NBM should be added to the cell-device system at least one day before device removal. This minimizes cellular stress as the neurons are in contact with medium at ideal temperature and pH when the devices are removed. When the microfluidic devices are slowly peeled off the dish (Fig. 5.2(c) and (d)) cells will remain in the patterned position (Fig. 5.3 and Fig. 5.5(a)).

Two types of microfluidic devices are used: Neuro Device and Co-Culture Device. The first enables easy identification of axons, dendrites and cell bodies.

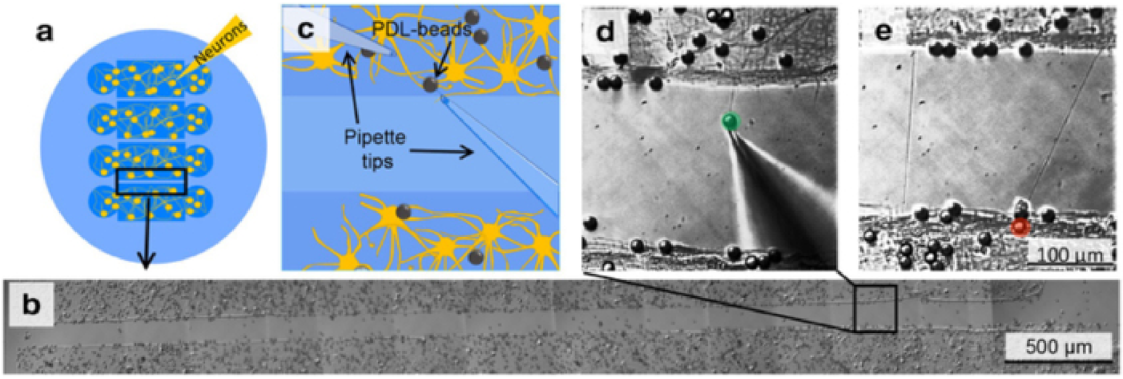

Figure 5.6 Initiation, Elongation and Connection of New Neurites to Connect two Isolated Populations using Multiple Population Device and Micromanipulation (Magdesian *et al.*, 2016). **(a)** The device isolates 4 neuronal populations between 3 gaps of 100 or 200 μm each. **(b)** Following removal of the device, select one gap and certify that no neurites connect the 2 individual populations. **(c)** Schematic of the experimental set-up as should be visible in the optical microscope, indicates the position of two micropipettes and the presence of PDL-coated beads. **(d)** By applying negative pressure to a pipette, a PDL-bead adhered to one neuronal population is pulled with the pipette tip, thereby initiating a new neurite. By maintaining the negative pressure in the pipette, the PDL-bead-neurite complex (green) can be pulled, elongating the neurite. **(e)** Pipette micromanipulation guides extension of the new neurite over the gap and the formation of a connection with a new neuronal population. To ensure the adhesion of the new neurite to the second population, a PDL-bead (red) is positioned with a second pipette on top of both the extended neurite and neuronal population.

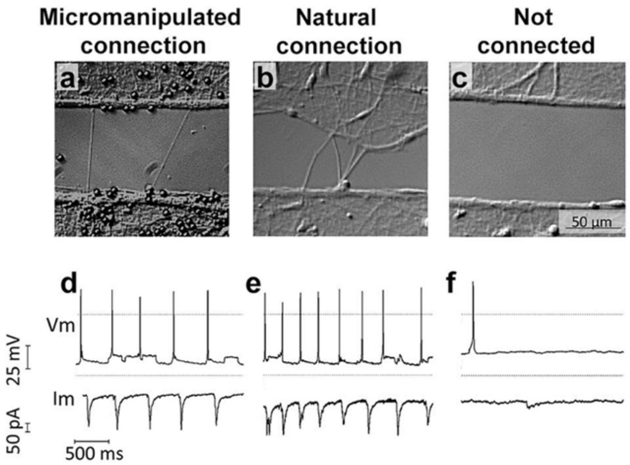

Figure 5.7 The Newly Induced, Elongated and Connected Neurite can Transfer Information Between two Isolated Neuronal Populations (Magdesian *et al.*, 2016). Isolated neuronal populations were cultured separated by a 100 μm gap in PDMS microdevices. Paired patch clamp recordings were performed in whole cell configuration from a neuron in population one and a neuron in population two (on the other side of the gap) when the two populations were connected through mechanical manipulation **(a)**, allowed to naturally interconnect across the gap, **(b)** or remain non-connected by maintaining the gap **(c)**. Representative traces of paired recordings are shown for each condition **(d-f)**.

The soma remain in the top soma chamber while axons and dendrites grow along the microfluidic channels (Fig. 5.5(a)) towards the axonal chamber.

It is recommended that PDL-beads be added to cells at a ratio of 10:1 and that most beads that have not adhered to the culture be removed by washing the cells once with NBM following the 1 h incubation (Fig. 5.3). Following PDL-bead adhesion to neurites, the PDL-bead-neurite complex is pulled and can be extended over large distances. The newly formed neurite can be precisely connected to neurites or soma millimeters away (Fig. 5.5(b)-(e)). The success rate for pulling a new neurite for the first 3 μm at speeds lower than 1 μm /min is $> 95\%$ ($n = 206$). The success rate for connecting the new neurite to another cell is 70% ($n = 30$). The connection is very fragile in the first 18 h, mainly because the new neurite is a filament of less than 1 μm in diameter anchored by a 10 μm PDL-bead. If the dish is rapidly moved during the first minutes of contact, the resulting turbulence of the medium may cause the bead to roll and consequently the adhesion to be lost. However, if the sample is not shaken, in 30 min the bead attaches to the neurites on the dish and the new connection remains for at least 48 h. See Fig. 5.4 for a schematic of the set-up.

The PDL-bead position on the culture can also be used to easily identify the location of the connected neurite (Fig. 5.6(d)-(e)). After initiation, extension and connection of a new neurite, a second, non-adherent PDL-bead, picked up via the micromanipulator, is used to create a second adhesion site between the initiated neurite and the second neuronal population. The second PDL-bead is placed on top of the new neurite, compressing it such that the new neurite just contacts the second neuronal population [18]. This will promote adhesion with the second neuronal population (Fig. 5.5(f)).

The multiple population device enables the growth of 4 isolated neuronal populations on the same dish. Each neuronal population is confined to a 4×7 mm rectangle separated from other neuronal populations by 100 or 200 μm gaps (Fig. 5.6(a)). Healthy neurons can grow inside the devices for several weeks. Usually, the neuronal populations remain isolated up to 48 h after removal of the device. After this 48 h period, neurons tend to grow towards neighboring neuronal populations and form natural connections. Before connecting two isolated populations, it should be verified that the populations are indeed truly isolated by examining the entire gap with the microscope to establish that there is no link between the two neuronal populations (Fig. 5.6(b)).

After connection, samples were incubated for 24 h and electrical whole cell paired patch clamp recordings were conducted to investigate whether the newly formed neurite used to connect two isolated neuronal populations was functional and able to transmit electrical signals. A neuron in population one, located less than 100 μm radius from the site where the induced neurite was initiated, was selected to record presynaptic action potentials (PAPs). This neuron was considered the presynaptic cell. Postsynaptic excitatory or inhibitory activity was recorded from a neuron in population two, on the other side of the gap, located in less than 100 μm radius of the micromanipulated connection (Fig. 5.7(a)-(c)). Recordings derived from the mechanically-induced connections were analyzed and compared to those from naturally connected neuronal populations and non-connected populations (Fig. 5.7). The electrical responses after PAP recorded from neurons connected naturally and by micromanipulation are significantly higher and temporally correlate with the presynaptic activity (Fig. 5.7).

5.4 Conclusion

Using standard micromanipulation and innovative microfluidic devices, a new technique was developed to rapidly initiate, elongate and precisely connect new functional neuronal circuits over large distances. Pipette micromanipulation is a common tool in most neuroscience labs [4, 15]. The real challenge to achieving reproducible and reliable results was standardization of healthy, precisely positioned neuronal cultures for the duration of the experiment (which can be on the order of weeks) through the development of microfluidic devices to organize cell cultures with micrometer precision. High quality cell cultures are the cornerstone of data validation. This contributes to easier and faster microscopy imaging and standardization of cultures and results. The microfluidic devices were designed to culture cells in vitro with similar organization as in vivo. The single population device enables the growth of long neurites and easy identification of axons, neurites and soma. The number of cells plated in the microfluidic chambers determines the neuronal density. Therefore, by plating fewer cells per device it is easy to identify single neurons close to the channels. The axon and multiple dendrites of one single neuron grow inside one channel. Dendrites grow at least 5 times slower than axons [8, 21] and after 2-3 weeks *in vitro* their growth in the channels is usually limited to 200 μm while fast-growing axons can reach beyond 2 mm [21]. Therefore, after adding PDL-beads to the samples, it is relatively easy to estimate whether the beads are adhering mostly to axons or to axons and dendrites (Fig. 5.5(b)-(f)). There are higher chances of pulling new axons and dendrites when pulling the PDL-beads attached to neurites shorter than 200 μm, while there are greater odds of pulling only new axons when pulling PDL-beads attached to neurites longer than 500 μm. The multiple population device is useful for the reproducible growth of healthy separated populations for several weeks. This system of channels is useful for studying up to 4 different cell types or comparing the same cells with different treatments.

Moreover, a controlled and reproducible cell culture environment provides an ideal framework for cell analysis and manipulation. Precise positioning of cells on a dish facilitates identification of regions of interest as well as orientation and navigation through these areas of interest ultimately allowing unprecedented control over the neurite initiation site. A controlled cell distribution makes it easier to visualize the newly formed connection and much faster to find the new connection with the microscope in the days following incubation. In addition, reproducible configurations of cells enable easy and precise positioning of chemical cues, such as the PDL-coated beads, on the soma, dendrites or axons [16]. Taken together, imaging and analysis of cells grown in microfluidic devices are faster due to standard cellular organization reproduced in all dishes. Furthermore, the devices are made of biocompatible, transparent and removable material, enabling imaging at all visible wavelengths and cell survival inside the devices for several weeks. Miniaturization of cellular assays also helps gather more data with fewer cells.

The low-volume consumption of the microfluidic devices reduces the number of cells needed per experiment and increases experimental efficacy. For instance, instead of spending several hours searching with a microscope for perhaps 1 or 2 isolated axons in a dish, the single population device can be used to immediately access over 100 isolated axons per cell sample. The microfluidic devices offer a miniaturized reliable and controlled cell culture environment favoring the analysis of rare samples with time to perform multiple tests.

Potential variations of the technique involve the direct attachment of the bead to the micropipette. In the current protocol, a method is described for attaching the bead to the tip via suction, but the bead can also be glued to the tip. Glue is the better option if a highly stable connection between the tip and the bead is desirable, for example if force measurements are made using the pipette as a sensor or if investigation of adhesion between PDL and the neurite is the main experimental objective. In another vein, suction is advantageous as it allows the release of the bead after placement without severing the neurite-bead complex thus enabling several connections to be made in parallel. Suction provides means for high throughput rewiring experiments, an improvement over other manipulation techniques such as atomic force microscopy (AFM) [17, 24]. Both modifications of this method allow the neurite initiation site to be selected by simply maintaining a bead in contact with a dendrite so synapses are formed. However, the strategy of incubating several beads as described in step 7 saves time at the manipulation stage and is recommended if precise control over the initiation site is unnecessary in the experiment.

Future research could seek to address various instrumental limitations, namely temperature control and sample accessibility. Mechanical properties of the cellular membrane can significantly vary at different temperatures [20]. Ideally all experiments should be performed at 37°C in neuronal medium and adequate conditions (correct CO_2 pressure and humidity controls). However it was not possible to use a closed cell incubator, because access to the samples from the top is required for the micromanipulators, from the bottom for the microscope and from the side to move the stage. Therefore perfusion at room temperature was used. In a similar vein, since the set-up only has enough space to accommodate 2 micromanipulators and it takes almost 1 h to establish a single connection, there is a limit to the number of experiments one can perform. This issue could be addressed with a manipulator that pulls more than one bead at a time. Another potential improvement to this protocol is the capability to register the height of the bead-pipette complex from the sample surface. The inability to do this can lead to imprecisions when bringing down the second bead and placing it on the induced neurite to fix it. The bead is lowered on top of the new neurite in a neurite-rich region until the new neurite and those on the dish lie in the same focal plane. The new neurite is never between the bead and the dish, but always between a cushion of cell matter and the bead, therefore the compression is reduced.In addition, the new neurite is observed for 10 min in the microscope to evaluate if neurite focal swellings are formed near bead. As described in Ref. [18], the presence of swellings indicates neurite degeneration. Nevertheless, since applying varying amounts of pressure to axons can lead to physiological changes [18], future research could focus on adapting the pipette-probes by fixing reflectors to them and monitoring displacement perpendicular to the sample surface with AFM methods. Finally, perhaps the greatest challenge to this protocol is to test the functionality of the manipulated connection. The most direct, reliable and well established technique is paired whole-cell patch clamp recordings. However, the success rate of regular paired patch clamp recording is very low ($< 25\%$) [7]. Whole-cell patch clamp has several disadvantages including long set up time, limited number of experiments/day, limited recording time ($\sim$30 min), low experimental yield for paired patch clamp recordings and cell death after measurements. Due to these technical challenges the experimental yield of whole-cell patch clamp paired recordings after micromanipulation is very low. Better platforms and techniques are needed to more precisely stimulate, record and compare neuronal activity in natural and micromanipulated connections.

The importance of tension in axonal growth has been known since the early days of neuroanatomy—referring to it as passive stretching [11]. During early embryonic development neurites migrate through small distances to reach their targets. As most cells divide and duplicate, axons are subjected to continuous forces to elongate and adjust their length to embryonic growth [11, 26]. Several groups have tried to test the limits of neurite growth by applying chemical cues and/or mechanical tension to neurons (for review see Ref. [10]). In these reports [4, 12–14] as well as during physiological growth, the neurites are pulled while attached to a substrate. The major difference to our setup is that in the present technique the new neurites only have two adhesion contacts; at the base the neurite is attached to the neuron and at the tip the neurite is attached to the bead. During elongation the components of the new neurite have the freedom to disperse in the most efficient way to accommodate the pulling forces. More importantly, this protocol describes how to reproduce these experiments without causing neurite rupture nor degeneration, based on previous studies on the formation of synaptic contacts [16] and on the resistance of axons to pressure [18] showing how to use micro- and nanotools to continuously pull the neurites with the appropriate force. The neurite extension rates described here (1.2 mm/h) are 30-60 times faster than the in vivo rates of the fastest growing axons from the peripheral nervous system (0.02 to 0.04 mm/h) [25]. When compared to the same neuronal type in vitro, the axonal extension rates described here are 7.5 times faster than the growth rates described by other authors at an earlier stage of development (0.1 mm/h) [15]. Different types of neurons have been found to extend axons at different intrinsic rates that vary by several fold [6]. In addition, central nervous system axons usually lose the high rate of axonal growth after target innervation in vivo [6] and 3 d of culture in vitro [8]. Therefore the current axonal extension technique should be tested with different neuronal types to better understand the limits of neurite extension.

Pipette micromanipulation and microfluidic devices are techniques demonstrated to create new functional neurites and to controllably position or (re)wire neuronal networks. This platform is ideal for systematic, standardized measurements. It introduces reproducibility and in vivo control into experiments on complex networks of neurons. The extension rates achieved are faster than 20 μm/min over millimeter-scale distances and functional connections are established. These results show, unexpectedly, that the intrinsic capacity of axons for elongation, including that of their cytoskeletal components, is much faster than previously thought [2,23]. This proposed mechanical approach bypasses slow chemical strategies and thus represents a paradigm shift for therapeutic developments to restore neuronal connectivity after injury and for micro-neuroengineering of artificial neural networks for their controlled study in vitro. These results also have a major impact on regenerative medicine and neuro-engineering approaches with direct implication for therapies that aim to reconnect neuronal circuits after trauma or in neurodegenerative diseases. This platform opens the door to obtaining data on neuron communication, signal modulation as well as growth and regeneration. It is a new way of mechanically regenerating the CNS and similar techniques may allow restoration of function after injury. Furthermore, this technique can be used to create systematically engineered neuronal networks as novel bioassay platforms for drug discovery and target validation. It is a precursor to the direct wiring of robust brain-machine interfaces.

Acknowledgements

We would like to thank Yoichi Miyahara for many helpful discussions and insights. MA and PG acknowledge funding from NSERC.

Bibliography

[1] ALBERT J Aguayo, Garth M Bray, Michael Rasminsky, Thomas Zwimpfer, David Carter, and MANUEL Vidal-Sanz. Synaptic connections made by axons regenerating in the central nervous system of adult mammals. *Journal of Experimental Biology*, 153(1):199–224, 1990.

[2] Gerard MJ Beaudoin III, Seung-Hye Lee, Dipika Singh, Yang Yuan, Yu-Gie Ng, Louis F Reichardt, and Jyothi Arikkath. Culturing pyramidal neurons from the early postnatal mouse hippocampus and cortex. *Nature protocols*, 7(9):1741, 2012.

[3] Frank Bradke, James W Fawcett, and Micha E Spira. Assembly of a new growth cone after axotomy: the precursor to axon regeneration. *Nature Reviews Neuroscience*, 13(3):183, 2012.

[4] Dennis Bray. Axonal growth in response to experimentally applied mechanical tension. *Developmental biology*, 102(2):379–389, 1984.

[5] Daniel J Chew, James W Fawcett, and Melissa R Andrews. The challenges of long-distance axon regeneration in the injured cns. In *Progress in brain research*, volume 201, pages 253–294. Elsevier, 2012.

[6] Eric YP Cho and Kwok-Fai So. Rate of regrowth of damaged retinal ganglion cell axons regenerating in peripheral nerve graft in adult hamsters. *Brain research*, 419(1-2):369–374, 1987.

[7] Dominique Debanne, Sami Boudkkazi, Emilie Campanac, Robert H Cudmore, Pierre Giraud, Laure Fronzaroli-Molinieres, Edmond Carlier, and Olivier Caillard. Paired-recordings from synaptically coupled cortical and hippocampal neurons in acute and cultured brain slices. *Nature protocols*, 3(10):1559, 2008.

[8] Carlos G Dotti, Christopher A Sullivan, and Gary A Banker. The establishment of polarity by hippocampal neurons in culture. *Journal of Neuroscience*, 8(4):1454–1468, 1988.

[9] Kimberly Goslin and Gary Banker. Experimental observations on the development of polarity by hippocampal neurons in culture. *The Journal of cell biology*, 108(4):1507–1516, 1989.

[10] Collin Gray, Mika Hukkanen, Yrjo T Konttinen, Giorgio Terenghi, Timothy R Arnett, Sheila J Jones, Geoffrey Burnstock, and Julia M Polak. Rapid neural growth: calcitonin gene-related peptide and substance p-containing nerves attain exceptional growth rates in regenerating deer antler. *Neuroscience*, 50(4):953–963, 1992.

[11] Ross Granville Harrison. The croonian lecture on the origin and development of the nervous system studied by the methods of experimental embryology. *Proceedings of the Royal Society of London. Series B-Biological Sciences*, 118(808):155–196, 1935.

[12] Steven R Heidemann and Dennis Bray. Tension-driven axon assembly: a possible mechanism. *Frontiers in cellular neuroscience*, 9:316, 2015.

[13] Steven R Heidemann and Robert E Buxbaum. Mechanical tension as a regulator of axonal development. *Neurotoxicology*, 15(1):95–107, 1994.

[14] Steven R Heidemann, Phillip Lamoureux, and RE Buxbaum. Cytomechanics of axonal development. *Cell biochemistry and biophysics*, 27(3):135–155, 1997.

[15] Phillip Lamoureux, Gordon Ruthel, Robert E Buxbaum, and Steven R Heidemann. Mechanical tension can specify axonal fate in hippocampal neurons. *The Journal of cell biology*, 159(3):499–508, 2002.

[16] Anna Lisa Lucido, Fernando Suarez Sanchez, Peter Thostrup, Adam V Kwiatkowski, Sergio Leal-Ortiz, Gopakumar Gopalakrishnan, Dalinda Liazoghli, Wiam Belkaid, R Bruce Lennox, Peter Grutter, et al. Rapid assembly of functional presynaptic boutons triggered by adhesive contacts. *Journal of Neuroscience*, 29(40):12449–12466, 2009.

[17] Margaret H Magdesian, G Monserratt Lopez-Ayon, Megumi Mori, Dominic Boudreau, Alexis Goulet-Hanssens, Ricardo Sanz, Yoichi Miyahara, Christopher J Barrett, Alyson E Fournier, Yves De Koninck, et al. Rapid mechanically controlled rewiring of neuronal circuits. *Journal of Neuroscience*, 36(3):979–987, 2016.

[18] Margaret H Magdesian, Fernando S Sanchez, Monserratt Lopez, Peter Thostrup, Nela Durisic, Wiam Belkaid, Dalinda Liazoghli, Peter Grütter, and David R Colman. Atomic force microscopy reveals important differences in axonal resistance to injury. *Biophysical journal*, 103(3):405–414, 2012.

[19] Bryan J Pfister, David P Bonislawski, Douglas H Smith, and Akiva S Cohen. Stretch-grown axons retain the ability to transmit active electrical signals. *FEBS letters*, 580(14):3525–3531, 2006.

[20] Bryan J Pfister, Akira Iwata, David F Meaney, and Douglas H Smith. Extreme stretch growth of integrated axons. *Journal of Neuroscience*, 24(36):7978–7983, 2004.

[21] F Polleux and William Snider. Initiating and growing an axon. *Cold Spring Harbor perspectives in biology*, 2(4):a001925, 2010.

[22] Guanxiao Qi, Gabriele Radnikow, and Dirk Feldmeyer. Electrophysiological and morphological characterization of neuronal microcircuits in acute brain

slices using paired patch-clamp recordings. *JoVE (Journal of Visualized Experiments)*, (95):e52358, 2015.

[23] Warren Strober. Monitoring cell growth. *Current protocols in immunology*, 21(1):A–3A, 1997.

[24] Fernando Suarez, Peter Thostrup, David Colman, and Peter Grutter. Dynamics of presynaptic protein recruitment induced by local presentation of artificial adhesive contacts. *Developmental neurobiology*, 73(1):98–106, 2013.

[25] Stephen G Waxman, Jeffery D Kocsis, Peter K Stys, et al. *The axon: structure, function, and pathophysiology.* Oxford University Press, USA, 1995.

[26] Paul Weiss. Nerve patterns: the mechanisms of nerve growth. *Growth*, 5:163–203, 1941.

Part III

Neurite Forces

Chapter 6

Response of Mechanically-Created Neurites to Extension

M. Anthonisen, M. Rigby, M. H. Sangji, X. Y. Chua and P. Grütter, *Response of Mechanically-Created Neurites to Extension*, Journal of the Mechanical Behavior of Biomedical Materials. **98**, 121 (2019).

Addendum for Thesis

This chapter extends the scope of the experimental set-up introduced in Ch. 5 by adding force-measurement capacities. We add particle-tracking techniques and stiffness-calibration measurements to precisely determine the bending of the micropipette as it pulls a neurite. We obtain the tension of the neurite as it is extended. We do this many times for 5 different pull speeds to obtain force-extension curves of neurites.

The data collected here is used in Ch. 7 to obtain the diameters of pulled neurites and these are combined with the force-extension curves obtained in this chapter to model neurite growth in Ch. 8.

Abstract

We use micromanipulation techniques and real-time particle tracking to develop an approach to study specific attributes of neuron mechanics. We use a mechanical probe composed of a hollow micropipette with its tip fixed to a functionalized bead to induce the formation of a neurite in a sample of rat hippocampal neurons. We then move the sample relative to the pipette tip, elongating the neurite while simultaneously measuring its tension by optically tracking the deflection of the beaded tip. By calibrating the spring constant of the pipette, we can convert this deflection to a force. We use this technique to obtain uniaxial strain measurements of induced neurites and investigate the dependence of the force-extension relationship on mechanical pull speed. We show that in the range of pull speeds studied (0.05-1.8 μm/s), the variation in the work to extend a neurite 10 μm is consistent across pull speeds. We do not observe statistically significant rate-dependent effects in the force-extension profiles; instead we find the same quadratic behaviour (with parameters drawn from the same distributions) at each pull speed.

6.1 Introduction

Tension is a fundamental driver of neurite growth and development [5,31]. This has been demonstrated by a series of experiments in which mechanical tension, applied with microneedles, is used to initiate and elongate axons (see e.g. [6,7,12,24,29,31]). In all types of axons investigated (embryonic chick sensory [44], rat hippocampal [24], and rat ganglion [37]) elongation rate was found to depend linearly on tension applied. This is evidence of a connection between tension and the axonal assembly process [5, 31]. The surprisingly rapid addition of new cellular material during neurite elongation as well as the exact mechanisms and the limits by which tension influences this mass accretion present many open questions [5, 16] such as whether the stimulus governing mechanotransduction is force or deformation.

We present a methodology based on micromanipulation tools and particle-tracking techniques to measure neurite mechanics. In [27] it is shown that when polystyrene beads coated with positively-charged poly-D-lysine (PDL) contact axons or dendrites, presynaptic structures form, which adhere to the bead. If this bead is then pulled, the growth of an auxiliary structure, the neurite, is induced. In [29], micropipettes, suction and PDL-coated beads were combined to exploit the advantages of each as micromanipulation tools to create *de novo* functional neurites. These neurites contained cytoskeleton elements and could transmit electrical signals. Here, we extend the work in [29] by performing force measurements on individual neurites as they are being pulled. This is achieved by fabricating mechanically compliant micropipettes, suitably calibrating their spring constants and applying particle-tracking techniques to determine force-elongation relationships of neurites being pulled. This gives us qualitative and quantitative information on the relationship between elongation and the force involved which can ultimately be used to extract material parameters for neurites and to model neurite growth. The controlled release of neurite-tethered beads, rendered possible by suction, opens the door to complex neuronal re-wiring experiments [29, 34]. This is an advantage over other techniques used to quantify forces in axons and dendrites, such as those that employ just microneedles or atomic force microscopy (AFM) [4, 14, 15, 22].

In the following, we measure force-extension relationships for a range of extension rates. Previous work done with the same method at rates of ~ 0.025 μm/s [29] and ~ 0.5 μm/s [38] reports the formation of neurites containing the same proteins as axons (including actin and tubulin). However, these papers made no attempt at quantifying the force-extension relationship involved. In this paper, we explore this relation in the regime between these two bounds. We pull at speeds up to 1.8 μm/s; to our knowledge this is 18 times faster than the fastest speeds ever reported in axon pulling experiments [33] and over 300 times faster than the fastest *in vivo* growth rates for axons of the same type [13, 41]. Surprisingly, we do not observe rate-dependent behaviour over a 10-fold increase in speed. We observe the variation in the fit parameters describing the force extension profiles to be the same across all pull speeds investigated.

6.2 Materials and methods

6.2.1 Experimental set-up

The apparatus contains five main elements, which are described below. Throughout the description, we refer to Figure 6.1a, which shows a schematic representation of the apparatus that features only the main components. These components are:

1. The neuron: Rat hippocampal neurons are cultured on coverslips and mounted in a fluid cell.

2. Movable platform: The fluid cell is fixed to a movable platform. The platform is a computer-controlled piezo stage constrained to move in two dimensions with a 90 μm$\times$90 μm range.

3. A pipette: A pipette is held in a fixed location; it is prepared so that one of its ends is tapered. The tapered end is flexible; this flexibility is important, as it will be used to measure the force exerted by the neurite. Suction is applied through the pipette by means of a syringe attached to the back-end of the pipette. The suction is used to hold a microbead firmly to the tapered end. This allows the controlled release of beads, demonstrated in Fig. 6.1c, which is an advantage compared to AFM.

4. A microbead: Microbeads coated with PDL are randomly distributed in the medium in which the neurons grow. When a microbead makes contact with a neuron, the PDL coating stimulates the formation of a synapse and thus a stable mechanical contact [38]. This connection is sufficiently strong as to withstand all manipulations imposed upon it during the experiment.

5. A microscope/camera: An inverted optical microscope (Olympus 71-X equipped with a 40× objective, NA=0.6), and a CCD camera (Cascade II, Photometrics) are used to acquire optical microscope images at rates of 1 Hz and 5.5 Hz.

To initiate and elongate a neurite, a bead-tipped pipette contacts a neuron for 30 minutes so a synapse can form (see Fig. 6.1b, 6.1d) [27,29]. Most of the data presented in the Results and Discussion section is obtained with beads fixed to the pipette tips with glue instead of with suction. This is to avoid potential errors in the displacement measurements due to small movements of the bead relative to the pipette tip as tension is applied. The sample stage is moved relative to the beaded pipette tip, thus applying a force on the neuron; the result is the mechanical creation and elongation of a new neurite. The mechanism allows the neurite to be pulled over large distances ($> 80\ \mu$m) at very high rates (we report pull speeds up to 1.8 μm/s).

In our experiments, we use a Sutter Pipette Puller (Flaming/Brown, model P-87) to fabricate pipettes with spring constants ~ 0.001 N/m and track the beaded tip with a resolution of ~ 20 nm. This provides a force measurement with resolution ~ 0.02 nN.

6.2.2 Bead tracking

As the neurite is pulled, we acquire microscope images and optically track the positions of all the beads in these images with a custom-made centroid-tracking algorithm [9]. We track beads fixed to the sample surface, termed “reference beads", to obtain the distance the platform has been moved ($d_1(t)$ in Fig. 6.1b). We also track the bead at the pipette tip to obtain the deflection of the pipette (this is $d_2(t)$ in Fig. 6.1b). The value of $d_1(t) - d_2(t)$ corresponds to the length the neurite is extended at time $t > t_0$, where t_0 is the time the platform is set in motion.

To characterize the stability and noise of our system, we measure the displacements over time of reference beads without moving the sample stage. Typical profiles of these displacements are shown in Fig. 6.2a, while Fig. 6.2b shows normal distributions that are fitted to these displacements. We find the displacement of an individual bead has a stable and constant mean for extended periods of time with a standard deviation of ~ 20 nm, dominated by bead-tracking error.

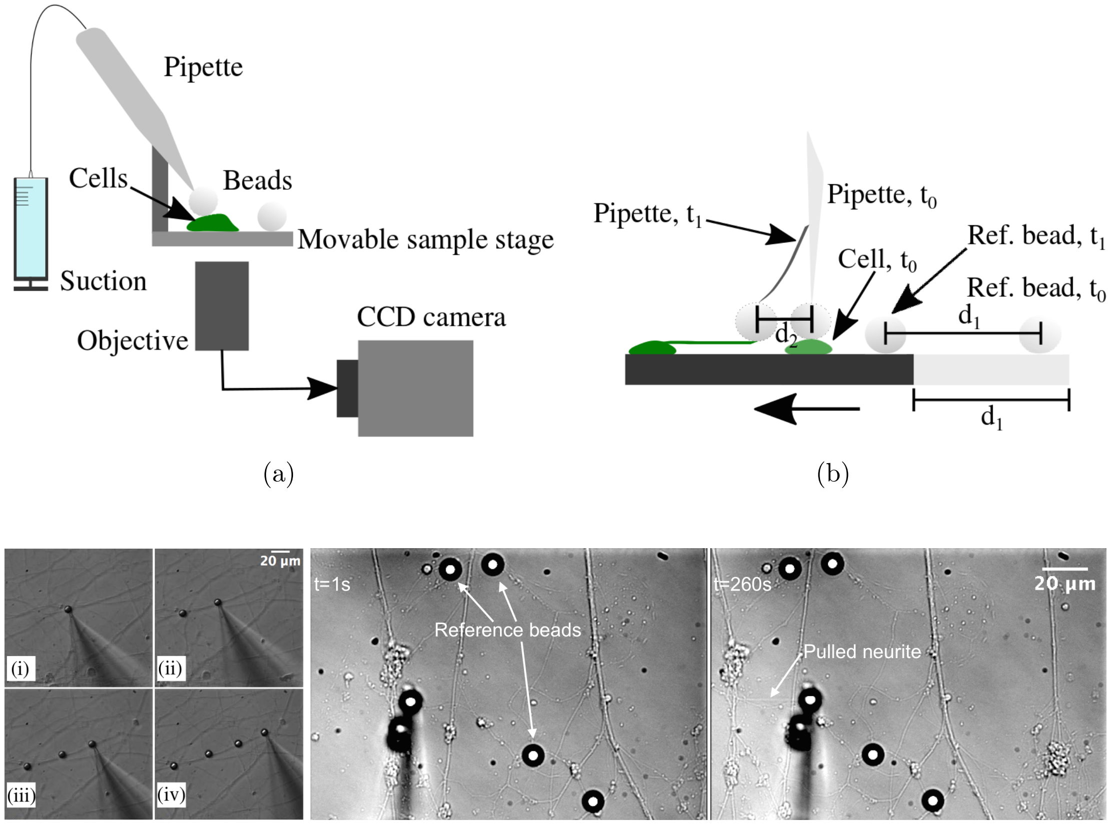

(a) (b)

(c) (d)

Figure 6.1 **(a)** Schematic of set-up for the initiation, elongation and detection of tension of neurites. The sample cells are mounted on a piezo-actuated nano positioning stage that is controlled by a CPU. A micropipette held in a micromanipulator approaches the sample from above the stage. The back of the pipette is connected to a 1 ml syringe via plastic tubing which allows for the controlled pick-up and release of beads. The sample is contacted optically from below by the 40× objective of an inverted optical microscope connected to a CCD camera which captures 512×512 pixel images. **(b)** Schematic of a pull (side view). At t_1, the stage has been moved to the left by d_1. The pipette bends by an amount d_2. The length the neurite has been pulled at t_1 is $d_1 - d_2$. **(c)** Demonstration of the capacity to control the adhesion sites of functionalized beads using suction. **(d)** Initiation and elongation of a neurite with a 10 μm PDL-coated bead and pipette micromanipulations. Snapshots depicting a neurite being pulled (arrow) by keeping the micropipette and the bead stationary and moving the stage (left in this instance). Reference beads are also indicated (arrows). Images are acquired at a rate of 1 Hz.

Averaging the displacements of several beads in the same image series reduces this error to $\sim$ 10 nm. In the following, we take the error in bead displacement, δd_i, to be 20 nm. The accuracy of the tracking algorithm was investigated by using computer-generated data that simulated measurements of bead locations, and then comparing the measurements produced by the tracking mechanism with the known “locations" in the data. The error was approximately 4 percent of a pixel, which is 16 nm. Other work has shown the variance of the lateral motion estimation is proportional to the square of the sampling width and inversely proportional to the average signal-to-noise ratio [2,3,43]. Therefore, subnanometer bead motion could be measured by reducing the sampling width (e.g. with higher magnification and a camera with smaller pixels) and by increasing the signal-to-noise ratio by increasing the illumination intensity. Note that neurons are photo-sensitive so optical power should be minimized. However, as we will show, our tracking sensitivity is more than adequate to observe neuron mechanics.

To ensure an accurate interpretation of biological measurements, several “null” experiments are performed by moving the sample stage (without neurons) and tracking the tip-bead, Fig. 6.2c-d. This allows us to determine the force-noise in our measurements due to mechanical vibrations coupling to the instrument. The distribution of the displacement of the tip-bead has a standard deviation of $\sim$65 nm.

6.2.3 Probe preparation and calibration

Flexible micropipettes with tip outer diameters of 0.5 to 2 μm were manufactured by locally heating the centers of glass capillary tubes (1.5 mm outer diameter, King Precision Glass Inc) and rapidly pulling the two ends apart in a Sutter Pipette Puller (Flaming/Brown, model P-87). Both pull speed and temperature influence pipette geometry, and these are chosen so as to obtain flexible micropipettes with long tapers ($\sim$5 mm, see Fig. 6.3a) [36]. We calibrate the pipette stiffness with standard AFM measurements following the procedure outlined in [19,36], wherein the spring constant is obtained by comparison to a reference probe of known

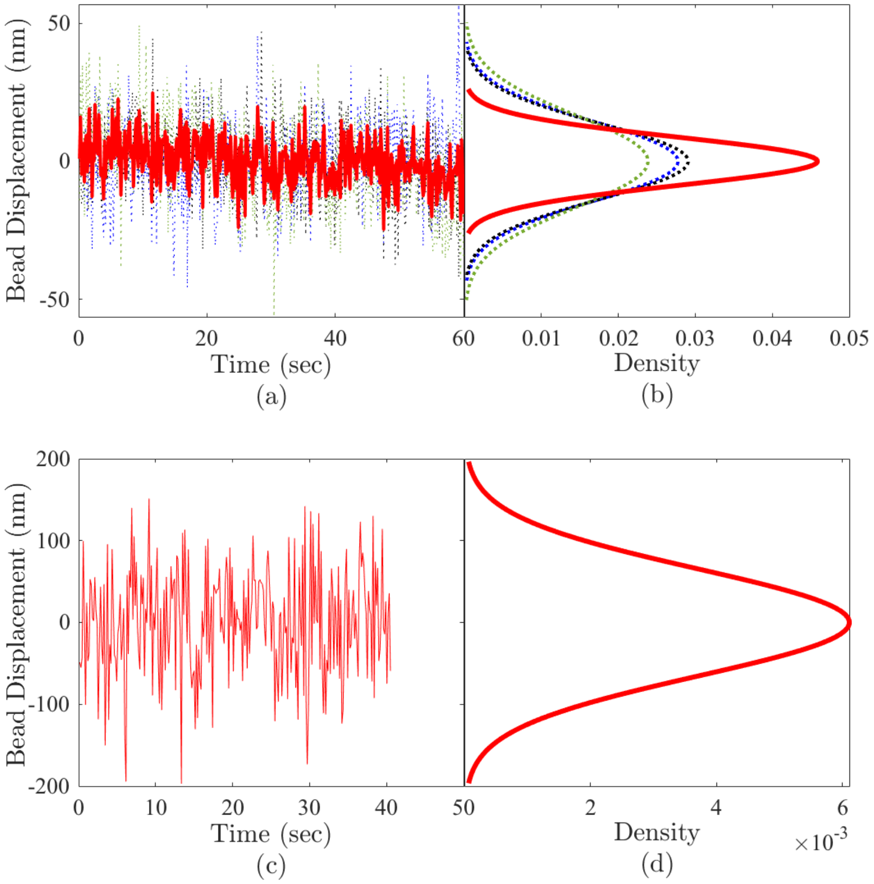

Figure 6.2 **(a-b)** Tracking of beads fixed to the fluid cell surface with the stage kept stationary. Dashed lines are individual bead displacements and the average of the individual time series is in red. **(a)** The displacement of beads versus time, images acquired at a 5.5 Hz rate. **(b)** Normal distributions of displacements. The distribution of the average of the individual time series in **(a)** has a standard deviation of ∼10 nm. **(c-d)** Tracking of a bead fixed to the tip of a pipette with stiffness 0.001 N/m. The pipette was held stationary while the sample stage was moved (a null experiment). **(c)** The displacement of the tip-bead versus time. **(d)** The distribution of displacement has a standard deviation of ∼65 nm.

stiffness. Using the MFP-3D-BIO AFM (Asylum Instruments), we calibrated a commercial AFM cantilever (HQ:CSC38, μmasch) according to the thermal noise method [20]. This "reference" cantilever was then used to collect force-distance curves at the pipette tip (see Fig. 6.3). For each pipette, several force-distance curves were acquired and the mean and standard deviation of probe stiffness were computed. Spring constants of pipettes used to measure force-extension curves range from $(1.0 \pm 0.1) \times 10^{-3}$ to $(1.6 \pm 0.2) \times 10^{-2}$ N/m. Note that increasing the opening of the pipette tip (e.g. by pulling at a slower rate and/or at a lower temperature) leads to a stiffer probe that applies suction to beads more easily. We find pipettes with stiffnesses $\sim$0.01-0.02 N/m can easily manipulate beads (see Fig. 6.1c) while maintaining the flexibility necessary to observe forces in neurites. Typically, commercially available cantilevers designated for biological experiments have minimal spring constants of 0.01 N/m whereas micropipettes can be made an order of magnitude more compliant.

6.2.4 Neuronal cultures

All procedures were approved by McGill University's Animal Care Committee and conformed to the guidelines of the Canadian Council of Animal Care. Following the procedures outlined in [27, 28] and references therein, hippocampal neurons from Sprague Dawley rat embryos (either sex) were isolated and placed on 25 mm glass coverslips (Warner Instruments) coated with 100 μg/ml PDL (Sigma-Aldrich). Samples were immersed in Neurobasal Medium (Life Technologies) supplemented with serum-free B-27 (volume ratio 1:50) and penicillin/streptomycin/glutamine (volume ratio 1:10) and maintained in the incubator (37°C, 5 %CO_2) for 7-21 days before measurements. Experiments were performed at room temperature and cells were continuously perfused with oxygen-infused physiological saline solution [consisting of 135 mM NaCl (Sigma-Aldrich), 3.5 mM KCl (Sigma-Aldrich), 2 mM $CaCl_2$ (Sigma-Aldrich), 1.3 mM $MgCl_2$ (BDH), 10 mM HEPES (ThermoFisher Scientific), 20 mM D-glucose (Invitrogen) [28]. To regulate the cell environment, pH was maintained between 7.3-7.4 and osmolarity between 240-260 mOsm. Data

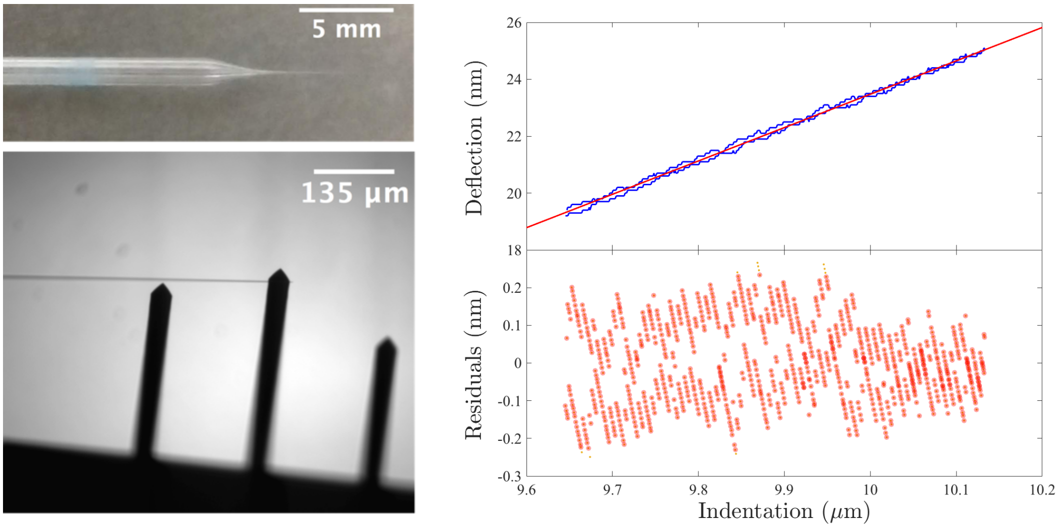

(a) (b)

Figure 6.3 Calibration of a micropipette with a reference cantilever. **(a)** Top: Micropipette with a long taper. Bottom: Image of an AFM cantilever, spring constant of 0.0483 N/m, contacting a micropipette. **(b)** Upper graph is the linear region of a force-distance curve acquired on a micropipette. The two blue lines are the indentation and retraction curves. The inverse slope of the linear fit (red line) is used to obtain the micropipette stiffness. The fit residuals are plotted below.

presented in this work is from 19 dishes, each with a cell density of $\sim 10^6$ neurons/mL.

6.2.5 Immunocytochemistry and properties of pulled neurites

Evidence that the pulled structures created with beads are in fact neurites makes this work relevant to questions of axonal growth. In this subsection, we address the question “are we pulling neurites?" by performing fluorescent microscopy to identify two cytoskeleton elements, actin and microtubules, in newly-created neurites. We also discuss references that give further evidence that our structures are axon-like.

Fig. 6.4a shows actin present in an extension pulled at a speed of 0.5 μm/s from an axon bundle expressing actin-GFP. The live-cell fluorogenic F-actin labeling probe (100 nM) was added to 2 mL of the physiological saline solution and incubated for 6 hours after which the medium containing the probe was replaced with new physiological saline.

In Fig. 6.4b, microtubule growth is captured with a fluorescently-tagged end-binding (EB) protein, End-Binding Protein 3-Green Fluorescent Protein (EB3-GFP). EB proteins are a type of Microtubule Associated Protein that bind to the ends of microtubules so when fluorescently tagged, they are markers of microtubule growth. In Fig. 6.4b, variations in intensity along the neurite show microtubules growing towards the distal end of the neurite ~ 824 seconds after its creation, the earliest time fluorescent recordings were acquired. Cell lines expressing fluorescently-labelled EB3 were prepared by viral transfection. Lentiviruses were a gift from the Fournier lab [21]. Neurons were infected overnight with purified lentivirus at a multiplicity of infection (MOI) of 2-3.

Fluorescence microscopy was performed using a Zeiss Axiovert 200M microscope and a 63× objective (Zeiss), with the fluorescent probes illuminated by a Xenon arc bulb (Sutter Instruments).

In previous works [35, 38], extensions were induced from axons expressing two other fluorescent proteins, one at a time: synaptophysin-GFP and bassoon-GFP, as well as from axons where the dye Tubulin Tracker$^{\text{TM}}$ Green (Invitrogen) was used to fluorescently label tubulin. In all cases, newly-created extensions (pulled at speeds > 0.5 μm/s) were observed to fluoresce, indicating these proteins are also present in the extensions.

We note that while it is uncertain that the proteins present are structured in a functional way at the timescales considered in this work, [29] showed that neurites induced by PDL-coated beads are electrically functional 24 hours after creation. As in [29], we allow the bead to contact the neuron for 30 minutes prior to pulling, long enough for a synapse to be induced. This increases the probability that we are pulling a neurite-like structure versus membrane tethers, which are cylindrical lipid structures that dynamically form on the cell membrane within seconds of being contacted by an adhesive bead [11, 17]. The identifiable components of an axon are present in our extensions suggesting these have similar mechanical properties and will develop into functional neurites.

6.3 Results and Discussion

6.3.1 Uniaxial strain measurements

In the following, we apply our force-sensing pipette technique to investigate the mechanics of extending neurons. The details of the procedure to initiate and pull a neurite are described in [28]. The flexible pipette method allows us to investigate the force-extension relationship of neurites over distances of 0-10 μm. Fig. 6.5 shows the force-extension relationships for pulls at 5 different extension rates, 5 to 300 times greater than the *in vivo* rates of the fastest growing neurons (0.006 um/s to 0.01 um/s [13,41]). Inspection of Fig. 6.5 shows that the spread of neurite deformability is largely uniform across the regime of pull speeds considered. Error bars are from combining the error in pipette stiffness and the error in the displacement of the beaded tip with the error formula for products. Fig. 6.5c, curves $\mathrm{C}-\mathrm{VI}$ and $\mathrm{C}-\mathrm{VII}$ were measured with beads fixed to pipette tips using suction; in the other cases the beads were glued to the tips. An interesting question

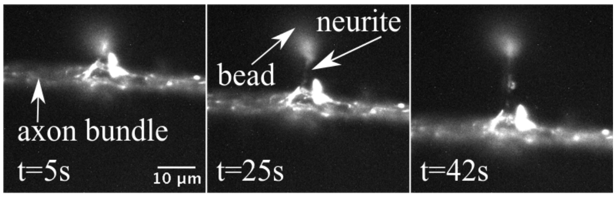

(a)

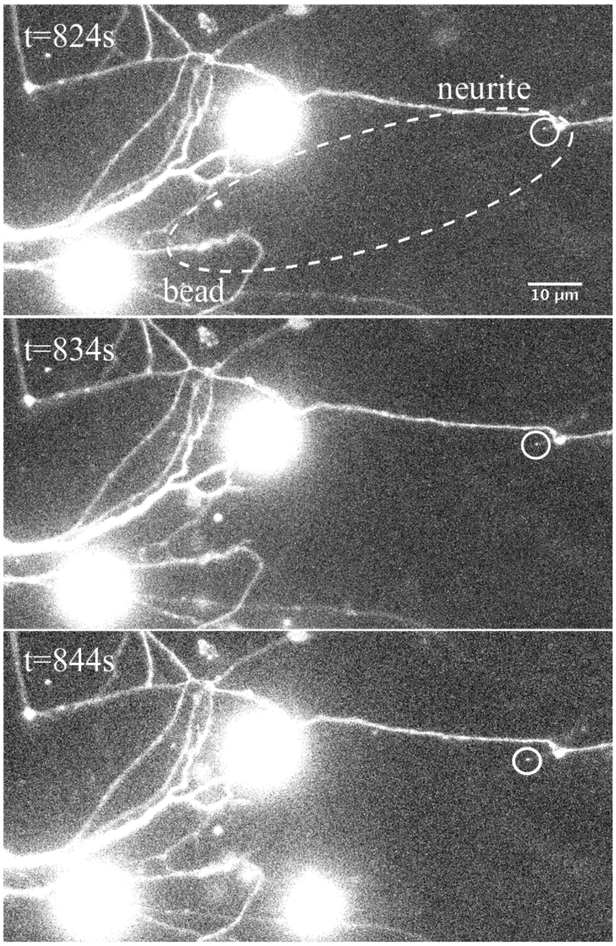

(b)

Figure 6.4 Cytoskeleton elements in newly-created neurites. **(a)** A neurite pulled from an axon bundle expressing actin-GFP (at a speed of ~ 0.5 μm/s) is observed to fluoresce. From one still image to the next the stage has been moved down relative to the stationary bead. **(b)** Microtubule growth marked by fluorescent EB3-GFP (white circles) in a newly-created neurite (pulled for ~ 87 μm at an average rate of 0.2 μm/s).

is if all the curves are similar. By eye it seems that some curves are monotonic (for example Fig. 6.5a, curve A − X), whereas others have discontinuities (for example Fig. 6.5a, curve B − VII). We use a statistically robust approach to address this question in two steps. First, we test whether our data can support a dependence of the force-extension relationship on pull rate, and second, we categorize curves by type (monotonic or non-monotonic) and by the number of parameters needed to fit their functional dependence.

To determine if the pulling rate matters we compute the integral of each curve (i.e. the work to extend a neurite) and compare sets (grouped by pull speed) with the Kruskal-Wallis test. We use the Kruskal-Wallis test because it does not require samples to follow a normal distribution. This test reveals no significant statistical difference between sets, the scatter in each set is consistent for all pull speeds. These results are summarized in Fig. 6.6.

In Fig. 6.6, we also show the age of the neurites (days *in vitro*), grouped by pull speed and classification type (discussed below). Age and work to extend a neurite have a correlation coefficient of ∼0.05, which indicates age is not an important factor affecting deformability.

Next, we determine if there are different classes of force-extension curves. We fit each curve with a family of polynomials with degrees ranging from 1 to 4 using a weighted least squares routine in Matlab (Mathworks). Weights are $w_i = 1/\delta f_i^2$ where δf_i is the measurement error on a data point. For each polynomial fit, a chi-square goodness-of-fit test was performed on the residuals to determine whether or not they followed a normal distribution (as would be the case if only noise remained in the signal after fitting). Curves were then categorized according to the smallest degree polynomial of the fit that returned residuals following a normal distribution. Force-extension relations that can be described by a polynomial of degree 1 or 2 are classified as “type I” curves, shown in blue in Fig. 6.5. Cases requiring a higher order polynomial to eliminate structure in the residuals were further treated and classified according to the Chow test [10]. The Chow test rejects the null hypothesis that the data can be fit with a single set of regression coefficients. These cases were treated as follows. First the data was divided into

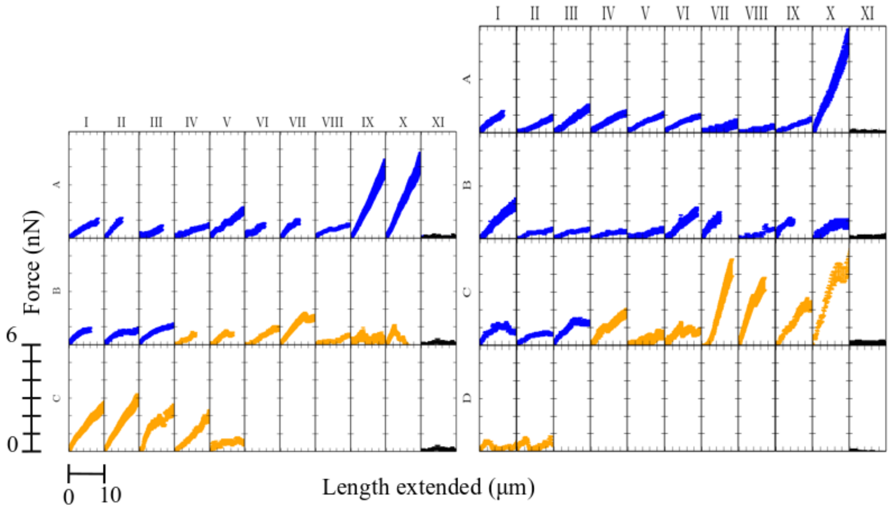

(a) v=0.05 µm/s

(b) v=0.1 µm/s

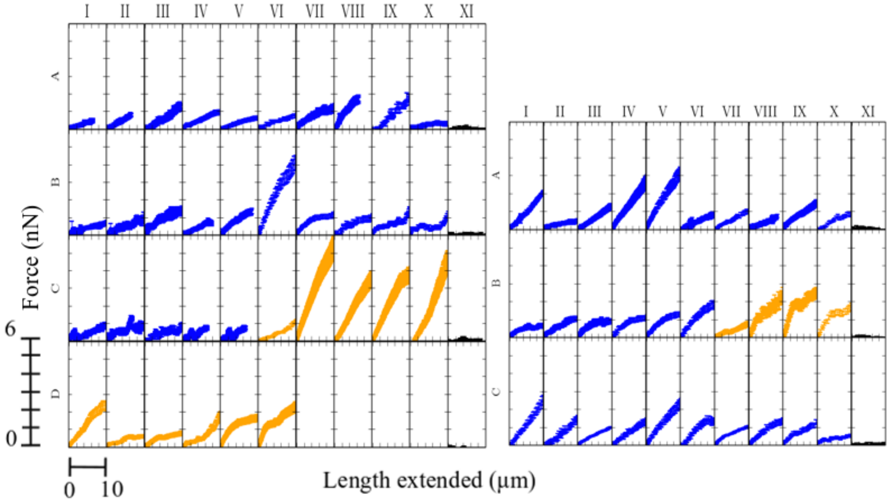

(c) v=0.2 µm/s

(d) A-B: v=0.5 µm/s, C: v=1.8 µm/s

Figure 6.5 Responses of rat hippocampal neurites to mechanical forces applied under different elongation rates. Each curve corresponds to a single pull inducing one or more neurites. Curves were obtained for pull speeds of 0.05 μm/s **(a)**, 0.1 μm/s **(b)**, 0.2 μm/s **(c)**, 0.5 μm/s **(d)**, rows A and B, and 1.8 μm/s **(d)**, row C. “Type I” curves are in blue, “type II" curves are in gold and null experiments (occupying the last columns of a-d) are in black. Calculation of error bars as described in text.

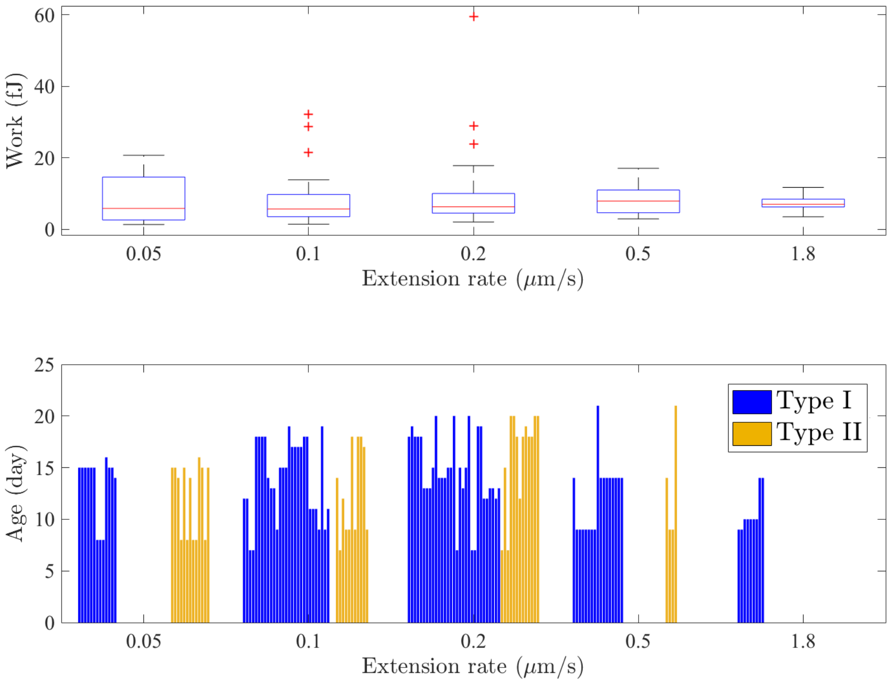

Figure 6.6 Top: Box plot summarizing the data displayed in Fig. 6.5. For every curve in Fig. 6.5, a value of work was computed by summing the product of extension and corresponding force. These values are plotted here. For each box, the central line corresponds to the median work value with the top and bottom edges of the box indicating the 75th and 25th percentiles of the data respectively. The whiskers encompass the most extreme data points except for the outliers which are indicated by the red crosses. Comparisons of the groups show no statistical significance ($p>0.1$) according to the Kruskal-Wallis test. Bottom: Bar graph of the ages of cell cultures; bars are grouped according to extension rate and classification type. This shows age is not an important factor affecting deformability.

subsets separated by break-points. A break-point could correspond to a single point defined by a spike in the residuals of the 2^{nd} degree fit or it could be created by excluding a subset of data such as a bump or anomalously noisy region. The Chow test was then applied to the remaining data. In some cases, by excluding a subset of the data, a degree 1 or 2 polynomial could be fit to the remaining data (for example Fig. 6.5b, curve $\mathrm{B}-\mathrm{VI}$, Fig. 6.5c, curves $\mathrm{C}-\mathrm{I}$ to $\mathrm{C}-\mathrm{V}$). These curves are classified as type I. In the remaining cases, the Chow test rejects the null hypothesis indicating the data is better fit with two different sets of regression coefficients. These are classified as "type II", shown in gold in Fig. 6.5. Applying the Chow test in this way lets us differentiate between curves with quadratic behaviour (expect for possibly a stand-alone spike) and curves requiring a more complex model to describe behaviour with kinks or discontinuities.

Fit parameters for the 2^{nd} degree fits are shown in Fig. 6.7. For the coefficients of the quadratic model fit to each curve, the t-statistics and corresponding p-values were computed using a built-in Matlab routine. These statistics test the null hypothesis that a given coefficient is zero against the alternative hypothesis that it is nonzero. Less than 10 % of curves had a quadratic coefficient with a t-statistic with a p-value < 0.05. The linear fit parameters for type I curves (all speeds) are distributed about a mean of 0.17 nN/μm with a SD of 0.12 nN/μm. According to the Mann-Whitney U-test (MWU), this is a different distribution than that describing the linear parameters of type II curves, which has a mean of 0.28 nN/μm and a SD of 0.22 nN/μm. On the other hand, the MWU test shows that the the quadratic parameters of type I and type II curves (all speeds) are drawn from the same distribution; we find the quadratic term to be -0.006±0.011 nN/$\mu\mathrm{m}^2$ for type I and -0.005±0.022 nN/$\mu\mathrm{m}^2$ for type II. Despite the large SD of the distribution, the quadratic term is statistically relevant. We discuss possible mechanisms for type I versus type II behaviour at the end of this section.

The same type I and type II behaviour emerges at different pull speeds (Fig. 6.7b-f). Surprisingly, we find the fit parameters to have the same scatter across all speeds investigated, as confirmed by the Kruskal-Wallis test. We observe the same behaviour with a 10-fold increase of extension rate. Thus rate-dependent mechanical effects (such as viscoelasticity) or active forces (due to a biologically 'active material' response) are small and statistically not detectable at these timescales.

The work to extend a neurite by 10 μm is 8.6±8.3 fJ (mean±SD) (Fig. 6.6). This result is consistent with previous studies; [24] find a value of 4 fJ to initially extend a single hippocampal neurite by 10 μm. However, we do not observe a positive linear relationship between extension rate and work to deform a neurite as reported for rat hippocampal neurons [24], the axons of embryonic chick sensory neurons [44], and the axons of rat ganglion neurons [37]. Our smallest elongation rate, 0.05 μm/s, is almost twice the largest extension rate reported for hippocampal neurites in towing experiments; put differently, we pull for much shorter timescales to achieve the same extension. We explore a different range of pull speeds and we find the behaviour of neurites under tension in this range is not modeled by a damping element (a Newtonian dashpot), unlike the behaviour of neurites at lower pull speeds [30]. We speculate that this is because at fast rates biologically 'active' forces are not relevant or measurable. Our measurements would thus be characteristic of the 'intrinsic' material properties. Indications of this are the observed cytoskeleton dynamics, which lag behind the mechanical pulling of neurites [34]. We also performed pulls at 37°C. While this dataset is too small to be statistically significant, we note that values of stiffness constants obtained are within the lower bounds of the data in Fig. 6.7. This suggests temperature is not the dominant factor influencing the behaviour of the force-extension relations of neurites on timescales measured. We conclude this section with a list of possible reasons for type I versus type II behaviour.

1. Axon versus dendrite: In our experiments, we do not know the nature of the pulled neurites (dendritic or axonal). It follows that type I versus type II behaviour could depend on the structure of the neurite. AFM experiments have shown stiffness of hippocampal axons to be larger than stiffness of dendrites under compression so it is reasonable that axonal and dendritic neurites respond differently to deformations under strain [42].

2. Multiple induced neurites: We sometimes observe that when a single bead

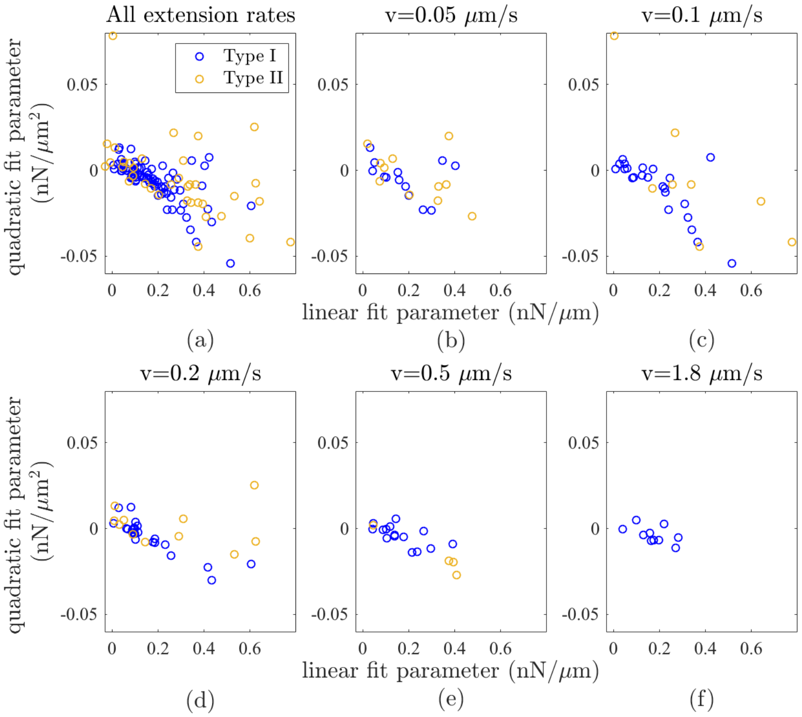

Figure 6.7 Fit parameters for 2nd degree fits of type I (blue) and type II (gold) curves. **(a)** Quadratic fit parameter versus linear fit parameter for all pull speeds. The mean±SD for type I linear parameters is 0.17 ± 0.12 nN/μm and that of the the quadratic parameter is -0.006 ± 0.011 nN/μm^2. For type II curves the linear fit parameter is 0.28 nN/μm±0.22 nN/μm and the quadratic fit parameter is -0.005±0.022 nN/μm^2. **(b-f)** Quadratic fit parameter versus linear fit parameter for each extension rate. We note the behaviour of the curves does not change, even with a 10-fold increase in the extension rate. The Kruskall-Wallis test is used to determine that the linear parameters at each pull speed are drawn from the same distribution, as are the quadratic fit parameters.

is pulled away from a denditric structure, multiple neurites can be induced. Distinguishing the exact number of neurites is challenging due to the fact that their radii are often below the diffraction limit of our optical microscope. It is possible that one or more of these neurites could break off the bead during the pull leaving a discontinuity in the force-profile as in Fig. 6.8a&c. Experiments reported in [29] point to bead-size as a factor influencing the number of neurites created and is an interesting avenue of future study.

3. Motion of submicron particles: Other possible reasons for type I versus type II behaviour are linked to the causes of bumps or spikes in the force-extension curves. In some cases, these jumps can be correlated to biological phenomena visible in the associated image series. For example, Fig. 6.5d, curves $A - X$, $C - VI$, $C - VIII$, have spikes associated with the motion of submicron particles along the neurite. An example is illustrated in Fig. 6.8b. These particles are likely organelles being transported along the neurite [8,18,38] or membrane defects [25]. Our method quantifies these processes as variations in the force-extension profile (Fig. 6.8a).

4. Motion of neurite perpendicular to direction of pull: Bumps also occur in conjunction with the motion of neurites themselves in directions perpendicular to the motion of the beaded pipette tip, see Fig. 6.5b, curve $A - II$. [38] observed that after it had been stretched, a neurite would displace its initial point of contact along the axon, minimizing its length.

6.4 Conclusion

In this paper we have studied the mechanics of newly induced neurites; to our knowledge this is the only large-scale investigation of structures originating from parent axons or dendrites. We find that on timescales and distances probed, neurite extension is well described by a quadratic model with a stiffness constant of $1.7 \times 10^{-4} \pm 1.2 \times 10^{-4}$ N/m and a quadratic term of -6±11 N/m^2. The variation

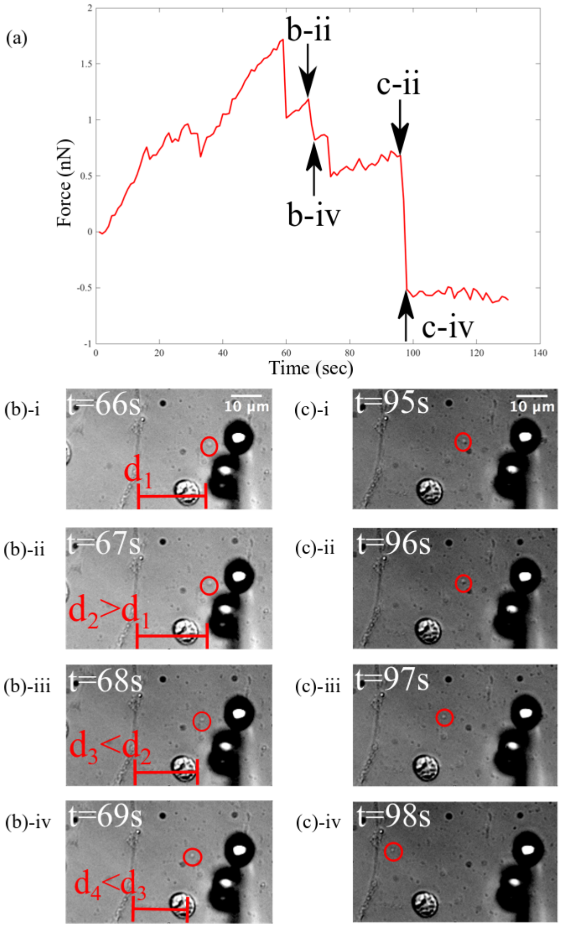

Figure 6.8 Example of submicron particle-movement along a neurite corresponding to spikes in the force-profile. **(a)** Graph of force on the pipette-tip versus time; features that correspond to visible events in the image series are indicated with arrows. **(b)** Images at times corresponding to a bump in the force-time curve. From $t = 66$ s to $t = 67$ s, the distance between the submicron particle (red circles) and the neurite-initiation site increases (distances indicated with red scale bars). From $t = 67$ s to $t = 68$ s and again from $t = 68$ s to $t = 69$ s, the distance between the submicron particle and the neurite-initiation site decreases, even as the neurite-initiation site is pulled away from the bead. This decrease corresponds to a drop in force (b-ii-b-iv). **(c)** Images at times corresponding to the large drop in the force-time curve (c-i-c-iii). The neurite appears to break off the bead. This can be seen by the same submicron particle (circles) that jumps to the neurite-initiation site from $t = 96$ s to $t = 98$ s.

of this data within a given pull speed is the same across all pull speeds, even with more than a 10-fold increase in speeds. For initial extensions of 10 μm we do not observe the linear relationship between work and pull speed previously reported for axons [24, 37, 44]. Finally, using statistically robust methods, we distinguish two types of behaviour characterized by either quadratic (type I) or discontinuous/non-monotonic (type II) force-extension relations, the latter being observed with a much lower frequency. In most cases, the continuous parts of the force-extension relationships of the type II curves have type I characteristics. Interestingly, the neurite-initiation site along the axis of the parent axon or dendrite did not influence our ability to initiate a neurite. This points to a uniformity in the branching potential of axons/dendrites.

To perform these studies, we have developed a multi-purpose system that combines flexible pipettes, functionalized beads and particle-tracking capabilities to enable robust, reproducible force measurements on individual cells. We show our system encompasses all the benefits of the traditional force sensing techniques with the added potential for more elaborate and/or higher-throughput experiments if the option of suction is used to attach beads to the pipette tip. The ability to release the beads means that multiple experiments can be performed. In our set-up, the pulled neurite is suspended in medium and does not contact the substrate unlike other, slower, methods of elongating axons that rely on chemical cues from a suitably compliant substrate, see e.g. [5, 23]. In these instances, as well as in works that use a combination of chemical and mechanical cues to explore the limits of neurite growth, cells are pulled along a substrate so the adhesion of the cell to the substrate can obscure the explicit roll of tension in the growth process [7, 16]. In fact, it is an open question how substrate stiffness affects axonal growth, electrophysiological and cytoskeleton function [4, 5]. Tension applied to axons adhered to a deformable substrate leads to a disruption in the microtubule network [39] whereas tension applied to axons suspended in media (though at less extreme rates) leads to a normal cytoskeleton array and axons able to transmit active electrical signals [16, 32, 33].

Future applications of the force probe could be to perform the same experiments described here on cell cultures treated with different cytoskeleton inhibitors to isolate the role of each cytoskeleton element in force generation and neurite initiation. This could connect our results to reports on the disruption of the cytoskeleton in response to applied tensile force [1,39]. Adjusting other experimental parameters such as the magnitudes and application times of applied strain, the adhesion of the neurite to a substrate and the elongation of an existing axon instead of a newly-created process could also give insights into the mechanisms governing developmental axon stretch versus those governing traumatic axon injury reported in [26]. Other applications are to combine electrophysiological techniques with our platform and explore various axonal injury models [40].

Acknowledgements

The authors would like to acknowledge funding from the Natural Sciences and Engineering Reasearch Council of Canada (NSERC) as well as from the Fonds de recherche du Québec-Nature et technologies (FRQNT), Regroupements stratégiques program. We thank Andrew Kaplan and Alyson Fournier for the gift of the lentiviruses.

Appendices

.1 Image Acquisition

The sample, which consisted of embryonic rat hippocampal neurons contained in a fluid cell, rested on the piezo-actuated stage of an MFP-3D-BIO AFM mounted on an inverted optical microscope (Olympus IX-71). The piezo stage allows nanometer-resolved positional control in the sample plane via custom MATLAB codes applied through a 16 bit converter (National Instruments, NI-6002) linked to the MFP-3D sample piezo scanner. Images of the sample, magnified by the 40×PH microscope objective with 0.6NA, were recorded by a charged-couple device (CCD) camera (Cascade II by Photometrics) attached to the sideport of the microscope that streams image stacks to a connected central processing unit (CPU). Bright-field imaging was used to track particles. Noise in the system arising from the building and acoustic vibrations was minimized by placing the entire set-up on an active damping table (Herzan TS-Series) located within an acoustic insulation enclosure located on a passive optical table.

Images with resolutions of 512 × 512 pixels were acquired in our experiments at either 5.5 or 1 Hz rates with an exposure time of 75 ms. Our setup can achieve a temporal resolution of up to 20 Hz if the camera exposure time is adjusted and a smaller region of interest (ROI) is selected.

.2 Image Analysis.

The quality of the data was initially assessed with ImageJ. Factors considered included visibility of reference beads, whether or not the beaded probe tip eclipsed any other beads, and whether the pipette was raised sufficiently above the sample surface so as not to cause “stick-slip” events on the petri dish surface. Videos were rejected after analysis if pulls were not significantly different from the corresponding null experiment. Images were analyzed in MATLAB (Mathworks) using a custom-made centroid tracking algorithm (which is available upon request) as described in [9]. First, we manually isolate a bead from the initial field of view to a smaller region. As observed in the microscope, beads appear as dark semi-circles surrounding a high-intensity centre, the brightest spot on the image. Expressing each image as a matrix of intensities, $I(x, y)$, where x, y are the pixel coordinates, the centroid can be given in terms of the moment, M_{ij}, of an image, defined as

$$M_{\mathrm{ij}} = \sum_{x=1}^{L_x} \sum_{y=1}^{L_y} x^{\mathrm{i}} y^{\mathrm{j}} I(x, y). \tag{1}$$

In the above, the L_n are the respective dimension lengths in pixels. The image centroid is

$$(x_C, y_C) = \left(\frac{M_{10}}{M_{00}}, \frac{M_{01}}{M_{00}} \right). \tag{2}$$

Note that in Equations (1) and (2), a threshold has been applied such that all pixels in I corresponding to intensities below said threshold are assigned a zero value, ensuring only the brightest region of the image is tracked. Detecting and comparing the centroid of a particle in two successive images indicates the distance an object has travelled.

Bibliography

[1] Ahmadzadeh, H., Smith, D.H., Shenoy, V.B., 2014. Viscoelasticity of tau proteins leads to strain rate-dependent breaking of microtubules during axonal stretch injury: predictions from a mathematical model. Biophysical journal 106, 1123–1133.

[2] Alexander, B.F., Ng, K.C., 1991. Elimination of systematic error in subpixel accuracy centroid estimation [also letter 34 (11) 3347-3348 (nov1995)]. Optical Engineering 30, 1320–1332.

[3] Ares, J., Arines, J., 2004. Influence of thresholding on centroid statistics: full analytical description. Applied optics 43, 5796–5805.

[4] Athamneh, A.I., Cartagena-Rivera, A.X., Raman, A., Suter, D.M., 2015. Substrate deformation predicts neuronal growth cone advance. Biophysical journal 109, 1358–1371.

[5] Athamneh, A.I.M., Suter, D.M., 2015. Quantifying mechanical force in axonal growth and guidance. Frontiers in cellular neuroscience 9, 359.

[6] Bernal, R., Pullarkat, P.A., Melo, F., 2007. Mechanical properties of axons. Physical review letters 99, 018301.

[7] Bray, D., 1984. Axonal growth in response to experimentally applied mechanical tension. Developmental biology 102, 379–389.

[8] Bressloff, P.C., Levien, E., 2015. Synaptic democracy and vesicular transport in axons. Physical review letters 114, 168101.

[9] Cheezum, M.K., Walker, W.F., Guilford, W.H., 2001. Quantitative comparison of algorithms for tracking single fluorescent particles. Biophysical journal 81, 2378–2388.

[10] Chow, G.C., 1960. Tests of equality between sets of coefficients in two linear regressions. Econometrica: Journal of the Econometric Society , 591–605.

[11] Dai, J., Sheetz, M.P., Wan, X., Morris, C.E., 1998. Membrane tension in swelling and shrinking molluscan neurons. Journal of Neuroscience 18, 6681–6692.

[12] Dennerll, T.J., Lamoureux, P., Buxbaum, R.E., Heidemann, S.R., 1989. The cytomechanics of axonal elongation and retraction. The journal of cell biology 109, 3073–3083.

[13] Dotti, C.G., Sullivan, C.A., Banker, G.A., 1988. The establishment of polarity by hippocampal neurons in culture. Journal of Neuroscience 8, 1454–1468.

[14] Franze, K., Gerdelmann, J., Weick, M., Betz, T., Pawlizak, S., Lakadamyali, M., Bayer, J., Rillich, K., Gögler, M., Lu, Y.B., et al., 2009. Neurite branch retraction is caused by a threshold-dependent mechanical impact. Biophysical journal 97, 1883–1890.

[15] Fuhs, T., Reuter, L., Vonderhaid, I., Claudepierre, T., Käs, J.A., 2013. Inherently slow and weak forward forces of neuronal growth cones measured by a drift-stabilized atomic force microscope. Cytoskeleton 70, 44–53.

[16] Heidemann, S.R., Bray, D., 2015. Tension-driven axon assembly: a possible mechanism. Frontiers in cellular neuroscience 9, 316.

[17] Hochmuth, F., Shao, J.Y., Dai, J., Sheetz, M.P., 1996. Deformation and flow of membrane into tethers extracted from neuronal growth cones. Biophysical journal 70, 358–369.

[18] Hurtig, J., Chiu, D.T., Önfelt, B., 2010. Intercellular nanotubes: insights from imaging studies and beyond. Wiley Interdisciplinary Reviews: Nanomedicine and Nanobiotechnology 2, 260–276.

[19] Hutter, J.L., 2005. Comment on tilt of atomic force microscope cantilevers: effect on spring constant and adhesion measurements. Langmuir 21, 2630–2632.

[20] Hutter, J.L., Bechhoefer, J., 1993. Calibration of atomic-force microscope tips. Review of Scientific Instruments 64, 1868–1873.

[21] Kaplan, A., Morquette, B., Kroner, A., Leong, S., Madwar, C., Sanz, R., Banerjee, S.L., Antel, J., Bisson, N., David, S., et al., 2017. Small-molecule stabilization of 14-3-3 protein-protein interactions stimulates axon regeneration. Neuron 93, 1082–1093.

[22] Karhu, E., Gooyers, M., Hutter, J.L., 2009. Quantitative friction-force measurements by longitudinal atomic force microscope imaging. Langmuir 25, 6203–6213.

[23] Kostic, A., Sap, J., Sheetz, M.P., 2007. Rptpα is required for rigidity-dependent inhibition of extension and differentiation of hippocampal neurons. Journal of cell science 120, 3895–3904.

[24] Lamoureux, P., Ruthel, G., Buxbaum, R.E., Heidemann, S.R., 2002. Mechanical tension can specify axonal fate in hippocampal neurons. The Journal of cell biology 159, 499–508.

[25] Lobovkina, T., Dommersnes, P., Joanny, J.F., Hurtig, J., Orwar, O., 2006. Zipper dynamics of surfactant nanotube y junctions. Physical review letters 97, 188105.

[26] Loverde, J.R., Pfister, B.J., 2015. Developmental axon stretch stimulates neuron growth while maintaining normal electrical activity, intracellular calcium flux, and somatic morphology. Frontiers in cellular neuroscience 9, 308.

[27] Lucido, A.L., Sanchez, F.S., Thostrup, P., Kwiatkowski, A.V., Leal-Ortiz, S., Gopalakrishnan, G., Liazoghli, D., Belkaid, W., Lennox, R.B., Grutter, P., et al., 2009. Rapid assembly of functional presynaptic boutons triggered by adhesive contacts. Journal of Neuroscience 29, 12449–12466.

[28] Magdesian, M.H., Anthonisen, M., Lopez-Ayon, G.M., Chua, X.Y., Rigby, M., Grütter, P., 2017. Rewiring neuronal circuits: A new method for fast neurite extension and functional neuronal connection. JoVE (Journal of Visualized Experiments) , e55697.

[29] Magdesian, M.H., Lopez-Ayon, G.M., Mori, M., Boudreau, D., Goulet-Hanssens, A., Sanz, R., Miyahara, Y., Barrett, C.J., Fournier, A.E., De Koninck, Y., et al., 2016. Rapid mechanically controlled rewiring of neuronal circuits. Journal of Neuroscience 36, 979–987.

[30] Mondaini, R.P., Pardalos, P.M., 2008. Mathematical modelling of biosystems. volume 102. Springer Science & Business Media.

[31] O'Toole, M., Lamoureux, P., Miller, K.E., 2008. A physical model of axonal elongation: force, viscosity, and adhesions govern the mode of outgrowth. Biophysical journal 94, 2610–2620.

[32] Pfister, B.J., Bonislawski, D.P., Smith, D.H., Cohen, A.S., 2006. Stretch-grown axons retain the ability to transmit active electrical signals. FEBS letters 580, 3525–3531.

[33] Pfister, B.J., Iwata, A., Meaney, D.F., Smith, D.H., 2004. Extreme stretch growth of integrated axons. Journal of Neuroscience 24, 7978–7983.

[34] Rigby, M., Anthonisen, M., Chua, X.Y., Kaplan, A., Fournier, A., Grutter, P., 2019. Building an artificial neural network with neurons (submitted).

[35] Sánchez, F.S., 2011. AFM investigations of cellular response to environmental and local chemo-mechanical stimulus. McGill University (Canada).

[36] Shimamoto, Y., Kapoor, T.M., 2012. Microneedle-based analysis of the micromechanics of the metaphase spindle assembled in xenopus laevis egg extracts. Nature protocols 7, 959.

[37] Steketee, M.B., Oboudiyat, C., Daneman, R., Trakhtenberg, E., Lamoureux, P., Weinstein, J.E., Heidemann, S., Barres, B.A., Goldberg, J.L., 2014. Regulation of intrinsic axon growth ability at retinal ganglion cell growth cones. Investigative ophthalmology & visual science 55, 4369–4377.

[38] Suarez, F., Thostrup, P., Colman, D., Grutter, P., 2013. Dynamics of presynaptic protein recruitment induced by local presentation of artificial adhesive contacts. Developmental neurobiology 73, 98–106.

[39] Tang-Schomer, M.D., Patel, A.R., Baas, P.W., Smith, D.H., 2010. Mechanical breaking of microtubules in axons during dynamic stretch injury underlies delayed elasticity, microtubule disassembly, and axon degeneration. The FASEB Journal 24, 1401–1410.

[40] Tian, J., Huang, G., Lin, M., Qiu, J., Sha, B., Lu, T.J., Xu, F., 2019. A mechanoelectrical coupling model of neurons under stretching. Journal of the mechanical behavior of biomedical materials 93, 213–221.

[41] Waxman, S.G., Kocsis, J.D., Stys, P.K., 1995. The axon: structure, function, and pathophysiology. Oxford University Press, USA.

[42] Zhang, Y., Abiraman, K., Li, H., Pierce, D.M., Tzingounis, A.V., Lykotrafitis, G., 2017. Modeling of the axon membrane skeleton structure and implications for its mechanical properties. PLoS computational biology 13, e1005407.

[43] Zhang, Z., Menq, C.H., 2008. Three-dimensional particle tracking with subnanometer resolution using off-focus images. Applied optics 47, 2361–2370.

[44] Zheng, J., Lamoureux, P., Santiago, V., Dennerll, T., Buxbaum, R.E., Heidemann, S.R., 1991. Tensile regulation of axonal elongation and initiation. Journal of Neuroscience 11, 1117–1125.

Part IV

Neurite Geometry

Chapter 7

Quantifying Bio-filament Morphology Below the Diffraction Limit of an Optical Microscope Using Out-of-Focus Images

M. Anthonisen, Y. Zhang, M. H. Sangji and P. Grütter, *Quantifying Bio-filament Morphology Below the Diffraction Limit of an Optical Microscope Using Out-of-Focus Images*, Applied Optics 20;59(9):2914-2923 (2020).

Addendum for Thesis

Here we develop a method to obtain the diameters of extending neurites that are below the optical diffraction limit. In the introduction of this thesis, we listed several powerful techniques to circumvent the optical diffraction limit. We performed preliminary tests with several of them, but all had particular disadvantages. We needed a simple technique that could be applied to optical images of live neurites and were suitable to measure a tether structure that is suspended off the surface of the coverslip.

Information about neurite geometry is needed to determine the stress of neurites (force per unit cross sectional area). Diameter measurements, combined with force-extension curves obtained in Ch 6 are used in Ch. 8 to obtain material parameters of neurites and model the kinematics of neurite growth.

Abstract

A method to measure the dimensions of objects below the optical diffraction limit using diffraction analysis of out-of-focus bright-field images is presented. The method relies on the comparison of the diffraction patterns of an object of unknown size to those of calibration objects of known size. Correlative scanning electron microscope (SEM) measurements are used to demonstrate the applicability of this method to measure 100 nm microbeads as well as objects of a different geometry than the calibration objects. This technique is important in the context of tethered particle experiments, in which bio-filaments are bound between a substrate and a microbead. This procedure is applied to obtain the diameters of axonal extensions or neurites that are mechanically created in samples of rat hippocampal neurons. The dependence of neurite geometry on mechanical pull speed is investigated and the diameter is found to be rate-independent.

7.1 Introduction

There is a class of biological force measurement techniques that relies on the manipulation of a microbead to induce the formation of a tether from a cell. Examples include optical tweezer experiments to extract and measure tension in tethers containing lipids and/or cytoskeleton elements [1–5] as well as experiments where a bead is aspirated and maneuvered with a micropipette to create a long, tubular structure [6, 7]. In all of these examples, the tubes created have radii below the diffraction limit of the optical microscope, $\sim$250 nm [8]. Electron microscopy (EM) is a powerful tool to overcome the diffraction limit and was exploited to measure fiber radii in [4, 5]. However, the sample preparation process for EM involves fixation which eliminates observation of cell dynamics and can cause morphological changes [9,10].

Bright-field microscopy has the advantage of being able to observe unstained samples continuously for long periods (several days). However, a feature of conventional bright-field microscopy is limited contrast when observing near-transparent samples such as cells [11]. These can be effectively invisible in focus but become visible when the microscope is slightly defocused [11–13]. In the defocused state, small objects ($\sim 10\ \mu$m) create diffraction fringes in an image; even with a broad-band light source the objects are within a coherence area [13].

In this work, we present a method for measuring the dimension of individual structures below the diffraction limit that requires only an optical microscope/camera and calibration objects of known dimensions. We image the diffraction patterns created by an object of unknown size and a calibration object of known size in the same slightly out-of-focus image. By comparing these patterns to those in a so-called "calibration series" of out-of-focus images of objects of known dimension, the diameter of the unknown object can be determined to $\sim 15\%$ uncertainty, for diameters as small as ~ 100 nm. This method is ideally suited for the class of experiments described above that feature an object of known size (the microbead) together with a tether of unknown size. We validate this method by comparing diameters measured in this way to those obtained from SEM images of the same objects.

Furthermore, we show that in our set-up, the method does not depend on the refractive index or on the material of the unknown objects. Two light waves each passing through a different material will have a phase shift and the magnitude of this phase shift depends on the thickness of the material [14]. We show experimentally that this shift is negligible. This is important for biological applications, since cells will likely have different refractive indices than the calibration objects. We also demonstrate experimentally that the method yields correct results when used to measure an object of different geometry than the spherical calibration objects. Theoretically, this can be attributed to the relation between the point-spread-function (which is the distribution of light when a sub-resolution sphere is imaged) and the line-spread-function (the distribution of light created by a line in the image). The line-spread-function can be calculated from the point-spread-function but for most imaging systems, these two quantities are indistinguishable [15]. It is common practice to model the point-spread-function of a sphere using a Gaussian [11,16,17], which has a Gaussian line-spread-function with the same width [15]. Again, this is important for biological applications in which we want to measure cylindrical objects such as neurites. Our imaging conditions are also more general than those in many previous studies of biological systems with diffraction patterns that rely on knowledge of sample position in either the near-field or the far-field regime [20–22].

We demonstrate the scientific value of this method by applying it to determine the diameter of neurites created by mechanical pulling in samples of rat hippocampal neurons, see Fig. 7.1. Previous work— [23]—has shown that when a polystyrene bead coated with the polymer poly-D-lysine (PDL) contacts axons or dendrites, presynaptic structures form, which adhere to the bead. If the bead is pulled (in our case with a microneedle), the growth of an auxiliary structure, the neurite, is induced [7, 24, 25]. These neurites are cylindrical structures with diameters near the diffraction limit [7]. In the following, we use this technique to investigate if the diameter of neurites is affected by how fast we pull them. This result has important implications for questions of what limits neuronal growth and regeneration [26–28] as well as for experiments that seek to re-wire neuronal networks with existing neurons [24, 25, 29].

7.2 Materials and Methods

7.2.1 Experimental set-up

Optical images

All optical images were acquired in bright-field with an inverted optical microscope (Olympus 71-X, equipped with a 100 × oil-immersion objective, NA=1.44) and a CCD camera (Cascade II, Photometrics). The camera captures 512 × 512 pixel

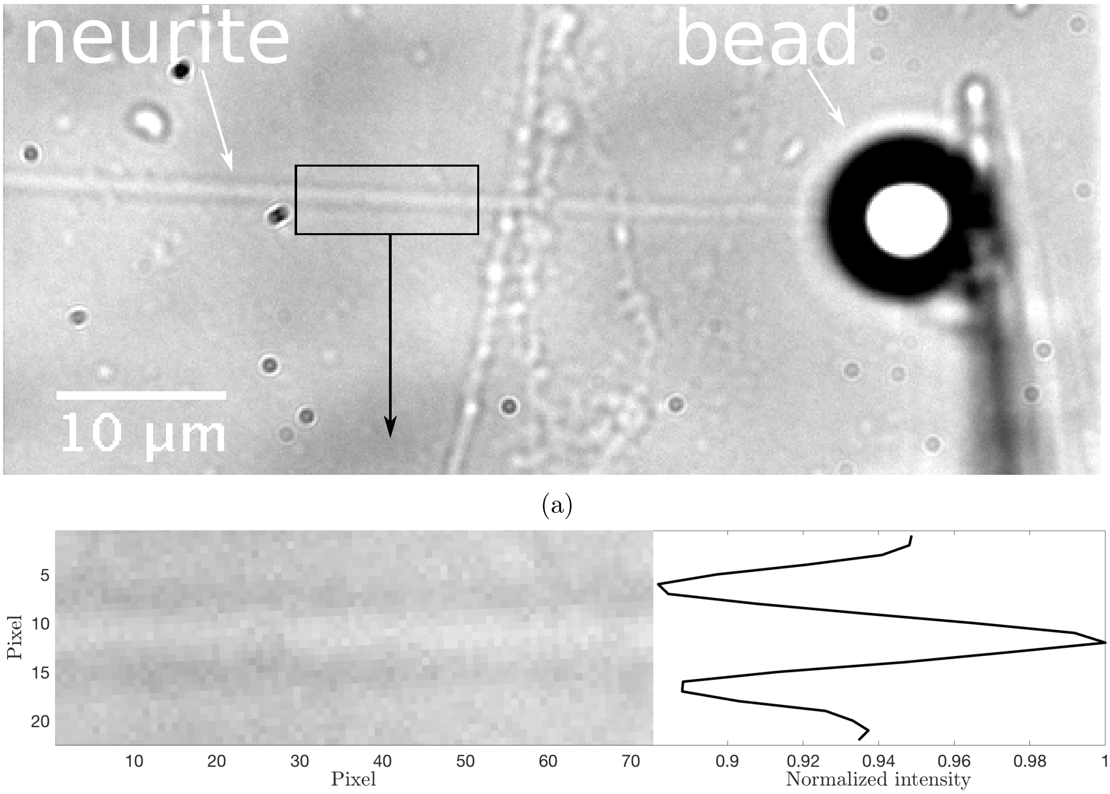

(a)

(b)

(c)

Figure 7.1 **(a)** Optical image of a neurite that is mechanically induced with a PDL-coated bead. **(b)** Isolated image of the neurite that has been rotated so its longitudinal axis is horizontal. **(c)** Both the neurite and the bead create diffraction patterns that can be used to extract the neurite diameter.

images with $16 \times 16\mu\text{m}^2$ pixel size. At the sampling plane, the spatial sampling width is $16\mu\text{m}/100=160$ nm. Samples were illuminated by a 12V halogen bulb. Experiments are performed with a common microscope setup, no special lenses or detectors are needed.

Neuronal cultures

All procedures were approved by McGill University's Animal Care Committee and conformed to the guidelines of the Canadian Council of Animal Care. Neuron samples containing PDL-coated beads were prepared following procedures outlined in [7, 24, 29]. Samples were imaged in cell media.

SEM images

Samples were imaged with a FEI Quanta 450 Environmental Scanning Electron Microscope (FE-ESEM) located at the Facility for Electron Microscopy Research at McGill University. To avoid charging effects, samples were coated with 4 nm platinum with a Leica EM ACE 600 High Vacuum Sputter Coater.

7.2.2 Diameter estimation

We describe a procedure for finding the diameter of an object by comparing its diffraction pattern to those of a set of beads in a series of out-of-focus images. Throughout the description, we refer to Fig. 7.2 for a schematic of the procedure. This method requires a so-called "test image", a single image that contains two objects, see panel (a) of Fig. 7.2. One object is of unknown dimension ("unknown object"), its width will be determined with the method, and the other object is a bead of known dimension ("known bead"). The method further requires a "calibration series" of images, again see Fig. 7.2a. This is an image stack of a set of beads of various known dimensions as a function of defocus. Each image in the stack is acquired at a different objective-focal plane separation z (i.e. different axial positions). One of the beads in this calibration series must be of the same dimension as the known bead in the test image. Using this calibration series and the known bead, one can determine the axial position of the microscope when the unknown object was imaged, as described in [30]. Since the calibration series contains beads of different and known diameters, this allows the determination of the unknown bead diameter. Surprisingly, as will be shown below, the method is effective down to ~100 nm with an accuracy ~ 15%, with potential of improvement if a more sophisticated camera and single wave-length illumination are used. In the following, we describe our process step-by-step, again see Fig. 7.2.

First the two-dimensional images of all the beads in the test image and the calibration series are converted to one-dimensional arrays called radius vectors [30]. Each 2D image of a bead, which is an intensity-function of the position on the image in pixels, has an associated radius vector. Each element of a radius vector I is the average intensity about an annulus concentric with the bead and the position of the element in the vector is the radius of the annulus as measured from the bead centre. See Fig. 7.2b for an example of a 2D image and its associated radius vector. To convert a bead image to a radius vector, we first isolate the individual bead from the initial field of view to a smaller region and identify its centre (in pixels) with a custom-made centroid tracking algorithm as described in [30–32]. We then assign cartesian coordinates to the circular bead image (with the origin at the bead centre) and convert that to a rectangle in the space defined by polar coordinates. The rectangle is collapsed to a vector by averaging along lines of constant θ—this is the radius vector and it contains the same information as the 2D image.

For each bead labeled D in the calibration series, a matrix M^D is constructed by taking the radius vector $[I_{1z_k} I_{2z_k} \dots I_{nz_k}]^T$ of the bead at each axial position z_k and inserting them into columns of a matrix. The collection of M^D matrices are shown in curly brackets $\{\}$ in Fig. 7.2 and an example of a radius vector is highlighted in a dashed red square. The results presented in this work are obtained with a calibration series of images at 16 different axial positions of 4 different sized beads, so we have $4\times$ M^D matrices each with 16 columns indexed by z_k where $k = 1, ..., 16$. The rows of each of these matrices are spline fit using linear interpolation to create a new series of matrices C^D, also shown in curly brackets $\{\}$ in Fig. 7.2. An example of a C^D matrix is displayed as a mesh plot in Fig. 7.2c. Note that the success of our method does not rely on acquisition of the different calibration images at a fixed interval in z; one does not need a precision motorized focus control for this method to work.

The axial position $z*$ of the test image is found following the method described in [30]. The radius vector $[m_1 m_2 \dots m_n]^T$ of the known bead in the test image is compared to each of the columns of the $C^{D=4}$ matrix that corresponds to the size of the unknown bead ($D = 4$ where 4 labels the bead in the calibration series that matches the bead of known dimension in the test image). This comparison is made via

$$J(z) = \sum_{i=1}^{n} [\rho_i(z) - m_i]^2, \tag{7.1}$$

where we have adopted the notation of [30] and $[\rho_1(z)\rho_2(z)\dots\rho_n(z)]^T$ are the columns of C^4. Gold, dashed arrows and boxes represent this matching procedure in Fig. 7.2. The known vector and the relevant column in C^4 are in gold, dashed boxes and are connected to J, also in a gold box, by gold arrows. The axial position $z*$ is found by minimizing $J(z)$.

Next a new matrix, N, is constructed by extracting and concatenating the columns with index $z*$ from each of the C^D matrices. The columns of this new matrix are thus each associated with a different bead diameter. For the results presented here we had 4 different sized beads in the calibration series generating 4 C^D matrices. Each matrix contributes a column to N, so here N will have 4 columns. The rows of N are again spline fit using linear interpolation to construct a diameter-calibration matrix P with columns $[\zeta_1(x)\zeta_2(x)\dots\zeta_n(x)]^T$ indexed by diameter x.

As before, the radius vector of the unknown bead in the test image, $[d_1 d_2 \dots d_n]^T$, (in a blue, dashed box in Fig. 7.2) is matched to a column of the diameter-calibration matrix P (also in a blue, dashed box) by minimizing

$$J_2(x) = \sum_{i=1}^{n} [\zeta_i(x) - d_i]^2. \tag{7.2}$$

The value of x that minimizes $J_2(x)$ is the diameter of the unknown bead. The matched quantities are shown in blue in Fig. 7.2.

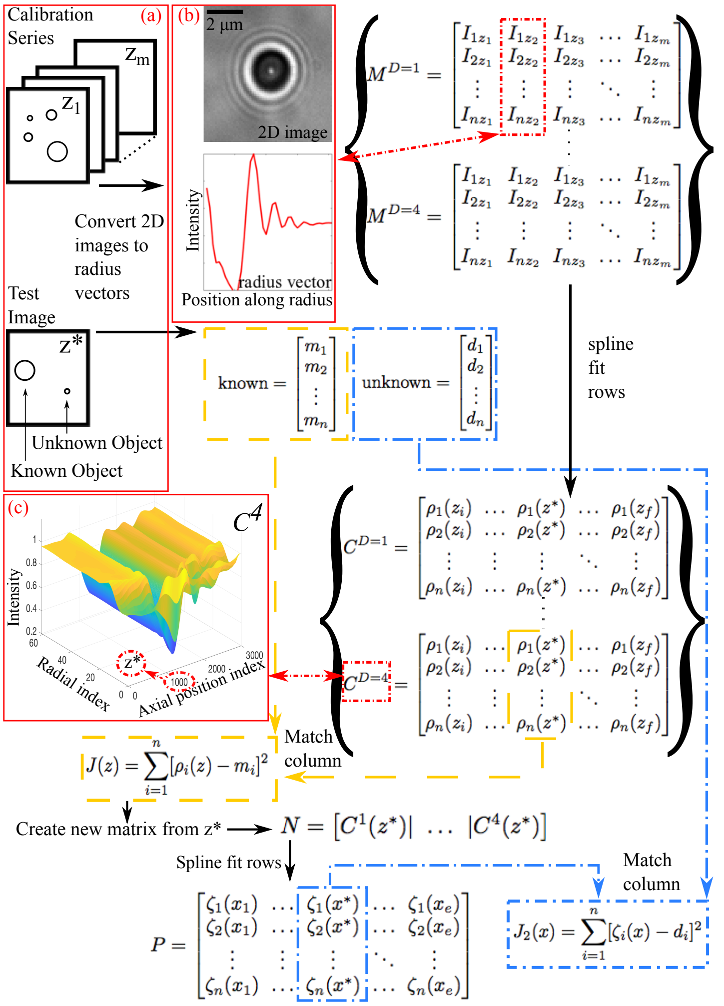

Figure 7.2 Schematic of procedure to extract bead diameter from out-of-focus images. **(a)** Sketch of a test image containing beads of known and unknown dimensions and a calibration series, which is an axial stack of images, labeled by z, of beads of known dimensions. **(b)** Image of a bead and its corresponding radius vector. Curly brackets: For each bead in the calibration series, a matrix M^D is constructed by concatenating the radius vectors from each image z_k of the calibration series. The rows of the M^D matrices are spline fit to create C^D (also shown in curly brackets). An example of a C^D matrix is plotted in **(c)**. The axial position of the test image z^* is found by matching the radius vector of the known bead to the column of the appropriate matrix C^D by minimizing $J(z)$ (gold boxes). Using z^*, N is constructed and spline fit to obtain P. The radius vector of the unknown object is compared to each column of P via $J_2(x)$ (blue boxes). The value of x that minimizes J_2 is the diameter of the unknown object.

7.2.3 Validation of method

We validate the method by applying it to find the diameters of objects of different dimensions and comparing the results to correlative SEM measurements; the results are shown in Fig. 7.3. Each histogram in Fig. 7.3 is from applying the method to beads of different nominal sizes from the manufacturer. We image an "unknown" bead multiple times at multiple different z values and determine its diameter using the method detailed above. The histogram in Fig. 7.3 is the combination of such measurements of several beads (4-5) of the same nominal diameter (e.g. the histogram for nominal diameter of 200 nm is from 5 different beads, each imaged at $\sim$20 different z values).

Fig. 7.3 shows the capability of this method to measure diameters down to 100 nm, the smallest size of object tested. The spread of each distribution is due to the combination of noise from the camera pixels and from sampling below the Nyquist limit. In [30], it is shown that the variance of pixel noise in the axial position estimation decays exponentially with the number of pixels in the radius vector, and so will the variance of pixel noise in the diameter estimation. Furthermore, this quantity is dependant on the objective-sample plane separation or z. It increases with increasing z and is at a minimum when the bead is in focus. Since larger beads can be imaged across a greater range of z values, their histograms include data from greater values of z which increases their spread. However, we note that the relative standard deviation of each histogram ultimately decreases with increasing bead size. Noise from sampling in this case should not depend on bead radius and will be discussed in a later section.

In Figs. 8.3 & 7.5, we validate the diffraction method by comparing the results to SEM measurements. In Fig. 8.3, we image the exact same sets of beads with the optical microscope and the SEM. We do this for beads with nominal diameters of 100 and 200 nm. We find the method to be accurate; in the case of the 100 nm-bead the percent difference between the two methods ranged from $\sim 2-21\%$ and in the 200 nm case the percent differences were $\sim 4\%$.

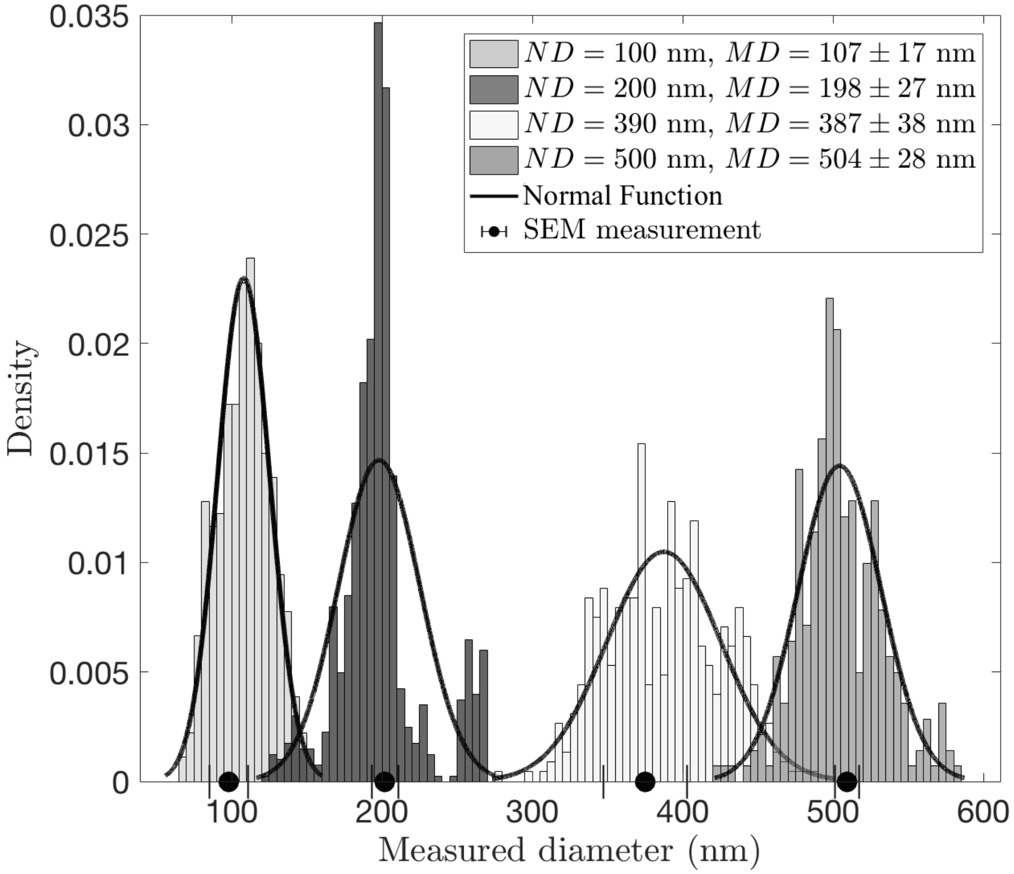

Figure 7.3 Histograms of bead diameters as measured by the diffraction method. Each histogram corresponds to measurements of a set of beads (4-5) with the same nominal diameter (labeled 'ND' in legend). The means and standard deviations of each histogram are also given in the legend, labeled 'MD=mean±SD' where 'MD' is for "measured diameter". Several beads of each size are also measured by SEM; the means and standard deviations of these measurements are shown for comparison (black dots). We also plot normal distributions (black lines) of width and average identical to measured diameters.

Verification of different materials

In Fig. 7.5a, we investigate the effects of the object material and the medium on the measured diameters. We apply the diffraction method to unknown beads of different materials: polystyrene, silica glass and silver, and find that the measured diameters match those obtained by SEM to within error. We also apply the diffraction method to polystyrene beads in water and find the diameters consistent with SEM results. This demonstrates that the method is robust in terms of the refractive index of the material to be measured and the environment in which it is imaged.

Verification of different geometries

We also check that the diffraction method can be applied to an unknown object with a different geometry than the calibration beads, since neurites are cylindrical rather than spherical. We apply the diffraction method to a borosilicate fiber and find a diameter of 636±64 nm, which is consistent with the diameter of 656 nm measured by SEM imaging. See Fig. 7.5b.

7.2.4 Estimation error

In our application of the method to cellular material, we take the standard deviation of repeated measurements to be the error in diameter, this is at the $\sim 15\%$ level for ~200 nm objects. This error is due to a combination of random noise from the camera and error from spatial sampling. Pixel noise enters into the radius vectors of the beads and effects the axial position estimation variance, as described in [30], as well as the diameter estimation variance. Our measurements are also subject to error due to spatial sampling at frequencies below the Nyquist limit. This occurs in two places. Firstly, in the determination of the axial position, each image in the calibration series provides columns to separate M^D matrices (each image provides one column for each different bead size). We assume that we are sampling discrete z-values of some continuous function of z. In our set-up, the step size between images is controlled by manually turning the focus knob and

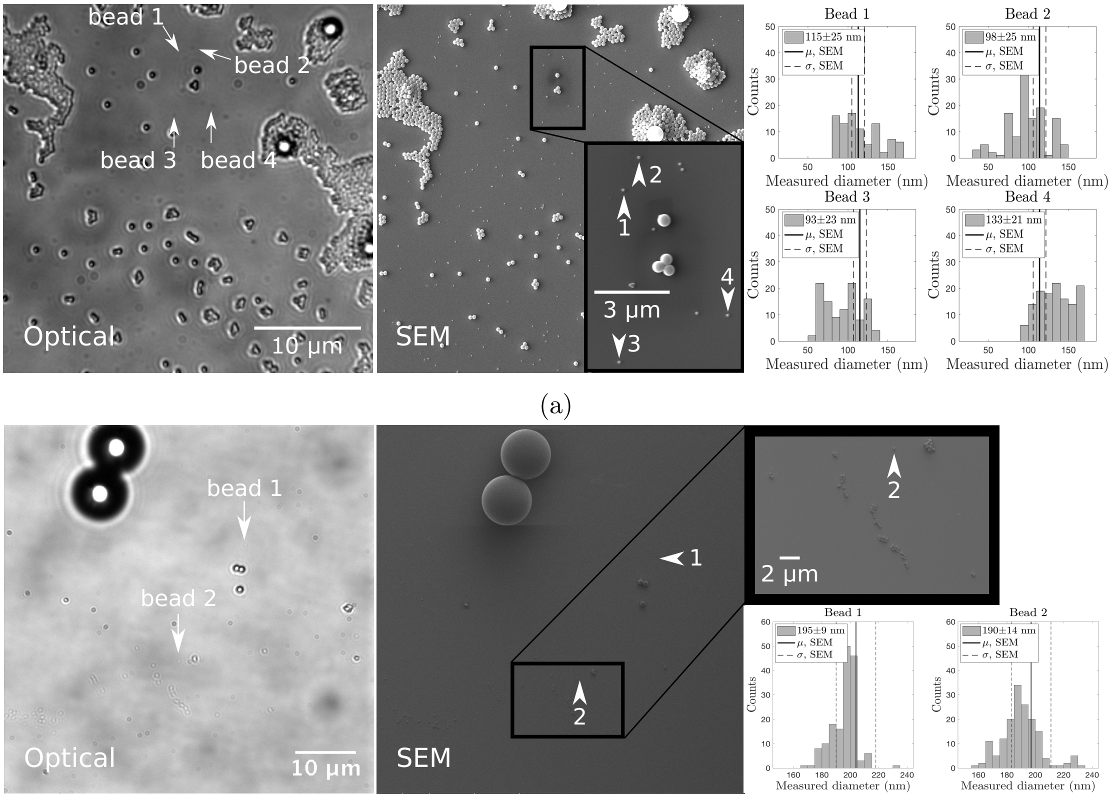

(a)

(b)

Figure 7.4 Validation of the method with SEM measurements. The same beads are imaged with an optical microscope and a SEM. Histograms are diameters of beads 1, 2, 3, 4 (white arrows) in **(a)** and beads 1, 2 (white arrows) in **(b)** measured with the diffraction method. The counts in the histograms are from taking measurements from images at different objective-sample plane separations. The means and standard deviations of the histograms are in the legends. The SEM results are plotted with the histograms for comparison; the solid lines represent the measured values and dashed lines are the uncertainties from the pixel size. **(a)** We confirm the capability of the method to measure beads with nominal diameters of 100 nm. The percent differences in the diameters as measured by the diffraction method and SEM range from ∼ 2% (Bead 1) to ∼21% (Bead 3). **(b)** We apply the method to beads with a nominal diameter of 200 nm and report percent differences of ∼ 4% between the two measurement methods.

so we are unable to sample steps below the Nyquist critical sampling distance in the axial direction. Precise control of the step-size, e.g. with a piezo stage, could lead to improved measurement error. Secondly, the construction of the N matrix introduces sampling noise. Here the step-size between different columns of N is determined by the sizes of the calibration beads. To eliminate this noise we would require many more different bead sizes.

We experimentally investigate the effects of pixel noise, inaccurate bead centres and bead position in the field of view. We find that the variance caused by each of these factors is less than or equal to the variance observed in measurements (data not shown). We considered the effect of spatial sampling by measuring the diameter with (separately) modified M^D and N matrices. We excluded up to half the columns of M^D and found that the variance in the diameter was stable. This could indicate we are near the maximum amount of noise from spatial sampling in the axial direction. Ultimately, improving sampling width in both M^D and N dimensions could improve the measurement error.

7.3 Application to determining the diameter of neurites

We apply this method to extract diameters of artificially generated neurites. We create these long cylindrical structures by a procedure described in [7,24,25], with the essential details summarized here. In brief, a PDL-coated polystyrene bead (10 μm in our measurements) is put in contact with an axon or a dendrite for sufficient time to form a synapse at the bead-cell interface. When the cellular structure is moved relative to the bead, an auxiliary structure, the neurite, is induced. In passing we note that these pulled neurites cannot be distinguished structurally or functionally from naturally grown neurites [7, 24]. Hippocampal axons are typically ~ 1 μm in diameter, the diameters of the pulled neurites branching from these can fall below the diffraction limit of our optical microscope.

One major motivation for developing this method was to answer the question "can we control the diameter of the pulled neurites by changing the pulling rate?" This could in turn clarify the dependence of action potential propagation on neurite diameter [33].

To determine the diameters, neurites and their corresponding diffraction fringes are identified by eye and isolated from an image (see Fig. 7.1). These image segments are then rotated so that the axis of the neurite is aligned with the horizontal axis. We then measure intensity versus pixel along lines perpendicular to the axis of the neurite (such that each pixel along the horizontal axis of the neurite has a corresponding line profile). From each line profile, we extract a diameter measurement by equating it to the radius vector of the unknown object. We take the centre of the neurite to be the first element of the radius vector. To determine if the neurite has a constant diameter along the entire box-size, we compute diameters for the mean of each line profile and its n-neighbours for $n = 1, ..., L_x$ where L_x is the horizontal dimension of the box in pixels. For each moving average size n, we compute the variance of the corresponding diameters. As long as this relation decreases monotonically, the neurite diameter is constant within the box.

Fig. 7.6 shows the diameters of neurites created by extending the neurite at different rates. Surprisingly, we see the spread in the measured diameters is the same over a 10-fold increase in extension rate. This is confirmed with the Kruskal-Wallis test ($p = 0.69$) which determines that the diameters, grouped by extension rate, are all drawn from the same distribution. The Pearson correlation coefficient between the logarithm of the extension rate and neurite diameter is $r = 0.04$, which confirms that the diameter does not change monotonically with extension rate. Therefore, extension rate is not an important predictor of cross sectional area of mechanically-created neurites.

7.4 Conclusion

In this work we present a method to obtain the size of objects that are smaller than the optical diffraction limit. This tool relies on matching the diffraction patterns of test objects to those in a series of out-of-focus optical images. In particular, this method does not require fluorescent labelling probes. This procedure enables us to measure objects with 100 nm diameters, which is similar to the size of structures that can be measured with classic structured illumination microscopy (SIM) [9, 19]. While in theory it is possible to obtain a 3-dimensional profile of objects with our method, we do not demonstrate this here. We note however, the limitations of this method with respect to the family of super-resolution techniques (see [9] for a review). We are unable to resolve different objects clustered together at the 100 nm length scale, we can merely extract their collective size. This method is thus best applied to structures that are isolated in the field of view, a condition met in e.g. optical tweezer experiments. In the same vein, we cannot discern individual components within a cell. Fluorescence microscopy could be used in conjunction with this technique to provide finer details of the cellular architecture and capture rapid motions in cells [34]. While fluorescence microscopy use is widespread, note that neurons are photo-sensitive [35] and fluorescence microscopy relies on exogenous labels making it sensitive to effects of phototoxicity and photostability from the excitation light [11, 36].

This method is not an alternative to super-resolution microscopy, which is extremely powerful in its capabilities. It may, however, be more convenient in certain contexts. Bright-field microscopy is simple and allows the continuous observation of unstained samples for long periods of time [11]. Many super-resolution techniques require specialized equipment such as lasers and both single molecule localization microscopy (SMLM) and stimulated emission depletion microscopy (STED) require specialized probes that can be sample-dependent [9, 19]. Finding a good sample-preparation recipe to perform the desired experiment can be a multi-month enterprise and can ultimately limit which experiments can be performed [37, 38].

Other works have used bright-field microscopy to achieve sub-resolution measurements. Amazingly, Ref. [39] demonstrated the visualization of microtubules, cylinders of $\sim$25 nm diameter, with a conventional bright-field set-up. This was achieved through so-called computer enhanced bright-field imaging, which involves averaging over multiple frames, background subtraction, spatial filtering, smoothing and enhancing images with spatial convolution routines. We present a different method that can be applied to structures suspended above the coverslip but we note that our results could be improved by adopting the techniques outlined in Ref. [39]. Ref. [13] also detailed a method to measure cell surface fluctuations by defocusing a bright-field microscope but this technique does not measure sub-resolution structures.

We apply this method to characterize the deformability of mechanically created neurites. Within our statistics, we do not find that the geometry of induced neurites depends on the pull speed at which they were created. In [7] it was shown that the force-extension relationship of neurites is also independent of pull speed. These results can be combined to obtain the material parameters of induced neurites which are in turn of interest for conditions of neuronal repair after injury and for predicting drug-neuron interactions. The independence of neurite width and pull speed is also significant for fundamental questions of axonal growth. The fact that speed is not a factor in neurite width implies that there is something else governing the size of neurites. All neurites in these experiments were induced with 10μm-size beads. An avenue of future study is to repeat these measurements with different bead size to see if this is a factor determining neurite width.

Acknowledgements

We thank David Liu and Weawkamol Leelapornpisit at the Facility for Electron Microscopy Research of McGill University for their invaluable help in sample preparation. We also thank Xavier Capaldi for help with SEM measurements.

Appendices

.1 Experimental Investigation of Error in Diameter Estimation

Here, we vary different parameters in the procedure and see how these affect the difference between the measured diameter of the unknown bead and the "true" value as measured by SEM.

We first determine the noise in a camera pixel by isolating a region of background and taking the standard deviation of the intensity of each pixel across a series of repeated images. We vary the objective-sample plane separation and then repeat. In Fig. 7, we plot the maximum standard deviation in the region versus the axial position index.

.1.1 Effect of Pixel Noise

Pixel noise enters directly into the radius vectors of the test image beads and the calibration series beads. We add gaussian noise with different variances to the test image, see Fig. 8a, c, e, and to the calibration image series, see Fig. 8 b, d, f, respectively. In both cases, the magnitude of the effects of the added noise are similar; both the difference between the expected value of the diameter (Fig. 8a, b) and the standard deviation of the measurement (Fig. 8c, d) increase with increasing variance of pixel noise. We see that for $\sigma_\eta = 75$, the percent standard deviation of the measurement is close to 10%. Given that a reasonable estimation for σ_η is ~ 25 (units of gray scale) we conclude camera noise is not the dominant source of error.

We can also see how the camera pixel noise propagates through the measurement by considering Fig. 8e, f and Fig. 9. Together these figures show how an offset in the estimation of axial position corresponds to an offset in the estimation of diameter. In Fig. 8e, f, we plot the difference in the axial position between a measurement with no noise added and a measurement with noise added, δz, versus standard deviation of noise added. In Fig. 9, we plot the difference in measured diameter to true diameter versus δz. We do this for three different true values of z. Thus for $\delta z \sim 250$ (the maximum value observed in Fig. 8f) we can expect a diameter shift of up to ~ 60 nm depending on z.

.1.2 Effect of Inaccurate Centre

In this subsection, we investigate the relationship between an inaccurate estimation of the bead centre and the resultant error in the diameter estimation. We separately vary the centres of the unknown and known beads in the test image as well as the centres of calibration beads with diameters matching the known and unknown beads. The difference between the measurement with an inaccurate centre and the SEM measurement is shown in Fig. 10a-d. We see that the difference is largest in the case where the centre of the known object in the test image is inaccurate. Similarly, the standard deviation in the measurement is largest when the centre of the known object is inaccurate (Fig. 10e-h). Once again, the difference in the diameter estimation is connected to the difference in axial position estimation. In Fig. 10i-l, we plot the difference in axial position estimation arising from inaccurate centres for different beads. We can again compare this to Fig. 9 to see how δz mediates δD. The measurement is thus most sensitive to inaccurate centre of the known object.

.1.3 Effect of Spatial Sampling

Here we consider the effects of spatial sampling on diameter estimation. Spatial sampling of the axial position is controlled by manually adjusting the objective-sample plane separation. If the Nyquist condition was met and the separation-step sizes were controlled with great precision, e.g. with a piezo stage, bias error due to spatial sampling could be eliminated. In Fig. 11a, c, we exclude different numbers of images from the calibration series (i.e. different z-slices) in our construction of the $M_1^{D_j}$ matrices. We show the difference between the diameters measured with $C_1^{D_j}$ matrices of different sizes and the SEM measurement. Interestingly, we see from Fig. 11a, c that the diameter estimation and the standard deviation of the estimation are stable under the elimination of up to 8 $z-$slices (half of what was used in Figs. 7.3-7.5 in the main text). This could be because we are near the maximum noise from sampling. We could improve our measurement by sampling at more $z-$slices.

We also explore the effect of spatial sampling of different bead radii in our construction of M_2. In Fig. 11b, d, we measure the diameter using C_2 matrices constructed by eliminating different columns of the $C_1^{D_j}$'s. Here we see the method is unreliable if we remove the column obtained from the $C_1^{D_1}$ matrix of the smallest bead, 200 nm. The method is also sensitive to the removal of 2 out of 4 columns.

.1.4 Effect of Uncertainty in Size of Calibration Beads

In our construction of the C_2 matrix, we assume the values assigned to the column indices, which correspond to the diameters of the calibration beads, are known. However, in reality these diameters each have some distribution. We explore the effects of this uncertainty by measuring the diameter of the unknown bead using a diameter of the smallest calibration bead of $\mu \pm \delta d$. The relationship between the difference of the measured diameter and the value obtained via SEM, δD, and δd is linear and shown in Fig. 12.

.1.5 Effect of Bead Position in Field of View

In this subsection, we use the diffraction method to measure the diameter of two separate unknown beads repeatedly but at different positions in the field of view of the microscope. Fig. 13 shows the results of these measurements. We see that the means and standard deviations are consistent across positions in the field of view so any optical limitations (such as lens defects or aberrations) do not vary significantly in the regions we investigated.

.2 Procedure to Extract Neurites From Optical Images

This section contains example figures to illustrate the procedure for selecting segments of neurites from optical images that could be used to measure diameters. For every pull there is a corresponding optical image of neurite(s) such as Fig. 14. The neurite is isolate by drawing boxes to contain as much of the neurite as possible while excluding “non-neurite” elements that could influence the measurement such as bright spots in the sample or dirt on the microscope lens (see arrows in Fig. 14). Each box is rotated so that the long axis of the neurite lies at 0 degrees. For each box, we verify that the diameter of the neurite is constant within the entire box-size. To do this, we compute we compute diameters for the mean of each line profile and its n-neighbours for $n = 1, ..., L_x$ where L_x is the horizontal dimension of the box in pixels. For each moving average size n, we compute the variance of the corresponding diameters. As long as this relation decreases monotonically, the neurite diameter is constant within the box. So for each box there is a corresponding graph, see Fig 15. We fit each graph with the function $\sigma_D(n) = 1/\sqrt{n}$ which indicates that shot noise dominates this process.

In the analysis described in the main text, we only consider neurites that were constant within the box. This is because our method cannot distinguish between diameter differences due to an intrinsic size change along the neurite or due to different segments of the neurite lying in different focal planes, unless there is another bead present in the image besides the one on the pipette tip. In cases where a difference in size was observed within a box, or between boxes, the largest possible segment closest to the bead was considered in the above analysis as this configuration most closely matches the calibration conditions. However, in > 0.9 cases, the neurite was constant across boxes.

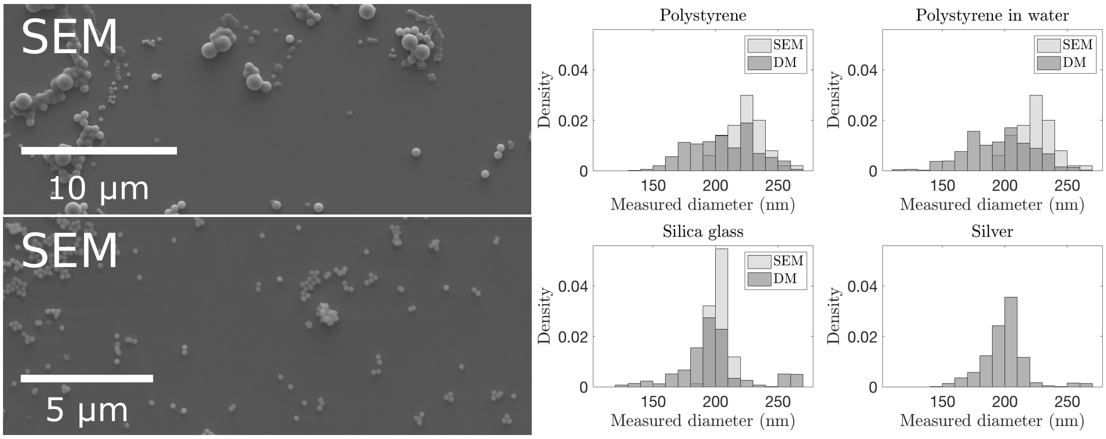

(a)

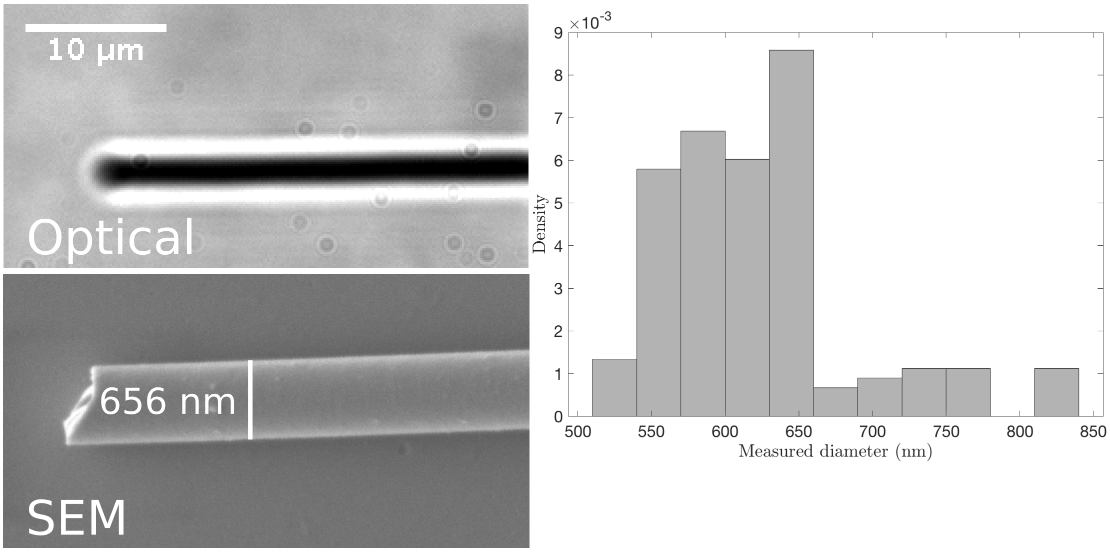

(b)

Figure 7.5 Verification of the method with SEM measurements. **(a)** Left: SEM images of polysytrene beads (top) and silica glass beads (bottom). Histograms of diameters of beads of different materials measured by SEM and by diffraction method (DM). DM-data is from images at different objective-focal plane separations of 5 different beads for each material. The two methods agree to within one standard deviation. **(b)** Optical and SEM images of a borosilicate fibre and the corresponding DM measurements. This confirms that the DM can be applied to unknown objects that have different geometries than the calibration objects.

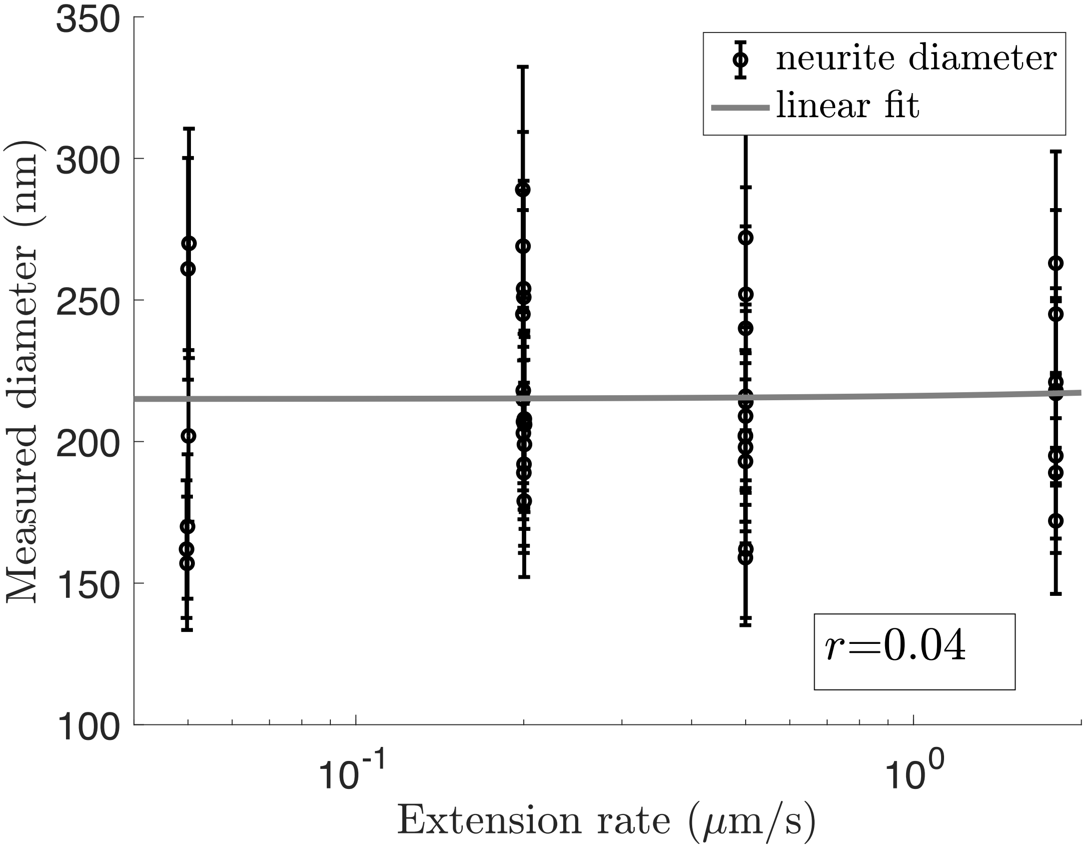

Figure 7.6 Diameters of neurites measured with the diffraction method for different extension rates (0.05 μm/s, 0.2 μm/s, 0.5 μm/s, 1.8 μm/s) plotted on a log scale. The distribution of the neurites is the same for each extension rate, as determined by the Kruskal-Wallis test. The Pearson correlation coefficient between the logarithm of extension rate and neurite diameter is $r = 0.04$, which indicates that the diameter does not change monotonically with extension rate. The linear relation associated with the correlation coefficient is plotted in grey.

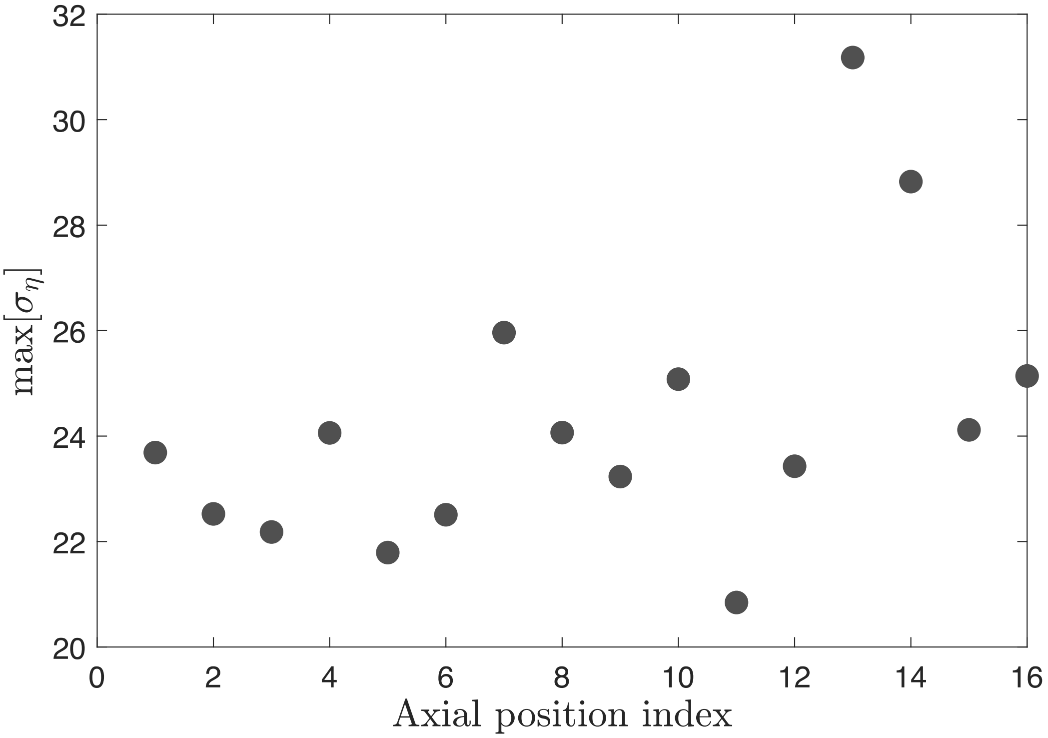

Figure 7 Determination of noise in a camera pixel. Maximum value of the standard deviation of pixel intensity in a region of background versus axial position index.

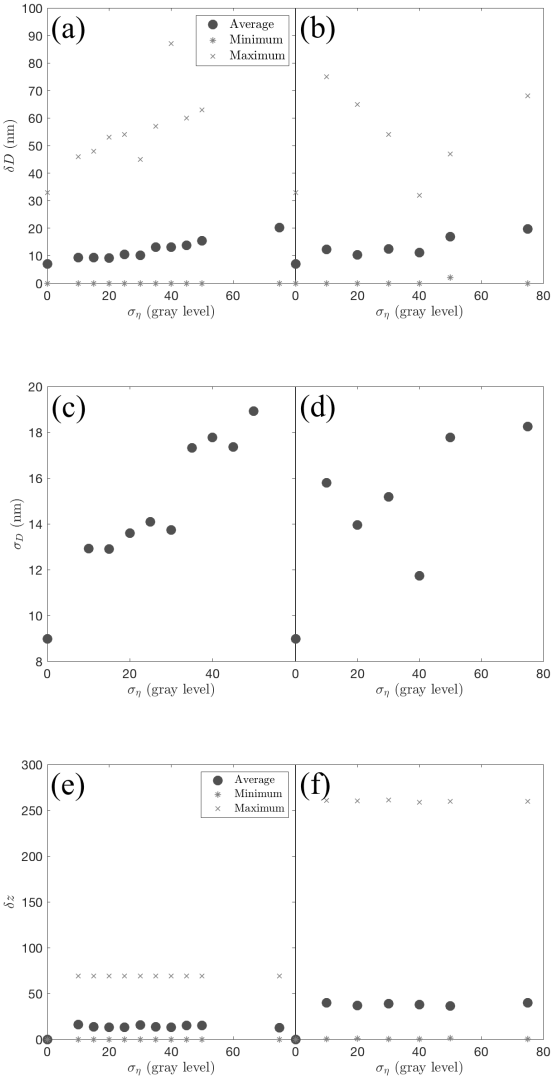

Figure 8 **(a-b)** Effect of camera pixel noise added to **(a)** the test image and **(b)** the calibration series on diameter estimation. The difference between the estimated diameter and the true value of the diameter as measured by SEM plotted versus different standard deviations of pixel noise added to the test image in **(a)** and the calibration series in **(b)**. We plot the difference averaged over several different z-separations (dots) as well as the maxima (crosses) and minima (stars) of all z-separations. **(c-d)** The standard deviation of the measured diameter (for several z-separations) versus standard deviation of pixel noise added. **(e-f)** Effect of camera pixel noise added to **(e)** the test image and **(f)** the calibration series on axial position estimation. The difference between the z-index measured using the diffraction method with no added noise and the z-index measured with pixel noise is plotted versus standard deviation of pixel noise added.

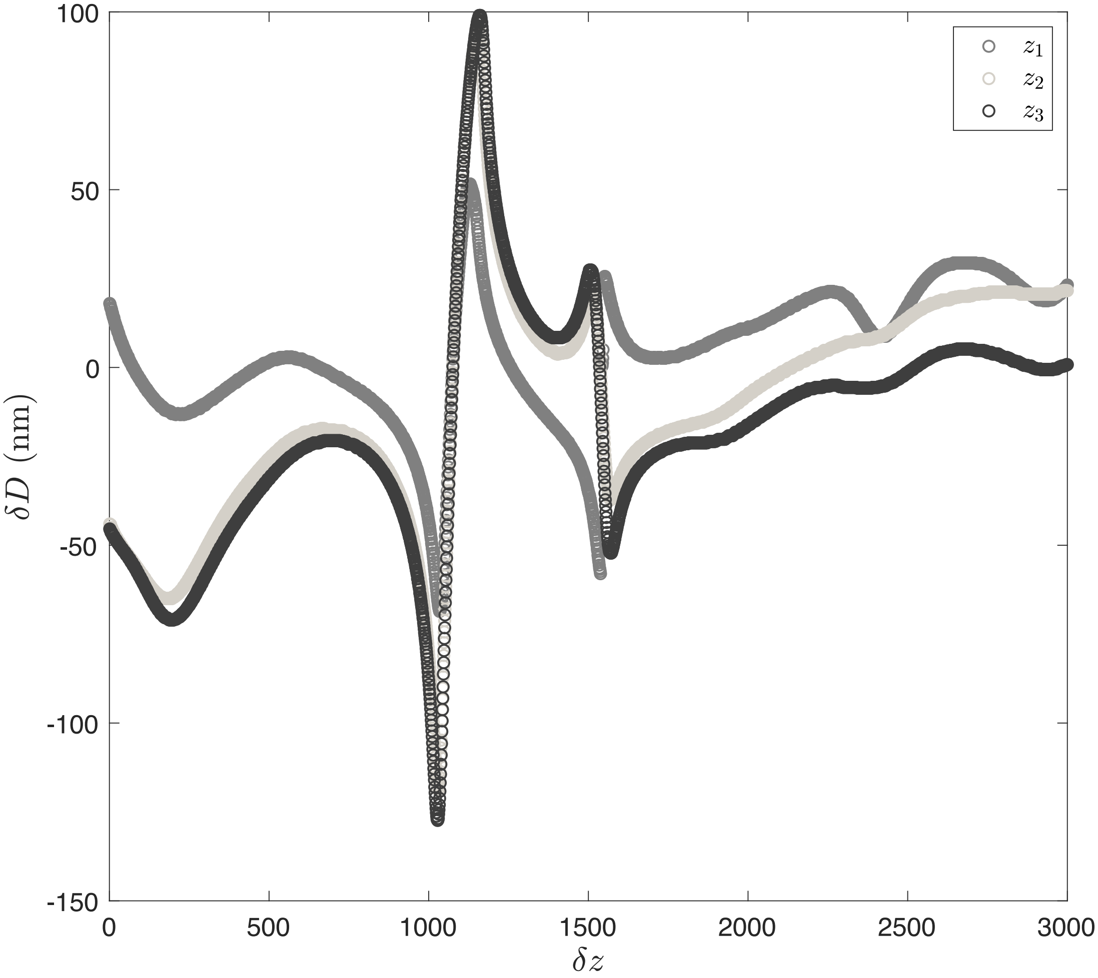

Figure 9 Effect of inaccurate axial position estimation on diameter estimation. The difference between the diameter of an unknown bead at a given z_i and its value as measured by SEM versus the value obtained by the difraction method for different values of axial position index. Curves are for three different values of the actual axial index.

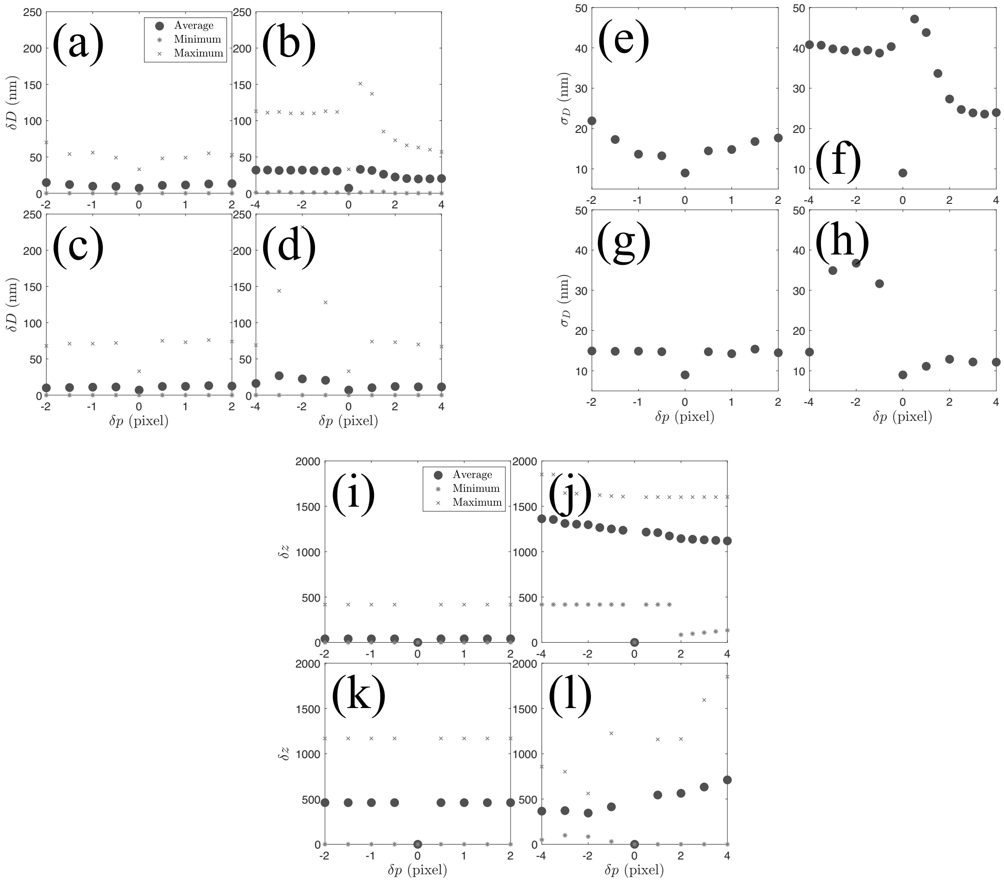

Figure 10 **(a-d)** Effects of moving the centre by δp pixels on diameter estimation. **(a)** Moving centre of unknown bead in test image. **(b)** Moving centre of known bead in test image. **(c)** Moving center of smallest bead in calibration series images. **(d)** Moving center of largest bead in calibration series images. **(e-h)** Standard deviations of diameter estimations with the centre of a bead moved by δp pixels. **(i-l)** Effect of shifting bead centres by δp pixels on axial position estimation. The difference between the z-index measured using the diffraction method with no centre-shift and the z-index measured with centre-shift is plotted versus centre shift in pixels.

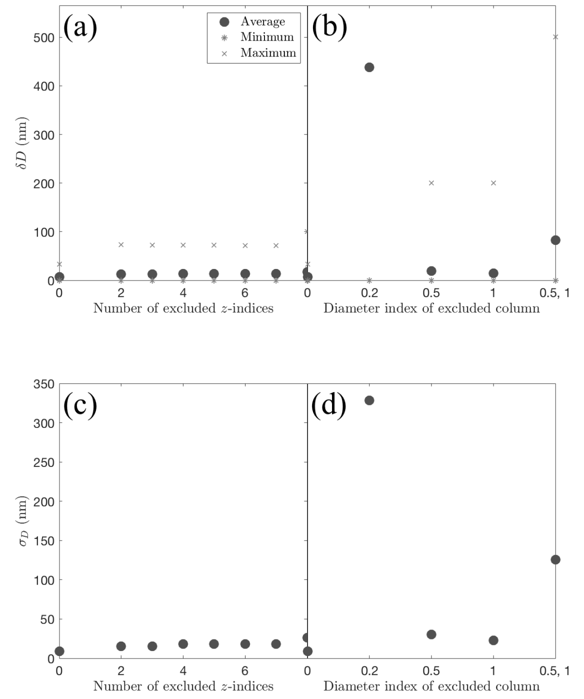

Figure 11 **(a)** We investigate the effects of sampling at different focuses. We construct the $C_1^{D_j}$ matrices using different numbers of images from the calibration series. The x-axis is the number of z-indexed columns excluded from the $M_1^{D_j}$ matrices and the y-axis is the corresponding difference in the estimated diameter (absolute value, as compared to the SEM-measured diameter). **(b)** We investigate the effects of sampling bead radii. We construct different M_2 matrices by excluding columns of different $C_1^{D_j}$. The bead sizes (μm) associated with these columns are plotted on the x-axis. We see the method becomes unreliable if we exclude the column from $C_1^{D_1=200\text{nm}}$. **(c-d)** Standard deviations of measurements made from excluding different numbers of columns from the $M_1^{D_j}$ matrices **(c)** and of measurements made from excluding different numbers of columns from the M_2 matrices **(d)**.

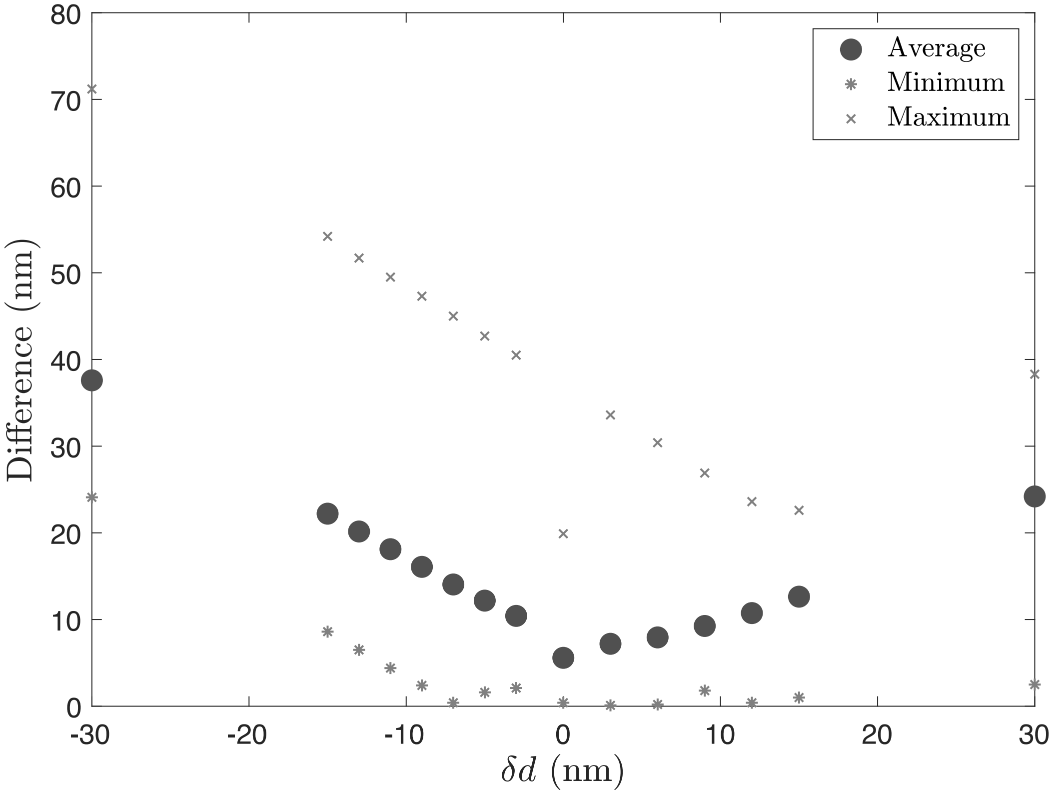

Figure 12 Effects of uncertainty in smallest calibration bead on diameter estimation.

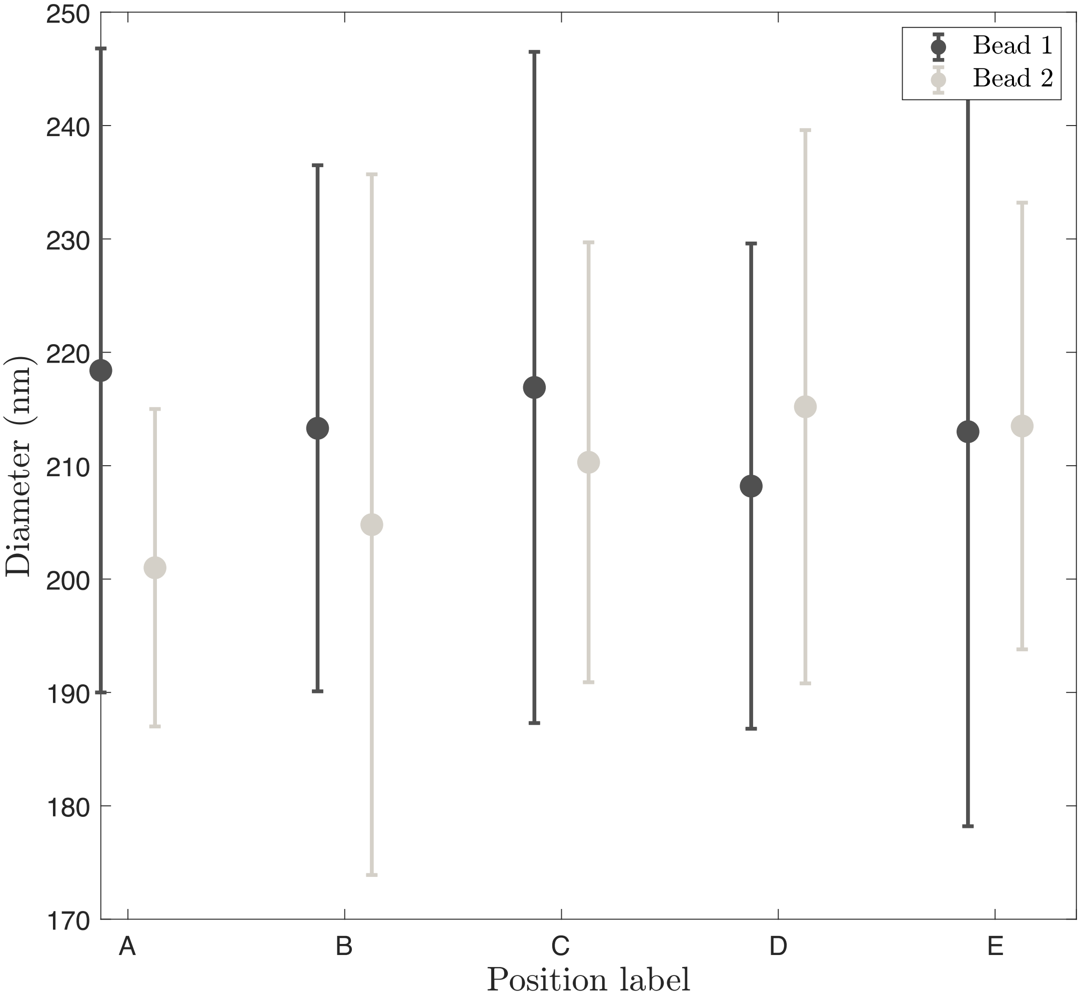

Figure 13 Diameter measurements of the same 2 beads at different positions in the field-of-view of the microscope. Points are the average diameter over different z-slices and error bars are the standard deviations. We see that for each bead, the measured diameters match to within error so the method is robust to changes in the field of view.

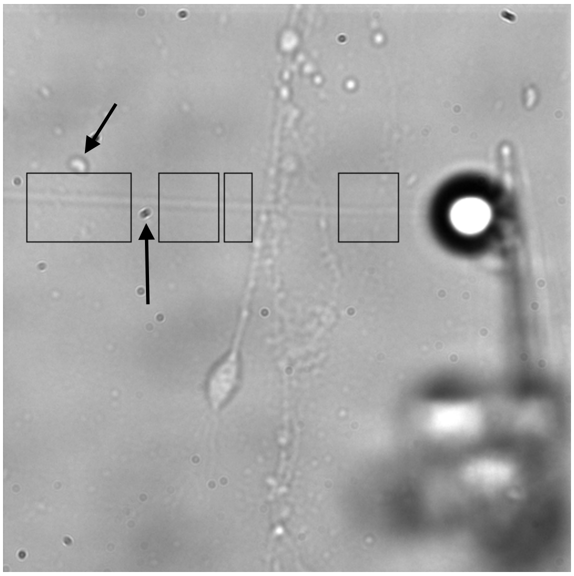

Figure 14 Optical image of a mechanically-created neurite. From left to right, boxes were rotated by angles of 1.9, 2.5, 2.5 and 0 degrees respectively. Black arrows indicate examples of features excluded from diameter analysis.

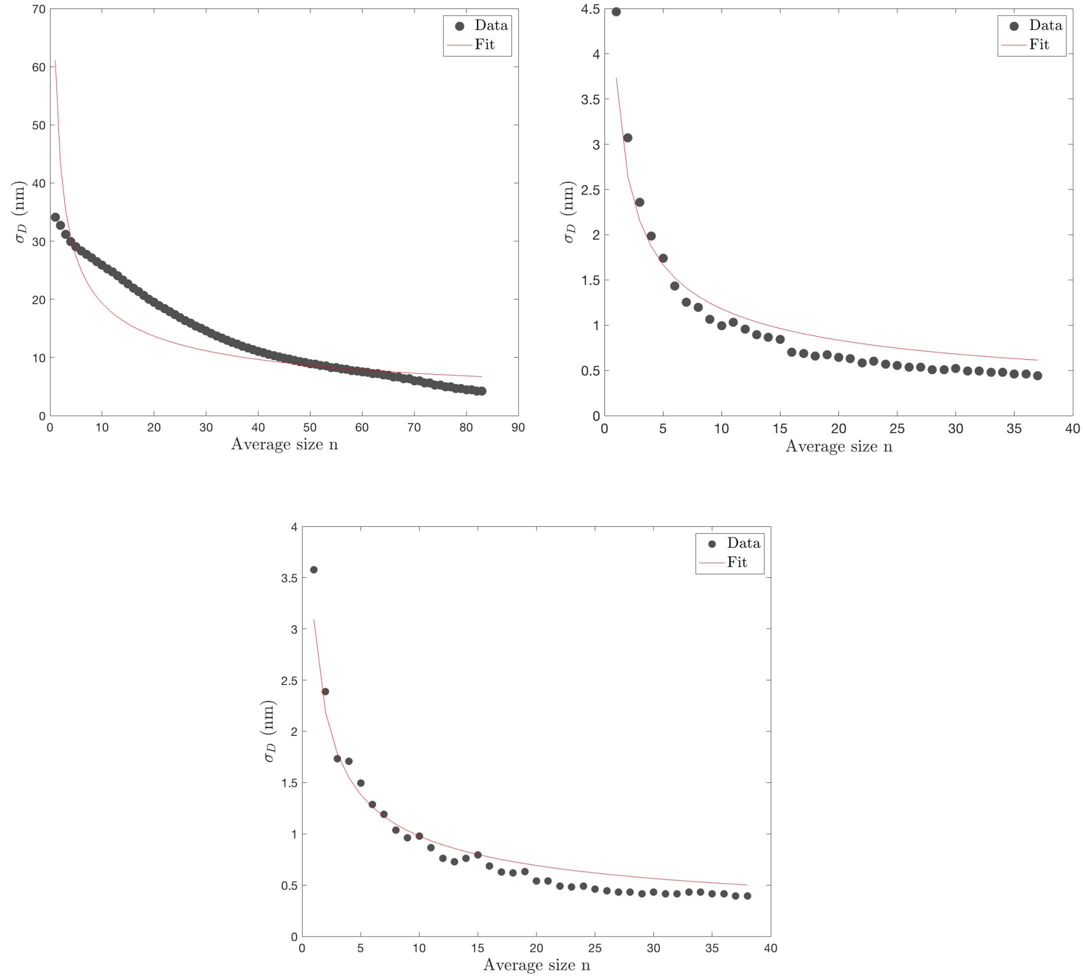

Figure 15 Size of neurite diameters for moving averages of size n within boxes in Fig. 14. As expected, the standard deviations decrease with more lines averaged. (Smallest box not shown). Fit functions are $1/\sqrt{n}$, indicating shot noise.

Bibliography

[1] J. Dai and M. P. Sheetz. Mechanical properties of neuronal growth cone membranes studied by tether formation with laser optical tweezers. *Biophysical journal* **68**, 988–996 (1995).

[2] J. Dai and M. P. Sheetz. Membrane tether formation from blebbing cells. *Biophysical journal* **77**, 3363–3370 (1999).

[3] B. Pontes, N. B. Viana, L. T. Salgado, M. Farina, V. M. Neto, and H. M. Nussenzveig. Cell cytoskeleton and tether extraction. *Biophysical journal* **101**, 43–52 (2011).

[4] B. Pontes, Y. Ayala, A. C. C. Fonseca, L. F. Romão, R. F. Amaral, L. T. Salgado, F. R. Lima, M. Farina, N. B. Viana, V. Moura-Neto *et al.*. Membrane elastic properties and cell function. *PLoS One* **8**, e67708 (2013).

[5] B. Pontes, P. Monzo, L. Gole, A.-L. Le Roux, A. J. Kosmalska, Z. Y. Tam, W. Luo, S. Kan, V. Viasnoff, P. Roca-Cusachs *et al.*. Membrane tension controls adhesion positioning at the leading edge of cells. *J Cell Biol* **216**, 2959–2977 (2017).

[6] D. Cuvelier, I. Derényi, P. Bassereau, and P. Nassoy. Coalescence of membrane tethers: experiments, theory, and applications. *Biophysical journal* **88**, 2714–2726 (2005).

[7] Anthonisen, M., M. Rigby, M. H. Sangji, X. Y. Chua, and P. Grütter, 2019. Response of mechanically-created neurites to extension. *Journal of the mechanical behavior of biomedical materials*.

[8] R. E. Thompson, D. R. Larson, and W. W. Webb. Precise nanometer localization analysis for individual fluorescent probes. *Biophysical journal* **82**, 2775–2783 (2002).

[9] Leterrier, C., P. Dubey, and S. Roy. The nano-architecture of the axonal cytoskeleton. *Nature Reviews Neuroscience* 18:713 (2017).

[10] Zhang, Y., T. Huang, D. M. Jorgens, A. Nickerson, L.-J. Lin, J. Pelz, J. W. Gray, C. S. López, and X. Nan, 2017. Quantitating morphological changes in biological samples during scanning electron microscopy sample preparation with correlative super-resolution microscopy. *PloS one* 12:e0176839.

[11] C. N. H. Candia and B. Gutiérrez-Medina. Direct imaging of phase objects enables conventional deconvolution in bright field light microscopy. *PloS one* **9**, e89106 (2014).

[12] U. Agero, L. Mesquita, B. Neves, R. Gazzinelli, and O. Mesquita. Defocusing microscopy. *Microscopy research and technique* **65**, 159–165 (2004).

[13] U. Agero, C. Monken, C. Ropert, R. Gazzinelli, and O. Mesquita. Cell surface fluctuations studied with defocusing microscopy. *Physical Review E* **67**, 051904 (2003).

[14] F. A. Jenkins and H. E. White. *Fundamentals of optics* (Tata McGraw-Hill Education, 1937).

[15] S. W. Smith *et al.*. *The scientist and engineer's guide to digital signal processing* (California Technical Pub. San Diego, 1997).

[16] F. Aguet, D. Van De Ville, and M. Unser. Model-based 2.5-d deconvolution for extended depth of field in brightfield microscopy. *IEEE Transactions on Image Processing* **17**, 1144–1153 (2008).

[17] J. Degerman, E. Winterfors, J. Faijerson, and T. Gustavsson. A computational 3d model for reconstruction of neural stem cells in bright-field time-lapse microscopy. in *Computational Imaging V,* vol. 6498 (International Society for Optics and Photonics, 2007), p. 64981E.

[18] M. H. Magdesian, M. Anthonisen, G. M. Lopez-Ayon, X. Y. Chua, M. Rigby, and P. Grütter. Rewiring neuronal circuits: a new method for fast neurite extension and functional neuronal connection. *JoVE (Journal of Visualized Experiments)* p. e55697 (2017).

[19] Schermelleh, L., R. Heintzmann, and H. Leonhardt, 2010. A guide to super-resolution fluorescence microscopy. *The Journal of cell biology* 190:165–175.

[20] Baskin, R., K. Roos, and Y. Yeh, 1979. Light diffraction study of single skeletal muscle fibres. *Biophysical journal* 28:45–64.

[21] Sundell, C., Y. Goldman, and L. Peachey, 1986. Fine structure in near-field and far-field laser diffraction patterns from skeletal muscle fibers. *Biophysical journal* 49:521–530.

[22] Mihailescu, M., and J. Costescu, 2012. Diffraction pattern study for cell type identification. *Optics express* 20:1465–1474.

[23] Lucido, A. L., F. S. Sanchez, P. Thostrup, A. V. Kwiatkowski, S. Leal-Ortiz, G. Gopalakrishnan, D. Liazoghli, W. Belkaid, R. B. Lennox, P. Grutter, et al., 2009. Rapid assembly of functional presynaptic boutons triggered by adhesive contacts. *Journal of Neuroscience* 29:12449–12466.

[24] Magdesian, M. H., M. Anthonisen, G. M. Lopez-Ayon, X. Y. Chua, M. Rigby, and P. Grütter, 2017. Rewiring neuronal circuits: a new method for fast neurite extension and functional neuronal connection. *JoVE (Journal of Visualized Experiments)* e55697.

[25] Rigby, M., M. Anthonisen, X. Chua, A. Kaplan, A. Fournier, and P. Grütter, 2019. Building an artificial neural network with neurons. *AIP Advances* 9:075009.

[26] Bernal, R., P. A. Pullarkat, and F. Melo, 2007. Mechanical properties of axons. *Physical review letters* 99:018301.

[27] Zhang, Y., K. Abiraman, H. Li, D. M. Pierce, A. V. Tzingounis, and G. Lykotrafitis, 2017. Modeling of the axon membrane skeleton structure and implications for its mechanical properties. *PLoS computational biology* 13:e1005407.

[28] Javid, S., A. Rezaei, and G. Karami, 2014. A micromechanical procedure for viscoelastic characterization of the axons and ECM of the brainstem. *Journal of the mechanical behavior of biomedical materials* 30:290–299.

[29] Magdesian, M. H., G. M. Lopez-Ayon, M. Mori, D. Boudreau, A. Goulet-Hanssens, R. Sanz, Y. Miyahara, C. J. Barrett, A. E. Fournier, Y. De Koninck, et al., 2016. Rapid mechanically controlled rewiring of neuronal circuits. *Journal of Neuroscience* 36:979–987.

[30] Zhang, Z., and C.-H. Menq, 2008. Three-dimensional particle tracking with subnanometer resolution using off-focus images. *Applied optics* 47:2361–2370.

[31] Cheezum, M. K., W. F. Walker, and W. H. Guilford, 2001. Quantitative comparison of algorithms for tracking single fluorescent particles. *Biophysical journal* 81:2378–2388.

[32] Alex von Diezmann, Yoav Shechtman, and WE Moerner. Three-dimensional localization of single molecules for super-resolution imaging and single-particle tracking. *Chemical reviews*, 117(11):7244–7275, 2017.

[33] Maia, P. D., and J. N. Kutz, 2014. Compromised axonal functionality after neurodegeneration, concussion and/or traumatic brain injury. *Journal of computational neuroscience* 37:317–332.

[34] Park, Y., G. Popescu, K. Badizadegan, R. R. Dasari, and M. S. Feld, 2006. Diffraction phase and fluorescence microscopy. *Optics express* 14:8263–8268.

[35] E. S. Boyden, F. Zhang, E. Bamberg, G. Nagel, and K. Deisseroth. Millisecond-timescale, genetically targeted optical control of neural activity. *Nature neuroscience* **8**, 1263 (2005).

[36] R. Hoebe, C. Van Oven, T. Gadella Jr, P. Dhonukshe, C. Van Noorden, and E. Manders. Controlled light-exposure microscopy reduces photobleaching and phototoxicity in fluorescence live-cell imaging. *Nature biotechnology* **25**, 249 (2007).

[37] Gražvydas Lukinavičius, Luc Reymond, Elisa D'este, Anastasiya Masharina, Fabian Göttfert, Haisen Ta, Angelika Güther, Mathias Fournier, Stefano Rizzo, Herbert Waldmann, et al. Fluorogenic probes for live-cell imaging of the cytoskeleton. *Nature methods*, 11(7):731, 2014.

[38] Anaël Chazeau, Eugene A Katrukha, Casper C Hoogenraad, and Lukas C Kapitein. Studying neuronal microtubule organization and microtubule-associated proteins using single molecule localization microscopy. In *Methods in cell biology*, volume 131, pages 127–149. Elsevier, 2016.

[39] B. Gutiérrez-Medina and S. M. Block. Visualizing individual microtubules by bright field microscopy. *American Journal of Physics*, 78(11), 1152-1159, 2010.

Part V

Material Parameters

Chapter 8

Growth and Elasticity of Mechanically-Created Neurites

M. Anthonisen and P. Grütter, *Growth and Elasticity of Mechanically-Created Neurites*, 2019. arXiv:1912.05735 [physics.bio-ph]

Addendum for Thesis

In this chapter, we develop a model for neurite growth and elasticity. We work in the framework of continuum mechanics introduced in Ch. 4. We use data collected in the previous chapters to find the best-fit model parameters, which are the material constants of neurites and the time constant associated with the addition of new cellular material. We use force-extension curves and diameter measurements to put new limits on the growth of neurites.

Abstract

Working in the framework of morphoelasticity, we develop a model of neurite growth in response to elastic deformation. We decompose the applied stretch into an elastic component and a growth component, and adopt an observationally-motivated model for the growth law. We then compute the best-fit model parameters by fitting to force-extension curves from measurements of constant-speed uniaxial deformations of mechanically-induced neurites of rat hippocampal neurons. We find a time constant for the growth law of 0.009 s^{-1}, similar to the diffusion rate of actin in a cell. Our results characterize the kinematics of neurite growth and establish new limits on the growth rate of neurites.

8.1 Introduction

Neurons are cells specialized for information processing. They have long, tube-like extensions of diameter ~ 1 μm, termed neurites, that connect the cell bodies to other neurons and enable the exchange of information via chemical and electrical signals. Neurites are classified as axons, signal transmitters, or dendrites, signal receivers.

Mechanical elongation of neurites has been widely studied (see e.g. [1, 2] for reviews). These experiments have lead to the identification of tension as a driver of neurite growth and development [3–6]; e.g. , "a pulled axon grows as though the nerve cell contained telescopic machinery prefabricated for elongation" [4]. Recent work, [7–9], has shown that this telescopic growth also occurs in axon-like structures initiated from parent axons or dendrites, see Fig. 8.1. However, the mechanisms responsible for this surprising mass-accretion and the role of tension in limiting this process remain outstanding mysteries [2–4, 10].

A natural question is the extent to which elongation can be attributed to growth, i.e. the addition of new cellular material, versus elastic stretching of existing constituents. In this paper, we answer this question.

Working in the theoretical framework of morphoelasticity described in [11–13], we relate the experimental force-extension curves of neurites to the material parameters that describe their elastic response to deformations and the rate as well as the rates of material added due to growth.

In our experiments, we measure the force-extension relationship of new neurites using flexible, calibrated glass micropipettes as illustrated in Fig 8.1. The micropipette is connected to the cell by a bead that is chemically functionalized to induce a stable mechanical contact with the parent axon or dendrite. When the bead-pipette complex is displaced relative to the cell, the growth of an auxiliary structure, a new neurite, is induced. We elongate the neurite while simultaneously measuring its tension by optically tracking the beaded tip. By calibrating the spring constant of the pipette, we can convert this deflection to a force. We extend our neurites at a constant rate, in contrast with other experiments, e.g. [14,15], in which a stretch is applied in one step and maintained constant for the duration of the experiment.

We derive an expression for the force-extension relationship of neurites that incorporates an exponential growth law. We fit experimental data to find the time constant for exponential mass addition, which is close to the rate of actin diffusion along a pulled neurite. We find that the time constants for different pulling experiments are positively skewed and follow a lognormal distribution. This puts new limits on the mass accretion of axon-like extensions.

The structure of this paper is as follows: In Section 8.2 we review the principles of morphoelastic theory and introduce a model to characterize the kinematics of neurite growth. We show the contributions of elastic stretching and growth stretching to neurite deformations in Section 8.3. In Section 8.4 we justify assumptions used in 8.2 with experiments, summarizing this paper in Section 8.5.

8.2 A model of growth with elastic deformation

A general deformation can be characterized by a geometric stretch λ, defined as the relative change in the length of the neurite to the initial length, i.e. $\lambda \equiv l/L$, with $l = l(t)$ and $L = l(t = 0)$ the length of the neurite at time t and the initial length respectively.

We work within the framework of morphoelasticity, in which the geometric stretch is the product of an elastic term λ^e and a growth term λ^g [10–13]:

$$\lambda = \lambda^e \lambda^g. \tag{8.1}$$

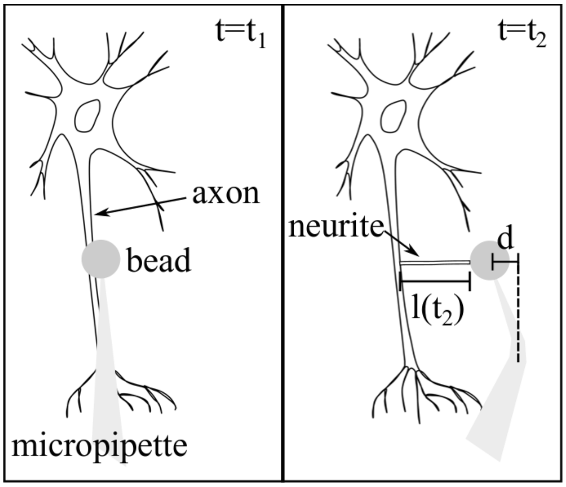

Figure 8.1 Sketch of a neurite pulling experiment. At time t_1, the micropipette tip is fixed to the bead that contacts the axon of a neuron. At time t_2, the micropipette-bead complex has been moved by an amount $v(t_2 - t_1)$ relative to the axon, inducing the growth of the neurite. The tension in the neurite is captured by recording the deflection of the micropipette, d, and calibrating its stiffness constant to convert the bending into a force.

We assume that stress, defined as the axial force per unit area of the neurite cross-section, is only caused by elastic deformation, a commonly-adopted assumption in growth theories [11,12]. We further assume that the elastic part of the deformation is incompressible (volume preserving) so that only the growth component will add volume.

In continuum mechanics, the stress-stretch relationship of soft materials is determined experimentally and can be derived from the strain energy density function of the deformation process. There are many different models to describe the strain energy density, we find that neurites are best described by the so-called Mooney-Rivlin model (this choice is justified in Sec. 8.4). Under the assumption of constant volume from the elastic deformation, the Mooney-Rivlin model has the form [11]

$$\Psi = c_1[I_1^e - 3] + c_2[I_2^e - 3], \tag{8.2}$$

where c_1, c_2 are material constants and $I_1^e = \lambda_1^{e2} + \lambda_2^{e2} + \lambda_3^{e2}$, $I_2^e = \lambda_1^{e2}\lambda_2^{e2} + \lambda_2^{e2}\lambda_3^{e2} + \lambda_1^{e2}\lambda_3^{e2}$ and $I_3^e = \lambda_1\lambda_2\lambda_3 = 1$ are elastic invariants in terms of the elastic stretches. Note $i = 1, 2, 3$ label the spatial dimensions of the deformation. In the case of incompressible uniaxial extension, the neurite is pulled along a single dimension, $\lambda_1^e = \lambda^e$ and $\lambda_2^e = \lambda_3^e = 1/(\lambda^e)^{1/2}$.

We can re-write the Mooney-Rivlin strain energy density function in terms of the elastic stretch and then reparameterize it in terms of λ, λ^g [11]:

$$\Psi(\lambda, \lambda^g) = c_1\left[\left(\frac{\lambda}{\lambda^g}\right)^2 + 2\frac{\lambda^g}{\lambda} - 3\right] + c_2\left[2\frac{\lambda}{\lambda^g} + \left(\frac{\lambda^g}{\lambda}\right)^2 - 3\right]. \tag{8.3}$$

From Eq. 8.3, we can obtain the elastic Piola stress P^e, which can be used to obtain the Piola stress P, defined as [11]:

$$P \equiv \frac{\partial\Psi}{\partial\lambda}. \tag{8.4}$$

This can be expanded in terms of λ and λ^g as [11],

$$P = \frac{2}{\lambda^g}\left[c_1 + c_2\frac{\lambda^g}{\lambda}\right]\left[\frac{\lambda}{\lambda^g} - \left(\frac{\lambda^g}{\lambda}\right)^2\right]. \tag{8.5}$$

The Piola stress captures the stress across the neurite. It can be related directly to an external loading force F on a neurite through the principle of virtual work [11, 16] to give

$$F = PA, \tag{8.6}$$

where A is the cross-sectional area.

The radial dimension of the neurite is a proxy for growth through addition of new material [11]. In the absence of radial thickening, the transverse stretch $\lambda^{\perp}$, that is the ratio between the neurite radius at a time t, $r(t)$, and the initial radius R, is defined via the elastic stretch,

$$\lambda^{\perp} = \left(\frac{1}{\lambda^e}\right)^{1/2}. \tag{8.7}$$

The cross sectional area of a neurite can also be written in terms of λ, λ^g:

$$A = \pi R^2\left(\frac{\lambda^g}{\lambda}\right). \tag{8.8}$$

This allows the force F to be written in terms of λ and λ^g, and the parameters c_1 and c_2, as

$$F = \frac{2\pi R^2}{\lambda}\left[c_1 + c_2\frac{\lambda^g}{\lambda}\right]\left[\frac{\lambda}{\lambda^g} - \left(\frac{\lambda^g}{\lambda}\right)^2\right]. \tag{8.9}$$

From this one can compute not only the force at a given deformation, but also the full time evolution $F(t)$.

Indeed, axons under axial tension will gradually increase in mass to recover some homeostatic equilibrium state, that is the axon has been observed to have some inherent tension [11, 12, 15, 17]. Motivated by these observations, here we adopt a growth model in which the growth rate depends on the axial stress of the neurite. If the neurite is perturbed from that state, mass will be added so it can recover a particular "baseline" stress. To model growth, we assume a functional form of λ^g based on experimental observations.

8.2.1 An exponential growth law

Here we consider a growth law that states exponential growth or resorption occurs until a homeostatic stress is recovered. This model has been used to describe axonal growth in [13]. Work from our lab indicates that the trajectory of actin (one of the principal constituents of neurites) entering the pulled neurite follows an exponential relation [18].

We consider a law of the form,

$$\frac{\partial \lambda^g}{\partial t} = k\lambda^g\,(\lambda^e - \lambda^*)\,\Theta(\lambda^e - \lambda^*), \tag{8.10}$$

where k is a constant, λ^* is a critical stretch associated with the homeostatic stress σ^* that the neurite is trying to recover, and $\Theta(x)$ is a Heaviside theta function: $\Theta(x)$ is 1 for $x > 0$ and 0 otherwise.

For $\lambda^e > \lambda^*$, Eq. 8.10 is

$$\frac{\partial \lambda^g}{\partial t} = k(\lambda - \lambda^g\lambda^*). \tag{8.11}$$

Solving for the functional form of $\lambda^g(t)$ with the initial condition $\lambda^g(0) = 1$, we obtain

$$\lambda^g(t) = \frac{k(L + vt) + v(e^{-kt} - 1)}{kL}, \tag{8.12}$$

where we have used $\lambda = (L + vt)/L$, v is the (constant) speed at which neurites are extended. We set $\lambda^* = 1$, an assumption we justify in a later section.

In what follows, we will experimentally measure force-extension curves, and from this obtain the best-fit values of the parameters k, c_1 and c_2 . Example experimentally-obtained force-extension curves are shown in Fig. 8.2. Here we have fit the curves to the functional form Eq. 8.9 with Eq. 8.12 inserted.

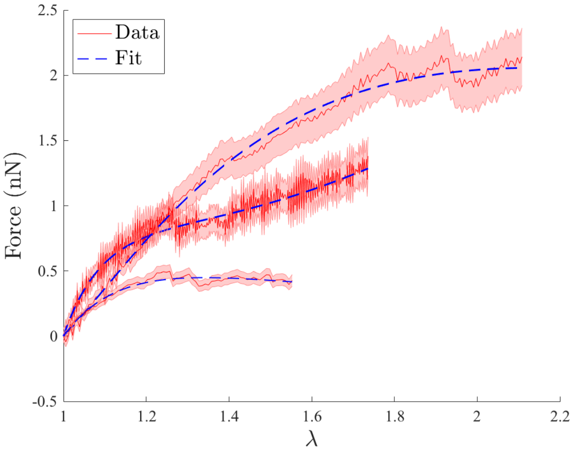

Figure 8.2 Examples of force-extension curves of induced neurites. Each curve (red) is from a single pulling experiment and can be due to 1 or more mechanically-induced neurites. The force is the loading force applied axially to the neurite(s) as measured by the bending of the micropipette and the stretch λ is the length the neurites have been pulled relative to their initial length. The shaded regions of the curves represent the measurement error and are calculated as described in [9]. The dashed blue lines are fits of Eq. 8.9.

8.2.2 Material parameters

We fit twenty-one experimentally-obtained force-extension curves with Eq. 8.9 and Eq. 8.12 as described in Section 8.2.1. The growth rate parameter k is shown in Fig. 8.3a for different pull speeds. We find the mean value of k to be 0.009 s^{-1}, see Table 8.1. The data is skewed to large values of k, with a SD of 0.01 s^{-1}. The mean is of a similar order of magnitude as the time constant describing the movement of actin along pulled neurites found in [18], which is 0.001 s^{-1}. The lower bound of our data matches the value found in [10] for the axonal growth rate, 2×10^{-5} s^{-1}. In Fig. 8.3b, we plot the cumulative density function of k values and show that it is well-characterized by a lognormal distribution with parameters $\mu = -5.31 \pm 0.01$ and $\sigma = 1.52 \pm 0.01$ (standard errors from fit). This is confirmed by a Chi-Square goodness of fit test at the 5% significance level. Here μ and σ are the mean and standard deviation of the natural logarithm of k. The skewness, which captures the asymmetry of the distribution, can be obtained from σ and is 33. Although this is significantly higher than 0.9, which is the sample skewness obtained from the definition of Pearson's moment coefficient of skewness, the two measures of skewness are consistent in describing the data as moderately to highly skewed.

We investigate the mass addition of new neurites as they are pulled, and find that k is independent of pull speed. This is confirmed by the Kruskal-Wallis test, which tests whether samples, grouped by pull speed, are drawn from the same distribution. This isconsistent with previous work, [9,19], which found that neither the force-extension relationships nor cross-sectional areas of neurites depend on mechanical pull speed. This is surprising given a greater than 10-fold increase in pull speed. Interpreting k as an exponential growth rate, it is reasonable that it should be the same across pull speeds as it could be constrained either by the properties of the cell (the speed with which it can manufacture and transport certain constituents) or by physical properties such as diffusion.

An open question is what causes the large variance in the k-values we extract, assuming this is not a feature that vanishes with more statistics. We postulate that this is related to the mechanisms underlying mass addition. Cell growth is typically modelled as a combination of active and passive processes. As mentioned, our timescales are consistent with those reported for actin in [18]. Motivated by this, we consider the behaviour of actin filaments and myosin motors (the proteins responsible for polymerizing actin filaments) in a simplistic 1D diffusion model. We calculate the time it takes actin filaments and myosin motors, which together have an effective diffusion coefficient of $D = 0.01\ \mu\mathrm{m}^2\mathrm{s}^{-1}$ [20], to diffuse along a length equivalent to L for each neurite. We find a mean rate of actin diffusion of $0.01\ \mathrm{s}^{-1}$ across neurites with a standard deviation of $0.01\ \mathrm{s}^{-1}$ that exactly matches our results for k. This is suggestive of an important role for actin diffusion in the addition of mass to new neurites. It also indicates that the variance in our reported values of k could be explained by different initial neurite lengths.

The other material parameters, which characterize the neurite response to elastic stretch in the Mooney-Rivlin model, are $c_1 = 204 \pm 385$ kPa and $c_2 = -13 \pm 302$ kPa (mean±SD). These are summarized in Table 8.1. Unlike k, the physical reason these parameters vary over orders of magnitude and, in the case of c_2, by sign is unclear. The Mooney-Rivlin model and the Neo-Hookean model, which is a specific case of the MR Eq. 8.2 [21], have been widely used to model other types of brain tissue [22–24], including axons [10]. While this family of models is succesful in describing brain tissue under diverse experimental conditions, these other works also contain the feature that the material parameters are phenomenological and vary over orders of magnitude [11]. In [25], it is shown analytically that the Mooney-Rivlin model, applied with different relative parameter signs, captures experimental trends observed in soft biological tissues under both shear and compression conditions. Our results add to the experimental evidence that the Mooney-Rivlin model is suitable to describe brain tissue. This indicates that the mechanical behaviour of newly induced neurites is very similar to that of naturally grown axons. While we lack a satisfying mechanistic interpretation of these parameters, quantifying single-cell behaviour with the Mooney-Rivlin model is an important step to multiscale modelling of the brain which could in turn ultimately clarify the physical significance of these results.

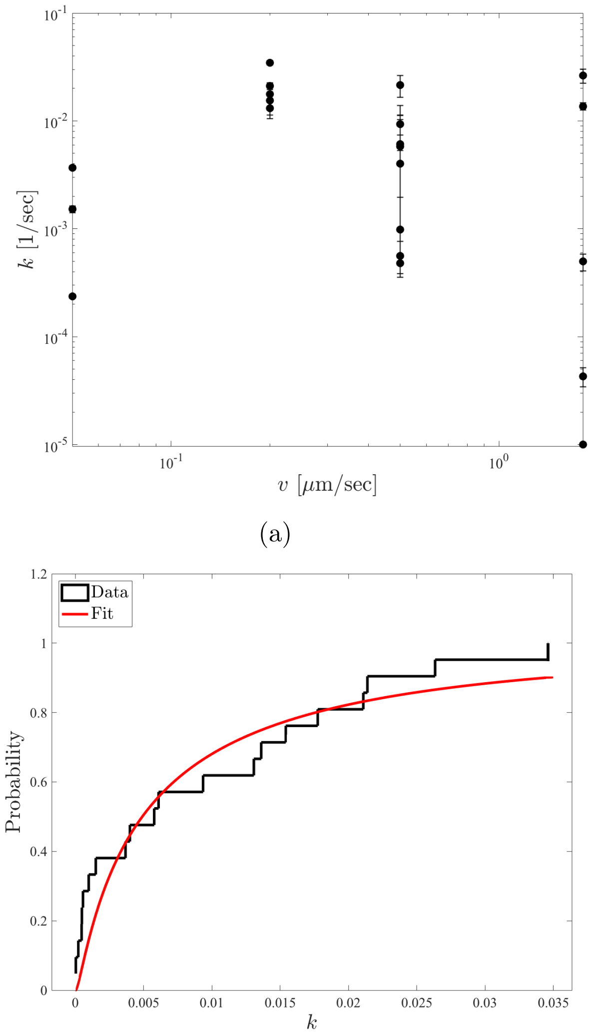

(a)

(b)

Figure 8.3 **(a)** Time constants characterizing neurite growth plotted versus pull speed. This is the fit parameter k from Eqs. 8.9&8.12. The Kruskal-Wallis test confirms the hypothesis that k values for each pull speed were all drawn from the same distribution. The mean value of k across pull speeds is 0.009 with a standard deviation of 0.01. **(b)** Cumulative density function for k values (black line), fit with a lognormal distribution (red line) that captures the skewness of the data. Parameters for the lognormal distribution are $\mu = -5.31$ and $\sigma = 1.52$.

Table 8.1 Fit parameters from Eqs. 8.9&8.12.

Parameter	Mean	Standard deviation
k	0.009 s^{-1}	0.01 s^{-1}
c_1	204 kPa	385 kPa
c_2	-13 kPa	302 kPa

8.3 Neurite growth

In Fig. 8.4 we plot the component of neurite stretch that is due to added mass, λ^g, versus time. Each curve represents one pulling experiment and we plot Eq. 8.12 with the k corresponding to the force-extension curve. These curves show the rapidity with which new material is added to neurites as they are being pulled. They represent the volume growth of neurites.

With the exception of $v = 0.05$ μm/s, the λ^g curves take on a range of values for a single pull speed. As discussed in Section 8.2.2, this could be due to the different initial lengths of neurites, which for $v = 0.05$ μm/s were in the 52nd, 90th and 95th percentiles of the data respectively; this is consistent with the idea that mass addition is less extreme if the diffusion path for material along the neurite is longer.

In Fig. 8.5, we show the different contributions to neurite deformation, λ, from the elastic stretch λ^e and the growth stretch λ^g. We see that for all the pull speeds, initially there is no growth and the entire deformation is elastic, $\lambda(0) = \lambda^e$. With time, the neurite grows according to Eq. 8.11 and we see $\lambda^g \rightarrow \lambda$ and $\lambda^e \rightarrow 1$. This reflects the the fact that the elastic stretch is evolving to recover a homeostatic equilibrium value. Interestingly, after ~175 s, the elastic stretches for all speeds collapse to the same values approaching 1. This indicates that for the range of speeds studied, there is a point past which the elastic response is independent of pull speed. This timescale is associated with the mechanisms of mass addition: As the cell has more time to add mass to the neurite, the stretch response of the existing neurite-components becomes less significant. For each speed, there is a time at which $\lambda^e = \lambda^g$. This time is inversely proportional to the pull speed meaning neurites are very flexible in their responses to deformation and able to

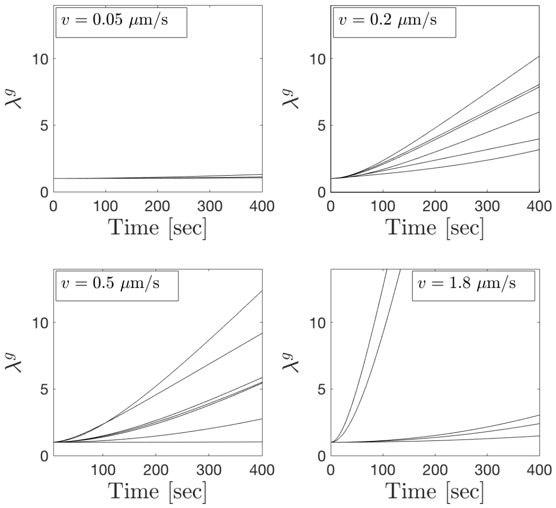

Figure 8.4 Volume growth versus time for different pull speeds. In each plot, the differing curves correspond to differing initial neurite length.

accommodate loading forces applied over a large range of speeds.

We see from the form of Eq. 8.12 that λ^g tracks λ with a pull-speed-dependant exponential term. We pull at extremely fast speeds relative to physiological ones and relative to other pulling experiments in the literature. Assuming our growth model, Eq. 8.12, is realistic, these results show new limits of mass addition for axon-like extensions.

8.4 Results from experiments

Before we conclude, we address and experimentally verify the validity of the assumptions made in this analysis.

Model selection

We have used the Mooney-Rivlin model to characterize the neurite response to deformation. However there do exist alternative choices.

To model the mechanical response of neurites to stretch, we compare a series

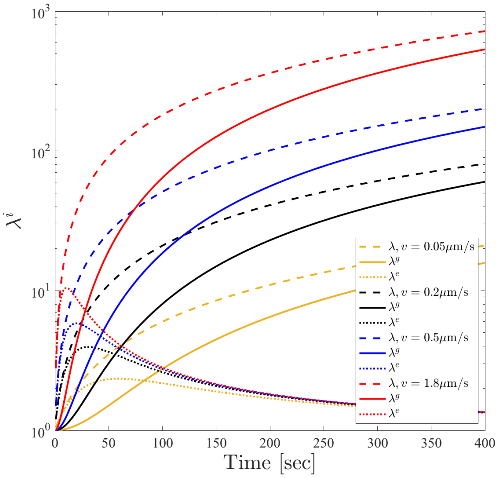

Figure 8.5 Stretch contributions of neurites. The different colours correspond to different pull speeds and the different line types (dashed, solid, dotted) are associated with different types of stretch (λ is dashed, λ^g is solid and λ^e is dotted). λ for each pull speed (dashed lines) is calculated with an initial neurite length of $L = 1$ μm. The volume addition λ^g (solid lines) for each pull speed are computed with Eq. 8.12 taking the mean $k = 0.009$ s^{-1} from all pulling experiments. We see that these track λ, approaching it for later times. $\lambda^e = \lambda/\lambda^g$ are plotted with dotted lines and show the elastic response of the neurite for different pull speeds. Initially all λ^e track λ then all collapse to values approaching 1.

of widely-used constitutive models, including viscoelatic and hyperelastic relations [11, 13, 21, 26]. We obtain constitutive relationships from strain-energy density functions, Ψ, and fit these to each curve. We determine the best fit by minimizing the Akaike Information Criterion (AIC) [27, 28]. Fig. 8.6 is a bar graph showing the frequency of 'wins' of each constitutive relationship, that is the number of curves for which that relationship gave the minimal AIC. This demonstrates that a Mooney-Rivlin relation best describes the data.

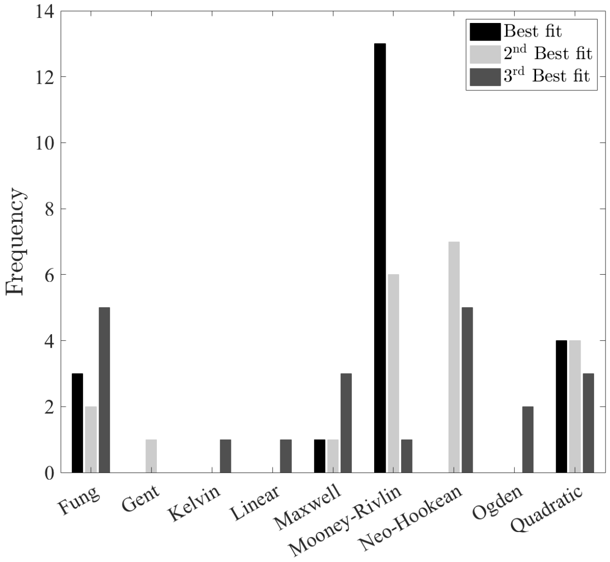

Figure 8.6 Relationships that best fit the data as determined by minimizing the AIC. Of the models commonly used to characterize the stress-strain relationship, the Mooney-Rivlin model was most frequently the best fit.

Added volume

The derivation of Eq. 8.6 assumes A is homogeneous along the axial length of the neurite [11]. In [19], a method for extracting radii of neurites below the optical-diffraction limit is developed and it is shown that neurites have a constant radius along their length a short time after they are pulled.

Together, radius measurements and our analysis confirm volume growth along the neurite. If volume were conserved during neurite deformations, then $\lambda^{\perp} = 1/\lambda^{1/2}$ [29]. In our framework, $\lambda \neq \lambda^{e}$ at later times so volume is not conserved.

From the form of λ^{e} (Fig. 8.5), we see that initially $\lambda^{\perp}$ decreases to accommodate stretch since mass flow is limited on very short timescales. With time, $\lambda^{\perp}$ increases, tending towards 1. Ref. [17] reported radial thinning then thickening along the axon but on much longer timescales (several hours). We apply stress at much faster rates than [17] and our neurites are on average $\sim 5\times$ smaller than axons. These factors could potentially explain the faster mass accretion rates observed here. Faster rates of applied stress could trigger a faster response and thinner neurites can increase their relative mass more quickly.

Critical stretch

Here we present experimental evidence of a critical stretch, λ^{*}, associated with a critical stress, σ^{*} that the neurite is trying to recover. Although we do not have sufficient statistics to concretely state $\lambda^{*} = 1$, we have indication that this is a reasonable choice, see Fig. 8.7.

In our experiments, neurites are initiated by initially pulling the bead very slowly for $1 - 5$ μm, see first snapshot of Fig. 8.7c [30]. In some cases, the neurite was pulled even further ($\sim 10 - 20$ μm, see Fig. 8.7a-b) to ensure that we could pull at greater rates without the bead becoming dislodged by other cells or debris on the coverslip. This slow initiation length was taken to be the initial length L in the analysis described above. This is the starting point for rapid pulling.

In some instances, during pulls at high pull speeds ($0.05-1.8$ μm/s), the neurite was stronger than the suction applied to fix the bead to the tip of the micropipette. In these cases, the bead would return to its initial position—indicating that the neurite has a critical tension it is trying to restore.

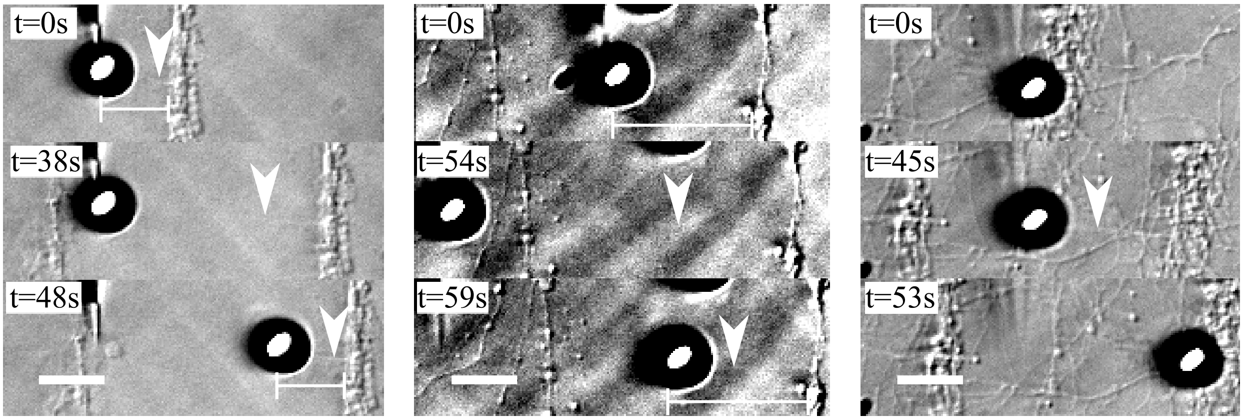

(a) (b) (c)

Figure 8.7 **(a-c)** Snapshots of experiments where the beads detach from the pipettes and the neurites (white arrows) return to their initial lengths. Thick scale bars are 10 μm. Thin scale bars represent different initial lengths; these are absent in **(c)** where the neurite is obscured by the bead. The second image in each series is the frame before the bead detaches.

8.5 Conclusion

In this work we have developed a model that links tension in extending neurites to the rate of mass addition. This lets us quantify the role of tension as a driver of neurite growth. The fact that the mechanical behaviour of induced neurites is similar to naturally-grown axons under stretch indicates that our pulling experiments are relevant to questions of axon growth [11, 13, 21, 26] . We quantify a new capacity for growth through the addition of new material.

Using a Mooney-Rivling model, we identify the contribution of hyper-elastic stretching to neurite deformation under loading. We find the material constants c_1 and c_2 vary over orders of magnitude without a satisfying reason as to why. However, we add a Mooney-Rivlin characterization of new structures to the existing body of literature. In future, this could be used in multi-cell models of the brain.

Motivated by previously-reported observations [18], we adopt an exponential growth law to model mass addition. We find that the time constants k are distributed lognormally. The mean value of k is close to the time constant of diffusion of actin in neurites, which could indicate the importance of diffusion in the growth process.

Acknowledgements

Both authors would like to acknowledge funding from the National Sciences and Research Council of Canada (NSERC) and the Fonds de recherche du Québec—Nature et technologies (FRQNT). We fervently thank Evan McDonough for invaluable discussions and recommendations for analysis.

Bibliography

[1] K. Franze, P. A. Janmey, and J. Guck. Mechanics in neuronal development and repair. *Annual review of biomedical engineering*, 13(2):e1005407, 2017.

[2] D. M. Suter and K. E. Miller. The emerging role of forces in axonal elongation. *Progress in neurobiology*, 94:91–101, 2011.

[3] A. I. M. Athamneh and D. M. Suter. Quantifying mechanical force in axonal growth and guidance. *Frontiers in cellular neuroscience*, 9:359, 2015.

[4] Steven R Heidemann and Dennis Bray. Tension-driven axon assembly: a possible mechanism. *Frontiers in cellular neuroscience*, 9:316, 2015.

[5] Matthew O'Toole, Phillip Lamoureux, and Kyle E Miller. A physical model of axonal elongation: force, viscosity, and adhesions govern the mode of outgrowth. *Biophysical journal*, 94(7):2610–2620, 2008.

[6] Jing Zheng, Phillip Lamoureux, Vivian Santiago, Timothy Dennerll, Robert E Buxbaum, and Steven R Heidemann. Tensile regulation of axonal elongation and initiation. *Journal of Neuroscience*, 11(4):1117–1125, 1991.

[7] F. Suarez, P. Thostrup, D. Colman, and P. Grutter. Dynamics of presynaptic protein recruitment induced by local presentation of artificial adhesive contacts. *Developmental neurobiology* **73**, 98–106 (2013).

[8] M. H. Magdesian, G. M. Lopez-Ayon, M. Mori, D. Boudreau, A. Goulet-Hanssens, R. Sanz, Y. Miyahara, C. J. Barrett, A. E. Fournier, Y. De Koninck

et al.. Rapid mechanically controlled rewiring of neuronal circuits. *Journal of Neuroscience* **36**, 979–987 (2016).

[9] M. Anthonisen, M. Rigby, M. H. Sangji, X. Y. Chua, and P. Grütter, Response of mechanically-created neurites to extension. *Journal of the mechanical behavior of biomedical materials* (2019).

[10] M. A. Holland, K. E. Miller, and E. Kuhl. Emerging brain morphologies from axonal elongation. *Annals of biomedical engineering* **43**, 1640–1653 (2015).

[11] A. Goriely, S. Budday, and E. Kuhl. Neuromechanics: from neurons to brain. in *Advances in Applied Mechanics,* vol. 48 (Elsevier, 2015), pp. 79–139.

[12] A. Goriely and D. Moulton,. Morphoelasticity: a theory of elastic growth. *New Trends in the Physics and Mechanics of Biological Systems: Lecture Notes of the Les Houches Summer School: Volume 92, July 2009* **92**, 153 (2011).

[13] A. Goriely, *The mathematics and mechanics of biological growth*, vol. 45 (Springer, 2017).

[14] R. Bernal, P. A. Pullarkat, and F. Melo. Mechanical properties of axons. *Physical review letters* **99**, 018301 (2007).

[15] T. J. Dennerll, P. Lamoureux, R. E. Buxbaum, and S. R. Heidemann. The cytomechanics of axonal elongation and retraction. *The journal of cell biology* **109**, 3073–3083 (1989).

[16] A. F. Bower, *Applied mechanics of solids* (CRC press, 2009).

[17] P. Lamoureux, S. R. Heidemann, N. R. Martzke, and K. E. Miller. Growth and elongation within and along the axon. *Developmental neurobiology* **70**, 135–149 (2010).

[18] M. Rigby, M. Anthonisen, X. Chua, A. Kaplan, A. Fournier, and P. Grütter. Building an artificial neural network with neurons, *AIP Advances* **9**, 075009 (2019).

[19] M. Anthonisen, Y. Zhang, M. H. Sangji, and P. Grütter. *Quantifying neurite morphology below the diffraction liimit of an optical microscope using out-of-focus images,* Submitted (2019).

[20] E. Hannezo, B. Dong, P. Recho, J.-F. Joanny, and S. Hayashi. Cortical instability drives periodic supracellular actin pattern formation in epithelial tubes. *Proceedings of the National Academy of Sciences* **112**, 8620–8625 (2015).

[21] R. de Rooij and E. Kuhl. Constitutive modeling of brain tissue: current perspectives. *Applied Mechanics Reviews* **68**, 010801 (2016).

[22] L. E. Bilston, Z. Liu, and N. Phan-Thien. Large strain behaviour of brain tissue in shear: some experimental data and differential constitutive model. *Biorheology* **38**, 335–345 (2001).

[23] M. Hrapko, J. Van Dommelen, G. Peters, and J. Wismans. The mechanical behaviour of brain tissue: large strain response and constitutive modelling. *Biorheology* **43**, 623–636 (2006).

[24] B. Rashid, M. Destrade, and M. D. Gilchrist. Mechanical characterization of brain tissue in simple shear at dynamic strain rates. *Journal of the mechanical behavior of biomedical materials* **28**, 71–85 (2013).

[25] L. A. Mihai, L. Chin, P. A. Janmey, and A. Goriely. A hyperelastic constitutive model for compression stiffening applicable to brain and fat tissues. *J. Royal Soc. Interface* **12**, 20150486 (2015).

[26] R. P. Mondaini and P. M. Pardalos, *Mathematical modelling of biosystems*, vol. 102 (Springer Science & Business Media, 2008).

[27] E.-J. Wagenmakers and S. Farrell. Aic model selection using akaike weights. bulletin & review **11**, 192–196 (2004).

[28] M. Snipes and D. C. Taylor. Model selection and akaike information criteria: An example from wine ratings and prices. *Wine Economics and Policy* **3**, 3–9 (2014).

[29] A. Fan, A. Tofangchi, M. Kandel, G. Popescu, and T. Saif. Coupled circumferential and axial tension driven by actin and myosin influences in vivo axon diameter. *Scientific reports* **7**, 14188 (2017).

[30] M. H. Magdesian, M. Anthonisen, G. M. Lopez-Ayon, X. Y. Chua, M. Rigby, and P. Grütter. Rewiring neuronal circuits: A new method for fast neurite extension and functional neuronal connection. *JoVE (Journal of Visualized Experiments)* p. e55697 (2017).

Afterword

Afterword

> One need not be a chamber to be
> haunted,
> One need not be a house;
> The brain has corridors surpassing
> Material place.
>
> Emily Dickinson

This thesis explores topics at the interface of biology and physics. We describe techniques to characterize the stress of neuron filaments and develop a model to describe their growth in response to stress. We used the tools invented here to quantify the link between tension and the mass-addition mechanisms of neurites.

There are many other applications of the force probe described in Ch. 6. It could be used to more systematically explore the differences between neurites generated from axons versus dendrites as well as the influence of the neurite-initiation site along the parent axon or dendrite. These could have important implications for understanding information processing mechanisms in the brain. Furthermore, the methods described in both Chs. 6&7 could be combined with fluorescence imaging. This could isolate the role of each cytoskeleton element in force generation and neurite initiation. It could also further elucidate the connection between mass addition and actin diffusion, noticed in Ch. 8. An important next step in this research is to conclusively prove a connection between the two processes. This would be significant in understanding the physical mechanisms underlying growth.

There are many other directions for future research. Foremost is coupling theory and measurements presented here with electrophysiological functions. The tools developed here can be readily integrated with various methods to probe the electrical properties of mechanically-created neurites (e.g. patch clamp or microelectrode arrays). This could be used to build injury models as well as answer fundamental questions about information propagation in the brain.

Finally, we thank the reader for their patience in reaching to the end of this thesis.